Pontifícia Universidade Católica
do Rio de Janeiro

Oscar Schmitt Kremer

Feedback Control of Optically Levitated Nanoparticles

Dissertação de Mestrado

Dissertation presented to the Programa de Pós–Graduação em Engenharia Elétrica da PUC-Rio in partial fulfillment of the requirements for the degree of Mestre em Engenharia Elétrica.

Advisor : Prof. Guilherme Penello Temporão
Co-advisor: Prof. Thiago Barbosa dos Santos Guerreiro

Rio de Janeiro
March 2024

Pontifícia Universidade Católica
do Rio de Janeiro

Oscar Schmitt Kremer

Feedback Control of Optically Levitated Nanoparticles

Dissertation presented to the Programa de Pós–Graduação em Engenharia Elétrica da PUC-Rio in partial fulfillment of the requirements for the degree of Mestre em Engenharia Elétrica. Approved by the Examination Committee.

Prof. Guilherme Penello Temporão
Advisor
Departamento de Engenharia Elétrica PUC-Rio

Prof. Thiago Barbosa dos Santos Guerreiro
Co-advisor
Departamento de Física PUC-Rio

Prof. Lukas Novotny
ETH Zürich

Prof. Jean Pierre von der Weid
Departamento de Engenharia Elétrica PUC-Rio

Rio de Janeiro, March 18th, 2024

Oscar Schmitt Kremer

The author graduated in Electrical Engineering from IF-Sul in 2021.

Bibliographic data

Schmitt Kremer, Oscar

Feedback Control of Optically Levitated Nanoparticles / Oscar Schmitt Kremer; advisor: Guilherme Penello Temporão; co-advisor: Thiago Barbosa dos Santos Guerreiro. – Rio de Janeiro: PUC-Rio, Departamento de Engenharia Elétrica, 2024.

v., 111 f: il. color. ; 30 cm

Dissertação (mestrado) - Pontifícia Universidade Católica do Rio de Janeiro, Departamento de Engenharia Elétrica.

Inclui bibliografia

1. Engenharia Elétrica – Teses. 2. Engenharia Elétrica – Teses. 3. levitodinâmica;. 4. teoria de controle;. 5. resfriamento.. I. Penello Temporão, Guilherme. II. Barbosa dos Santos Guerreiro, Thiago. III. Pontifícia Universidade Católica do Rio de Janeiro. Departamento de Engenharia Elétrica. IV. Título.

CDD: 530

To my father (*in memoriam*), my mother and my brother.

Acknowledgments

This work was only possible due to the help and support of others.

First, I would like to express my gratitude to my advisor Guilherme Temporão for granting me complete liberty to pursue and explore different research topics, if not for that, these last 2 years would've been completely different. To my co-advisor, Thiago Guerreiro, for the support and guidance through all the experiments, for welcoming me and allowing that I, a completely random guy from the south of Brazil, could start working with optomechanics and optical tweezers. Thanks to both, I am more than certain about what path I want to follow.

To Professor Lukas Novotny, I extend my thanks for sharing the FPGA projects that allowed us to test, examine, and further enhance our understanding of parametric cooling. Additionally, for his provision of exemplars of the Lightpath aspherical lens, which will be crucial for future cooling experiments.

I must also express my gratitude to Professor Jean Pierre von der Weid. In the same week I started the final cooling measurements, our 1550 nm laser broke. If it weren't for him lending us his laser, there would be no measurements, no cooling and no Chapter 5.

I would like to thank all my friends from the laboratory, for their help and teachings. Balancing my master's degree with a full-time job presented its challenges and moments of stress, in the end, I think surpassing all this would not have been possible without the environment you built. The lab is a truly amazing place to be, and this is mostly due to the people who are in it.

To my closest friends, I thank you for all the support during the last years. To my colleagues and friends from work, for your patience and comprehension.

I would like to thank my family. My brother, for being such a reference of researcher and professional, and for being truly by my side when I needed, even in the most difficult moments. My mother, for raising me into the man that I am today. My father passed away in 2009, and since then, she single-handed raised me and my brother, and I am here only due to all the sacrifices that she, without thinking twice, did.

Lastly, this work was only possible because of my father. Nearly 15 years after his passing, I still find myself thinking about the things he taught me. He was an example of man, father, friend, professor and professional, if I am who I am today, it is because of him, for showing me the value of education, hard work and passion. Time passes and my gratitude and admiration towards him only grows, as does my love and, of course, the *saudade*.

This study was financed in part by the Coordenação de Aperfeiçoamento de Pessoal de Nível Superior - Brasil (CAPES) - Finance Code 001.

Abstract

Schmitt Kremer, Oscar; Penello Temporão, Guilherme (Advisor); Barbosa dos Santos Guerreiro, Thiago (Co-Advisor). **Feedback Control of Optically Levitated Nanoparticles**. Rio de Janeiro, 2024. 111p. Dissertação de Mestrado – Departamento de Engenharia Elétrica, Pontifícia Universidade Católica do Rio de Janeiro.

The harnessing of optical, electric and magnetic forces to levitate and control nano-objects in high vacuum environment has enable the development of the field of levitodynamics. Optical levitation, in particular, has allowed the implementation of massive high-quality factor resonators, yielding results that include ground-state cooling at the mesoscopic scale and high precision force and displacement sensor. These advancements hold significant potential for both fundamental research and technological progress. Precise control of levitated systems is indispensable for advancing experimental techniques in levitodynamics. This level of control facilitates motion stabilization, thereby enhancing the sensitivity of these systems and enabling the attainment of the desired properties necessary for examining fundamental principles. This dissertation focuses on the study and control of certain optically levitated systems: dielectric nanospheres trapped in vacuum by a highly focused Gaussian beam. To undertake this examination, we will elucidate the theoretical framework underlying these levitated systems and highlight some majorly important control techniques. Subsequently, we will proceed to experimental investigations where we aim to apply feedback forces in two different contexts. First, we will explore feedback forces as a way to change the dynamics of levitated nanoparticles, by means of adding nonlinear terms governing their motion. Secondly, we will detail the development of an experimental setup that allows 3D stabilization of motion by applying an all electrical control scheme, allowing stable trapping at high vacuum.

Keywords

levitodynamics; control theory; feedback cooling.

Resumo

Schmitt Kremer, Oscar; Penello Temporão, Guilherme; Barbosa dos Santos Guerreiro, Thiago. **Teoria de controle aplicada à partículas levitadadas opticamente**. Rio de Janeiro, 2024. 111p. Dissertação de Mestrado – Departamento de Engenharia Elétrica, Pontifícia Universidade Católica do Rio de Janeiro.

A utilização de forças ópticas, elétricas e magnéticas para levitar e controlar nano-objetos em um ambiente de alto vácuo possibilitou o desenvolvimento do campo da levitodinâmica. A levitação óptica, em particular, permitiu a implementação de ressonadores massivos de alto fator de qualidade, conduzindo a resultados que incluem o resfriamento ao estado fundamental em escala mesoscópica e o desenvolvimento de sensores com sensibilidade ultrafina. Esses avanços possuem um potencial significativo tanto no âmbito da pesquisa fundamental quanto em termos de progresso tecnológico. O desenvolvimento e implementação de técnicas avançadas de controle é indispensável para o avanço experimental na levitodinâmica, visto que facilita a estabilização do movimento destes sistemas levitados, melhorando assim a sua sensibilidade e possibilitando a obtenção das propriedades necessárias para examinar princípios fundamentais. Esta dissertação concentra-se no estudo e controle de certos sistemas levitados opticamente: nanoesferas dielétricas aprisionadas no vácuo por um feixe Gaussiano altamente focalizado. Para realizar essa investigação, elucidaremos a descrição teórica destes sistemas e destacaremos algumas técnicas de controle importantes. Posteriormente, procederemos a investigações experimentais onde visamos atuar em dois contextos diferentes. Primeiramente, exploraremos a geração de forças não lineares como uma maneira de alterar o movimento dessas nanopartículas, visando compreender o efeito destes termos na sua dinâmica. Em segundo lugar, detalharemos o desenvolvimento de um aparato experimental que permite a estabilização tridimensional do movimento de uma nanopartícula por meio da aplicação apenas de controle elétrico, permitindo aprisionamento estável em alto vácuo.

Palavras-chave

levitodinâmica; teoria de controle; resfriamento.

Table of contents

List of figures

List of tables

List of Abreviations

ADC – Analog-to-Digital Converter

BS – Beam Splitter

CoM – Center of Mass

CW – Continuous Wave

DOF – Degree of Freedom

EDFA – Erbium-Doped Fiber Amplifier

FPGA – Field-Programmable Gate Array

IIR – Infinite Impulse Response

LFSR – Linear-Feedback Shift Register

LQE – Linear Quadratic Estimator

LQG – Linear Quadratic Gaussian

LQR – Linear Quadratic Regulator

MRAC – Model-Reference Adaptive Controller

MIMO – Multiple-Input Multiple-Output

NA – Numerical Aperture

PBS – Polarised Beam Splitter

PCB – Printed Circuit Board

PLL – Phase Lock-in Loop

PSD – Power Spectral Density

SISO – Single-Input Single-Output

SNR – Signal-to-Noise Ratio

Out of the night that covers me
Black as the pit from pole to pole,
I thank whatever gods may be
For my unconquerable soul.

William Ernest Henley, *Invictus.*

1
Introduction

The study of the interaction between light and matter has captivated researchers for well over a century, dating back to Einstein's contributions on photon momentum transfer [1] and the first experimental observation of radiation pressure in 1901 [2, 3]. These inquiries have given rise to *optomechanics*, the specialized field of physics dedicated to explore the interactions between electromagnetic radiation and mechanical systems [4, 5]. Over time, optomechanics has become instrumental in exploring the manipulation and even control of mechanical motion by use of optical forces, with experimental results spanning in various areas and scales. Examples include GHz rotation of nanoparticles and nanodumbbells [6, 7], trapping and manipulation of microorganisms [8, 9], macroscopic mirrors used for the detection of gravitational waves [10] and the ground-state cooling of clamped and optically levitated nanomechanical resonators [11–15].

Optical manipulation of nano and micron-sized particles was first proposed and implemented by Arthur Ashkin [16], and it has enabled a sequence of works, including stable trapping of cells [17], dielectric particles [18, 19] and atoms [20], culminating in the tool that nowadays is known as *optical tweezer*. Optical tweezers have consistently proven to be a versatile experimental tool for biophysics [8, 9], sensing [21–24], non-equilibrium physics [25] and quantum science [13–15, 26, 27]. Levitated optomechanics, also referred as *levitodynamics*, focuses on harnessing trapping forces to control nano-objects in vacuum environments. When implemented with optical tweezers, this yields massive high quality-factor resonators with almost complete thermal isolation from external perturbations. These optomechanical systems are a promising platform for analysing and exploring quantum phenomena at the mesoscopic scale [28].

One of the primary objectives in levitated optomechanics is the development of techniques for accurate measurement and control of nano-objects. Specifically, the controlled reduction in the amplitude of oscillation of the trapped particle's motion, known as *cooling*, is essential for experimental purposes due to two main reasons. Firstly, the removal of residual gas in the vacuum chamber decreases the damping of the medium, thereby increasing the

chance of motional instability, which is further compounded by the effects of nonlinearities and coupling between distinct axes [29]. Secondly, observation of quantum aspects or preparation of a pure quantum state hinges directly upon decoupling the particle's dynamics from external noise sources. Additionally, control mechanisms also enable the exploration of tweezed nanoparticles as a platform for fundamental physics by introducing additional forces terms to artificially alter the particle's dynamics, allowing the examination of the system response to nonlinear [30] or stochastic driving forces [31, 32].

Optomechanical cooling can be pursued through two strategies, *passive* and *active* cooling. Passive cooling relies on feedback terms provided by scattering processes within optical cavities to cool the motion of trapped objects [13, 33], while active cooling depends on real-time measurements of the particle's displacement, enabling employment of a variety of control theory algorithms to compute feedback forces that are then applied by optical [34, 35] or electrical actuators [14, 15, 36, 37], aiming at effectively damping the nano-object's dynamics. Control theory is one of the main sub-areas in electrical engineering, with part of its findings intersecting with signal processing, artificial intelligence, stochastic analysis and optimization. Its application on quantum systems has given rise to the field known as *quantum control* [38].

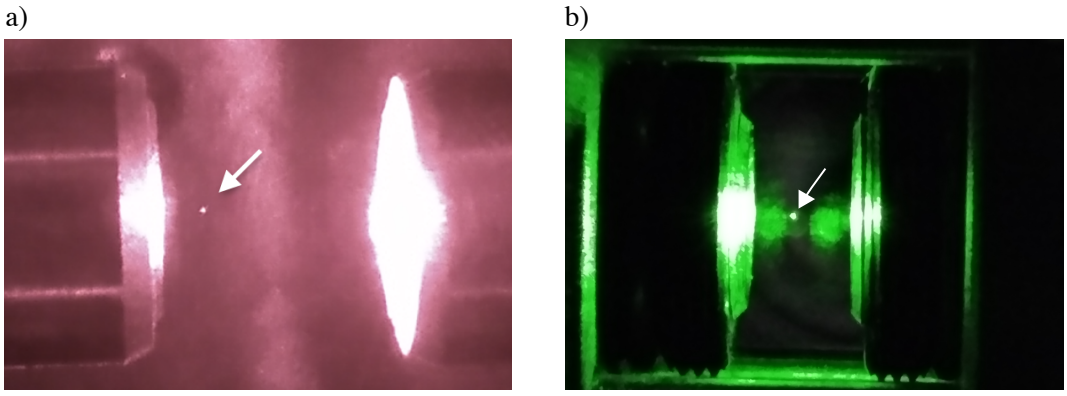

Figure 1.1: Optically levitated nanoparticles in the 780 nm a) and 1550 nm optical tweezer b). White arrows indicate the trapped nano-object, which for both tweezers consists in a 71.5 nm radius Silica nanosphere (MicroParticles GmbH). In both cases the optical trap was assembled inside a vacuum chamber.

This dissertation primarily focuses on implementing and exploring control methods within the domain of optically levitated nanoparticles. After assembling two optical tweezers — one operating with a 780 nm laser and the other at 1550 nm — each setup will be utilized to present experimental results regarding the use of feedback terms generated by electrodes positioned near each tweezer. Images of nanoparticles trapped in these experimental setups are shown in

Fig. 1.1. This dissertation is organized into six chapters, with its main content (Chapters 2, 3, 4 and 5) divided into two parts.

The first part, comprised of Chapters 2 and 3, presents the theoretical foundation and key concepts of optical tweezers and control theory. Given the complexity inherent in describing generic optical beams applied to optical tweezers across all regimes, Chapter 2 focuses on formulating the dynamics of tweezed nanoparticles considering specific parameters and characteristics used in the experiments presented in the subsequent chapters. Chapter 3 introduces general concepts of control theory, leading to the presentation of control methods relevant to the optomechanics community. Readers already familiar with either of these topics may opt to skip these chapters.

The second part, Chapters 4 and 5, presents the experimental setups and results. Chapter 4 aims to validate theoretical predictions previously made regarding perturbative nonlinear forces on underdamped stochastic systems, where feedback is explored to induce an additional weak cubic nonlinearity. Chapter 5 presents results of 3D cooling, which relied on the application of an optimal control method and an all electrical actuation scheme, resulting in the stable motion of a silica nanoparticles at pressures in the order of 10^{-5} mbar. For the best extend of our knowledge, both setups are the first (780 nm) and second (1550 nm) optical tweezers in vacuum in South America. As is briefly mentioned in the beginning of each of these chapters, their content is presented just like articles produced from the results showcased. Some overlap and redefinitions are noticeable as some concepts need to be introduced within each article's scope. Conclusions of each experiment are made at end of each respective chapter.

Chapter 6 is dedicated to presenting potential future research directions and general closing remarks. The list of publications produced throughout this Masters is shown in Appendix A. Auxiliary methods necessary for the development of the content in Chapter 3 are presented in Appendix B. Additional characterizations and results related to the setup from Chapter 5 have been added to Appendix C. The code implemented to produce all the plots and simulations in this dissertation can be found in [39, 40], with a brief description of code's organization and structure in the final appendix. The code repositories also include details and documentation regarding digital electronic implementations.

2
Optical tweezers in the dipole regime

Prior knowledge with respect to the system's dynamics is fundamental to efficiently control any physical system, allowing one to anticipate possible non-linearities and stochasticities, and to optimize the controller's performance and robustness. Throughout this chapter we dedicate our efforts into understanding the dynamics of a dielectric nanoparticle levitated due to the optical forces exerted by a focused Gaussian beam. Starting from the Maxwell's equations, we present the description of the fundamental mode of a laser beam focused by an aplanatic lens. We then proceed with the dipole approximation, a simplification applied to particles sufficiently smaller than the laser's wavelength. Lastly, we conclude by examining the particle's equation of motion and possible anharmonicities.

2.1
Optical beams

To mathematically describe the motion of a tweezed nanoparticle, we must first understand the mathematical description of the electromagnetic field in the vicinity of the particle's position. In this section, we briefly present the theoretical foundations that enable the derivation of the electromagnetic field of a strongly focused Gaussian beam, covering topics such as the description of monochromatic planes waves, the paraxial approximation and the angular spectral representation. The mathematical description presented is based primarily on [41, 42].

2.1.1
Plane Waves

A monochromatic electromagnetic field with angular frequency ω propagating in a linear, homogeneous, non-dispersive, isotropic and source free-medium satisfy the Maxwell's equations,

$$\nabla \times \mathbf{E}(\mathbf{r}, t) = -i\omega\mu\mathbf{H}(\mathbf{r}, t), \tag{2-1a}$$

$$\nabla \times \mathbf{H}(\mathbf{r}, t) = i\omega\varepsilon\mathbf{E}(\mathbf{r}, t), \tag{2-1b}$$

$$\nabla \cdot \mathbf{E}(\mathbf{r}, t) = 0, \tag{2-1c}$$

$$\nabla \cdot \mathbf{H}(\mathbf{r}, t) = 0, \tag{2-1d}$$

where $\mathbf{E}(\mathbf{r}, t)$ is the electric field, $\mathbf{H}(\mathbf{r}, t)$ the magnetic field, and ε and μ are the dielectric permittivity and magnetic permeability of the medium, respectively. Utilizing properties of vector calculus, these equations can be rewritten as

$$\nabla^2\mathbf{E}(\mathbf{r}, t) + \omega^2\mu\varepsilon\mathbf{E}(\mathbf{r}, t) = \mathbf{0}, \tag{2-2a}$$
$$\nabla^2\mathbf{H}(\mathbf{r}, t) + \omega^2\mu\varepsilon\mathbf{H}(\mathbf{r}, t) = \mathbf{0}, \tag{2-2b}$$

which are the vector Helmholtz equations for electric and magnetic fields propagating at velocity $v = 1/\sqrt{\mu\varepsilon}$. The simplest solution for Eqs. (2-2) is the transverse electromagnetic plane wave,

$$\mathbf{E}(\mathbf{r}, t) = E_0 e^{-i(\mathbf{k}\cdot\mathbf{r}-\omega t)}\,\hat{\mathbf{u}}_e, \tag{2-3a}$$
$$\mathbf{H}(\mathbf{r}, t) = H_0 e^{-i(\mathbf{k}\cdot\mathbf{r}-\omega t)}\,\hat{\mathbf{k}} \times \hat{\mathbf{u}}_e. \tag{2-3b}$$

Here, E_0 and H_0 are, respectively, the complex amplitudes for the electric and magnetic field, $\hat{\mathbf{k}}$ is the unitary vector of $\mathbf{k}$, which is the wavevector, and $\hat{\mathbf{u}}_e$ is the polarisation vector, which obeys $\mathbf{k}\cdot\hat{\mathbf{u}}_e = 0$. The wavevector magnitude is $|\mathbf{k}| = k = \omega\sqrt{\mu\varepsilon}$. By using the phasor representation, $\mathbf{E}(\mathbf{r}, t) = \mathbf{E}(\mathbf{r})e^{i\omega t}$, we will omit the time parameter t from $\mathbf{E}(\mathbf{r}, t)$ when referring specifically to the spatially dependent component $\mathbf{E}(\mathbf{r})$.

Considering the wavevector in the Cartesian space, $\mathbf{k} = [k_x, k_y, k_z]$, one of its components, without loss of generality chosen here to be k_z, can be represented as

$$k_z = k\sqrt{1 - \frac{k_x^2 - k_y^2}{k^2}}. \tag{2-4}$$

Since k is solely determined by properties of the medium, this relation when applied to Eqs. (2-3) gives rise to two distinct scenarios. Firstly, when $k^2 < k_x^2 + k_y^2$, we encounter evanescent waves. These waves exhibit an exponentially decaying behavior, making them non-propagating and outside the scope of our interest. Secondly, for $k^2 \geq k_x^2 + k_y^2$, we have the plane waves, characterized by an oscillating behavior along the z-axis.

Even thought a true plane wave cannot exist they are useful because a generic electric field $\mathbf{E}(\mathbf{r})$ can be expressed as a superposition of plane waves by using what is called as the *angular spectrum representation* [41, 42]. By rewriting $\mathbf{E}(\mathbf{r})$ into this plane wave basis, we obtain

$$\mathbf{E}(\mathbf{r}) = \int_{-\infty}^{\infty}\int_{-\infty}^{\infty} \bar{\mathbf{E}}(k_x, k_y, 0)e^{i(k_x x + k_y y \pm k_z z)}\,dk_x\,dk_y, \tag{2-5}$$

where

$$\bar{\mathbf{E}}(k_x, k_y, 0) = \frac{1}{4\pi^2} \int_{-\infty}^{\infty} \int_{-\infty}^{\infty} \mathbf{E}(x, y, 0) e^{-i(k_x x + k_y y)}\, dx\, dy. \tag{2-6}$$

Then, considering that we have knowledge of $\mathbf{E}(x, y, 0)$, is possible to compute the different spectral components $\bar{\mathbf{E}}(k_x, k_y, 0)$ of the electric field in the plane $z = 0$. By propagating each component individually along the z-axis and applying the inverse Fourier transform, we can reconstruct $\mathbf{E}(x, y, z)$ for any value of x, y and z.

2.1.2 Paraxial approximation

In certain experiments, which include the ones described in Chapters 4 and 5 of this dissertation, the propagation of a laser beam predominantly occurs along a specific direction, herein assumed to be along the z-axis, with spreading observed in the transverse plane (x and y directions). With this condition in mind, we can expand Eq. (2-4) in a Taylor series, resulting in

$$k_z(k_x, k_y) = k_z(0, 0) + \frac{k_x^2}{2!}\frac{\partial^2 k_z}{\partial k_x^2} + \frac{k_y^2}{2!}\frac{\partial^2 k_z}{\partial k_y^2} + \frac{k_x k_y}{2!}\frac{\partial^2 k_z}{k_x k_y} + \mathcal{O}(k_x^4, k_y^4), \tag{2-7}$$

and leading to what is entitled as *paraxial approximation*,

$$k_z(k_x, k_y) \approx k - \frac{k_x^2 + k_y^2}{2k}. \tag{2-8}$$

This approximation considerably simplifies the integrals in Eqs. (2-5) and (2-6), making it extremely useful in describing weakly focused laser beams. However, it is important to note that in cases of strong focusing, this approximation is no longer valid [41, 42].

2.1.3 Gaussian beam

In light of the paraxial approximation, we may apply to Eq. (2-6) an electric field with a Gaussian distribution in the xy-plane for $z = 0$,

$$\mathbf{E}(x, y, 0) = E_0 e^{-\frac{x^2+y^2}{w_0^2}} \hat{\mathbf{u}}_e, \tag{2-9}$$

where w_0 is the waist radius, or beam waist. By solving the components of $\mathbf{E}$ in the plane wave basis we encounter

$$\bar{\mathbf{E}}(k_x, k_y, 0) = \frac{w_0^2 E_0}{4\pi} e^{-\frac{w_0^2(k_x^2+k_y^2)}{4}} \hat{\mathbf{u}}_e. \tag{2-10}$$

Then, the spectral components may be inserted into Eq. (2-5), resulting in the paraxial representation of a Gaussian beam,

$$\mathbf{E}(x, y, z) = E_0 \frac{w_0}{w(z)} e^{-\frac{x^2+y^2}{w(z)^2}} e^{i[kz - \zeta(z) + k(x^2+y^2)/2R(z)]} \hat{\mathbf{u}}_e, \tag{2-11}$$

with

$$w(z) = w_0\sqrt{1+\frac{z^2}{z_0^2}}, \tag{2-12a}$$

$$R(z) = z\left(1+\frac{z_0^2}{z^2}\right), \tag{2-12b}$$

$$\zeta(z) = \arctan\left(\frac{z}{z_0}\right), \tag{2-12c}$$

$$z_0 = \frac{n\pi w_0}{\lambda}, \tag{2-12d}$$

where $w(z)$ is the waist function, $\zeta(z)$ the Gouy phase shift, $R(z)$ the wavefront radius, n is the refractive index of the medium and z_0 the Rayleigh length. Equation (2-11) describes one of the most commonly used beams in optics. The Gaussian beam is the fundamental mode sustained by a spherical-mirror cavity, a type of resonator employed in the construction of the majority of lasers [43, 44]. Although some lasers can emit other modes, our focus throughout this dissertation will remain on the Gaussian mode, as it is the one employed in the experiments detailed in the Chapters 4 and 5.

The intensity $I(x, y, z)$ of this electromagnetic field will also follow a Gaussian distribution,

$$I(x,y,z) = \frac{c\varepsilon}{2}|\mathbf{E}(\mathbf{r})|^2 = \frac{c\varepsilon|E_0|^2}{2}\left[\frac{w_0}{w(z)}\right]^2 e^{-\frac{2(x^2+y^2)}{w(z)^2}}, \tag{2-13}$$

and from this expression we can relate the magnitude of the electric field complex amplitude $|E_0|$ with the output power P of the laser source,

$$|E_0| = \sqrt{\frac{4P}{c\varepsilon\pi w_0^2}}. \tag{2-14}$$

For a clearer understanding of its characteristics, in Fig. 2.1a) we present the longitudinal profile of the Gaussian beam and in Fig. 2.1b) the transversal profile of its intensity. As can be seen, for $|z| \ll z_0$, $w(z)$ remain approximately constant, and the beam can be treated as a plane wave propagating along the z-axis.

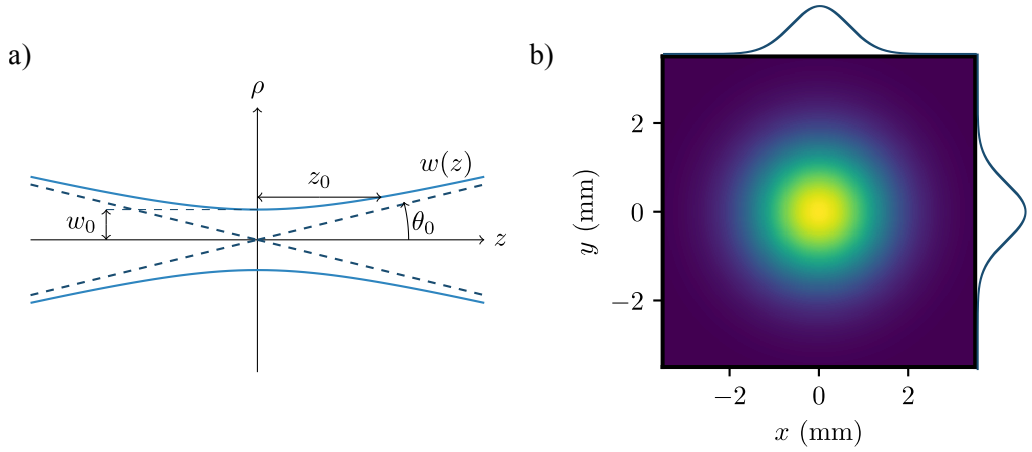

Figure 2.1: Gaussian beam. a) Longitudinal profile highlighting w_0, z_0 and the hyperboloid formed along the z-axis by the waist function $w(z)$, here $\rho = \sqrt{x^2 + y^2}$ and $\theta_0 = w_0/z_0$. b) Transversal profile of the intensity for an optical beam with $w_0 = 2.2\,\text{mm}$ and $P = 300\,\text{mW}$. Colormap is presented in arbitrary units (normalized by the maximum intensity).

2.1.4 Focusing a Gaussian beam

In optical manipulation of nano-objects, strongly focused optical fields are used [16]. A theoretical treatment of how an optical field behaves after being focused by an aplanatic lens was presented in [45, 46]. This approach may be employed to characterize the electromagnetic field at the focal point of an aspheric lens after the incidence of a Gaussian beam on its surface. To better comprehend this, let us refer to Fig. 2.2 (figure inspired by the representation found in Chapter 4, Section 5 of [42]). A paraxial optical field propagating along the z-axis crosses an aperture stop of radius R_a and then reaches the surface p_l of an aspheric lens. This surface is centered at the focal point and has a radius equals to the focal length f. For this case, we assume that the mediums before and after the lens have $\varepsilon = \varepsilon_0$ and $\mu = \mu_0$.

The electric field before the lens, $\mathbf{E}_\text{i}$, and after, $\mathbf{E}_\text{t}$, must adhere the *intensity law* of geometric optics, which states that the energy flux along each optical ray must remain constant even after passing by a perfect optical element. This conduct us to an initial conclusion regarding the relation between the magnitude of $\mathbf{E}_\text{i}$ and $\mathbf{E}_\text{t}$,

$$|\mathbf{E}_\text{i}| = \sqrt{\cos\theta}|\mathbf{E}_\text{t}|. \tag{2-15}$$

Due to the azimuthal symmetry, we represent $\mathbf{E}_\text{i}$ in cylindrical coordinates and decompose its components into radial and azimuthal polarisations, referred to as p- and s-polarisations, respectively,

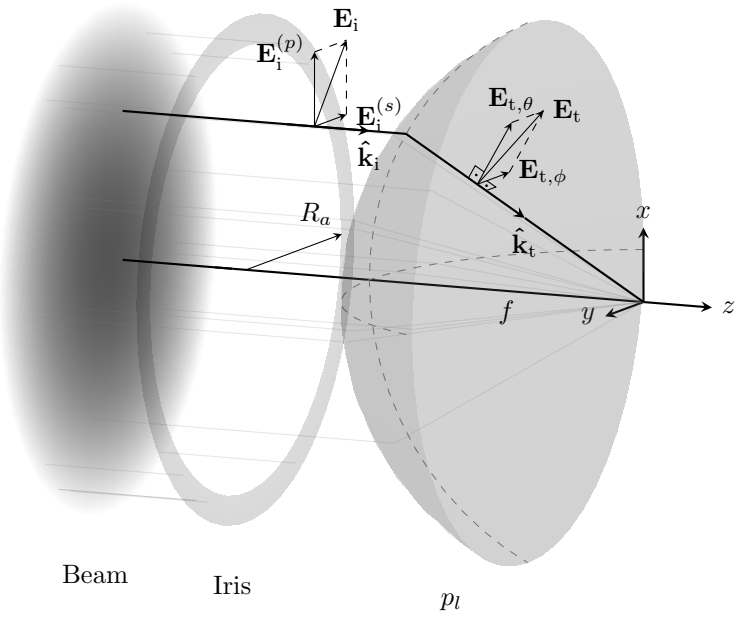

Figure 2.2: Focusing of an optical beam by an aplanatic optical lens. An optical beam, depicted as a set of rays, passes through an iris and reaches the spherical surface p_l of an optical lens. At p_l each ray is refracted and focused.

$$\mathbf{E}_\mathrm{i}(\rho,\phi) = [\mathbf{E}_\mathrm{i}(\rho,\phi)\cdot\hat{\mathbf{u}}_\rho]\hat{\mathbf{u}}_\rho + [\mathbf{E}_\mathrm{i}(\rho,\phi)\cdot\hat{\mathbf{u}}_\phi]\hat{\mathbf{u}}_\phi. \tag{2-16}$$

After passing through the lens, it is practical to represent the electric field in a spherical coordinate system, considering the lens's geometric aspects. The incident electric field will be refracted by the lens, with the component $\hat{\mathbf{u}}_\phi$ remaining unchanged, while $\hat{\mathbf{u}}_\rho$ is transformed into $\hat{\mathbf{u}}_\theta$. This transformation corresponds to the polarisations $\mathbf{E}_\mathrm{i}^{(p)}$ and $\mathbf{E}_\mathrm{i}^{(s)}$ becoming $\mathbf{E}_{\mathrm{t},\theta}$ and $\mathbf{E}_{\mathrm{t},\phi}$, respectively, and for the unitary wavevector $\hat{\mathbf{k}}_\mathrm{i}$ turning into $\hat{\mathbf{k}}_\mathrm{t}$. Considering the coordinate system transformation and Eq. (2-15), $\mathbf{E}_\mathrm{t}$ can be expressed as

$$\mathbf{E}_\mathrm{t}(\theta,\phi) = \sqrt{\cos\theta}[t_s(\theta)(\mathbf{E}_\mathrm{i}\cdot\hat{\mathbf{u}}_\phi)\hat{\mathbf{u}}_\phi + t_p(\theta)(\mathbf{E}_\mathrm{i}\cdot\hat{\mathbf{u}}_\rho)\hat{\mathbf{u}}_\theta]. \tag{2-17}$$

The functions $t_s(\theta)$ and $t_p(\theta)$ are referred to as *apodisation* or *pupil functions* and serve to take into account attenuation, distortions and aberrations that may be caused to each polarisation. Since p_l is located in the far-field region ($k_\mathrm{t} f \gg 1$) of the focal point, we can obtain the electric field at the focus $\mathbf{E}_\mathrm{f}$ by employing the near-field to far-field relation,

$$\mathbf{E}_\mathrm{f}(x,y,z) = \frac{ik_\mathrm{t} f e^{-ik_\mathrm{t} f}}{2\pi}\int_0^{\theta_\mathrm{max}}\int_0^{2\pi}\mathbf{E}_\mathrm{t}(\theta,\phi)e^{ik_{\mathrm{t,z}}z}e^{i(k_{\mathrm{t,x}}x+k_{\mathrm{t,z}}y)}\sin\theta\,d\phi\,d\theta. \tag{2-18}$$

The parameter θ_max is defined as a function of the numerical aperture (NA), $\theta_\mathrm{max} = \arcsin(\mathrm{NA})$, and not only directly affects the integration domain in Eq. (2-18) but also influences the apodisation functions t_s and t_p [41]. Applying

to this formalism a Gaussian beam linearly polarised along the $\hat{\mathbf{u}}_x$ direction we encounter the intensity profile depicted in Fig. 2.3a). In Fig. 2.3b) we examine the profile along $x = 0$ and $y = 0$, showing a small asymmetry, which will have an impact in the behavior of a tweezed nanoparticle, as shown in Sections 2.2 and 2.3.

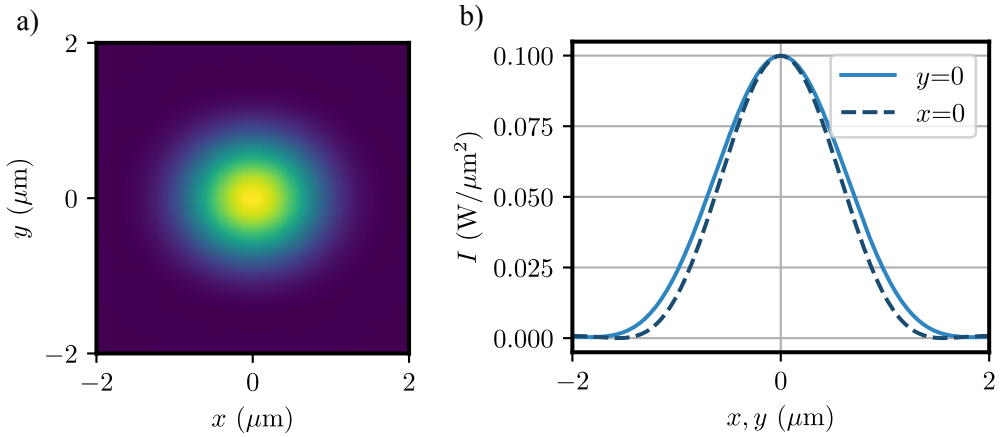

Figure 2.3: Intensity of a focused Gaussian beam. a) Transversal profile of the intensity at the focal point. Colormap is presented in arbitrary units (normalized by the maximum intensity). b) Intensity at the focal point evaluated along x-direction ($y = 0$) and y-direction ($x = 0$).

2.2 Optical forces on an electrical dipole

Now that we can describe the electromagnetic field in the focus of an aplanatic lens, let us shift our attention to the forces experienced by a nanosphere when it is positioned near the focal point. When the nanoparticle's radius R is significantly smaller than the laser's wavelength, $R \ll \lambda$, the electromagnetic field within the particle becomes approximately uniform [42,47]. However, this uniform field will induce an electric dipole in a dielectric particle, and because it undergoes time-dependent oscillations, the dipole also oscillates.

An electric dipole can be modelled as two particles of mass $m/2$ and charges $+q$ and $-q$, at positions $\mathbf{r}_+(t)$ and $\mathbf{r}_-(t)$, respectively. The particles will experience Lorentz forces due to the electric $\mathbf{E}_\mathrm{f}$ and magnetic $\mathbf{H}_\mathrm{f}$ fields at the focus. The equations describing the motion of the dipole are

$$m\frac{d^2\mathbf{r}_+(t)}{dt^2} = +q\mathrm{Re}\left[\mathbf{E}_\mathrm{f}(\mathbf{r}_+,t) + \mu_0\frac{d\mathbf{r}_+(t)}{dt}\times\mathbf{H}_\mathrm{f}(\mathbf{r}_+,t)\right], \tag{2-19a}$$

$$m\frac{d^2\mathbf{r}_-(t)}{dt^2} = -q\mathrm{Re}\left[\mathbf{E}_\mathrm{f}(\mathbf{r}_-,t) + \mu_0\frac{d\mathbf{r}_-(t)}{dt}\times\mathbf{H}_\mathrm{f}(\mathbf{r}_-,t)\right]. \tag{2-19b}$$

As the particle is much smaller than λ, we can expand $\mathbf{E}_\mathrm{f}$ and $\mathbf{H}_\mathrm{f}$ in a Taylor series around the dipole center of mass $\mathbf{r}_d = \frac{\mathbf{r}_+ + \mathbf{r}_-}{2}$. This leads to a first order approximation,

$$\mathbf{E}_\mathrm{f}(\mathbf{r}_\pm, t) \approx \mathbf{E}_\mathrm{f}(\mathbf{r}_d, t) + [(\mathbf{r}_\pm - \mathbf{r}_d)\cdot\nabla]\mathbf{E}_\mathrm{f}(\mathbf{r}_d, t), \tag{2-20a}$$

$$\mathbf{H}_\mathrm{f}(\mathbf{r}_\pm, t) \approx \mathbf{H}_\mathrm{f}(\mathbf{r}_d, t) + [(\mathbf{r}_\pm - \mathbf{r}_d)\cdot\nabla]\mathbf{H}_\mathrm{f}(\mathbf{r}_d, t). \tag{2-20b}$$

Now, after summing both expressions in Eq. (2-19) and substituting the expansion in Eqs. (2-20), we arrive at the equation of motion for the dipole's center of mass,

$$m\frac{d^2\mathbf{r}_d}{dt^2} = (\mathbf{p}\cdot\nabla)\mathbf{E}_\mathrm{f}(\mathbf{r}_d, t) + \mu_0\left[\frac{d\mathbf{p}}{dt}\times\mathbf{H}_\mathrm{f}(\mathbf{r}_d, t) + \frac{d\mathbf{r}_d}{dt}\times(\mathbf{p}\cdot\nabla)\mathbf{H}_\mathrm{f}(\mathbf{r}_d, t)\right], \tag{2-21}$$

where $\mathbf{p} = q(\mathbf{r}_+ - \mathbf{r}_-)$ is the electric dipole moment. Our main interest will be in time-averaged values of the force because the oscillations in the electromagnetic field are much faster than the mechanical motion of the nanoparticle.

This assumption allows us to find the expression for the time-averaged force applied to the nanoparticle by the focused laser beam [42, 47, 48],

$$\begin{aligned}\mathbf{F}(\mathbf{r}) = \frac{1}{4}\mathrm{Re}\{\alpha_d\}\nabla|\mathbf{E}_\mathrm{f}(\mathbf{r})|^2 + \frac{k\mathrm{Im}\{\alpha_d\}}{2c\varepsilon_0}\mathrm{Re}\{\mathbf{E}_\mathrm{f}(\mathbf{r})\times\mathbf{H}_\mathrm{f}^*(\mathbf{r})\} \\ - \frac{ick\mathrm{Im}\{\alpha_d\}}{4\omega}[\nabla\times(\mathbf{E}_\mathrm{f}(\mathbf{r})\times\mathbf{E}_\mathrm{f}^*(\mathbf{r}))],\end{aligned} \tag{2-22}$$

where α_d is the effective polarisability, which provides the linear relation $\mathbf{p} = \alpha_d\mathbf{E}_f$ and introduces corrections to the Clausius-Mossoti polarisability, α_{CM}, for cases when the nanoparticle is in the presence of an oscillating field. The expression for α_d is [42]

$$\alpha_d \approx \alpha_{CM}\left(1 - i\frac{k^3\alpha_{CM}}{6\pi\varepsilon_0}\right)^{-1}, \tag{2-23}$$

with $\alpha_{CM} = 4\pi\varepsilon_0 R^3(\varepsilon_R^2 - 1)/(\varepsilon_R^2 + 2)$ and $\varepsilon_R = \varepsilon_p/\varepsilon_m$, where ε_p is the dielectric permittivity of the particle and ε_m the dielectric permittivity of the medium.

After plugging Eq. (2-23) into Eq. (2-22) and rewriting the expression by means of the intensity $I_\mathrm{f}(\mathbf{r})$ of the focused optical field, we find the following expressions for the first and second terms on right side of Eq. (2-22),

$$\mathbf{F}_\mathrm{grad}(\mathbf{r}) = \frac{2\pi R^3}{c}\left(\frac{\varepsilon_R^2 - 1}{\varepsilon_R^2 + 2}\right)\nabla I_\mathrm{f}(\mathbf{r}), \tag{2-24}$$

$$\mathbf{F}_\mathrm{scat}(\mathbf{r}) = \frac{128\pi^5 R^6}{3c\lambda^4}\left(\frac{\varepsilon_R^2 - 1}{\varepsilon_R^2 + 2}\right)^2 I_\mathrm{f}(\mathbf{r})\hat{\mathbf{u}}_z. \tag{2-25}$$

First, in Eq. (2-24) we have a conservative force, proportional to $\nabla I_\mathrm{f}(\mathbf{r})$, and entitled as the *gradient* force, and second, in Eq. (2-25) the *scattering*

force, a non-conservative force acting along the optical axis due to scattering and absorption processes. The remaining force is entitled as the *spin-curl* force and appears in the presence of polarization gradients [42, 49]. This force will be disregarded as we will work with uniform linearly polarised laser beams. In Fig. 2.4 we present the simulated forces for a silica nanoparticle with radius $R = 71.5\,\text{nm}$ trapped in air by a 1550 nm Gaussian beam with power $P = 300\,\text{mW}$ and initial waist of $w_0 = 2.75\,\text{mm}$. The beam is focused by an aspheric lens with NA of 0.67 and focal length $f = 3.1\,\text{mm}$.

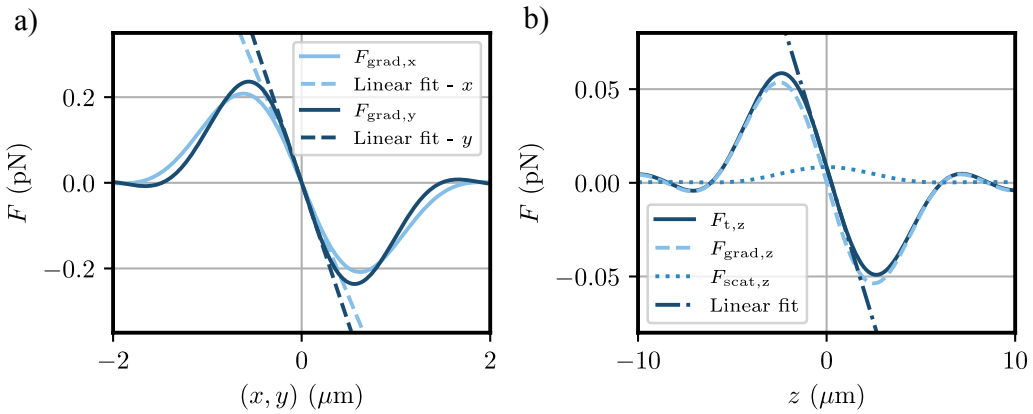

Figure 2.4: Optical forces in a Gaussian optical trap. a) Forces along the x and y-axis. b) Total, gradient and scattering forces along the z-axis.

As shown in Fig. 2.4, we can observe that for sufficiently small displacements, the forces acting along each axis can be approximated as harmonic forces, denoted as $F_i = -k_{m,i} r_i$ for $i \in \{x, y, z\}$. These spring constants, represented as $k_{m,j}$, allow us to calculate characteristic oscillation frequencies for each axis, denoted as $\Omega_i = \sqrt{k_{m,i}/m}$, for a particle with mass m. In the specific simulation shown in Fig. 2.4, these frequencies are $\Omega_x/2\pi = 63.10\,\text{kHz}$, $\Omega_y/2\pi = 70.24\,\text{kHz}$ and $\Omega_z/2\pi = 15.79\,\text{kHz}$. The difference between Ω_x and Ω_y is attributed to the asymmetry in the intensity profiles along x and y presented in Fig. 2.3.

2.3 Dynamics of a levitated nanoparticle

The motion of a nanoparticle is governed by the various forces acting upon it. In the previous section, we demonstrated that the effect of the optical field can be approximated as harmonic forces acting along each axis. However, a trapped nanosphere is subject to additional forces, including a drag force resulting from friction between the object and the surrounding fluid, as well as a stochastic force arising from random collisions between residual gas molecules and the nanosphere. The motion of the nano-object can be mathematically

described using a second-order Langevin equation,

$$\ddot{z}(t) + \gamma_m \dot{z}(t) + \Omega_z^2 z(t) = \frac{1}{m} F_{\text{th}}(t). \tag{2-26}$$

Here, γ_m represents the drag coefficient and F_{th} stands for the stochastic force. In scenarios with gas pressures, P_{gas}, smaller than 10 mbar, the drag coefficient can be expressed using the empirical expression [50, 51],

$$\gamma_m \approx 15.8 \frac{R^2 P_{\text{gas}}}{m v_{\text{gas}}}, \tag{2-27}$$

with v_{gas} being the root mean-squared velocity of the gas molecules. As for the term F_{th}, it must comply with

$$\langle F_{\text{th}}(t) \rangle = 0, \tag{2-28a}$$

$$\langle F_{\text{th}}(t) F_{\text{th}}(t+\tau) \rangle = 2m\gamma_m k_B T \delta(\tau), \tag{2-28b}$$

where T is the residual gas temperature, k_B the Boltzmann constant and $\delta(\tau)$ the Dirac delta function. In other words, the values of F_{th} can be described as an additive white Gaussian noise with zero mean and a standard deviation equals to $\sqrt{2m\gamma_m k_B T}$. Even though Eq. (2-26) specifically addresses the variable $z(t)$, expressions for $x(t)$ and $y(t)$ are analogous.

When analysing stochastic signals or systems, frequency domain techniques provide a valuable tool to gain insights. By applying the Fourier transform on Eq. (2-26) we find an expression for $z(t)$ in the Fourier space, denoted as $Z(\Omega)$,

$$Z(\Omega) = -\frac{F_{\text{th}}(\Omega)}{m} \left[\frac{(\Omega^2 - \Omega_z^2) + i\gamma_m \Omega}{(\Omega^2 - \Omega_z^2)^2 + \gamma_m^2 \Omega^2} \right]. \tag{2-29}$$

Now, considering that we carefully conducted a measurement of the signal $z(t)$ with a duration of T_m, we may explore how the power of the random process is distributed across the spectral space by utilizing the power spectral density (PSD). The PSD can be defined in terms of $Z(\Omega)$ and T_m [52, 53],

$$S_{zz}(\Omega) = \lim_{T_m \to \infty} \left[\frac{|Z(\Omega)|^2}{T_m} \right]. \tag{2-30}$$

By utilizing the properties presented in Eq. (2-28) and by substituting Eq. (2-29) into Eq. (2-30) we arrive at the Lorentzian function,

$$S_{zz}(\Omega) = \frac{2\gamma_m k_B T}{m[(\Omega^2 - \Omega_z^2)^2 + \gamma_m^2 \Omega^2]}. \tag{2-31}$$

The PSD is a robust method for calibration of the optical tweezer and for extraction of the parameters γ_m and Ω_z [54–56], and is one of the main

experimental tools used to produced the results in Chapters 4 and 5. Traces and the PSDs produced by numerical simulations of the motion of a nanoparticle are shown in Fig. 2.5. We considered $P_{\text{gas}} = 1\,\text{mbar}$, the other parameters were the same employed to produce Fig. 2.4.

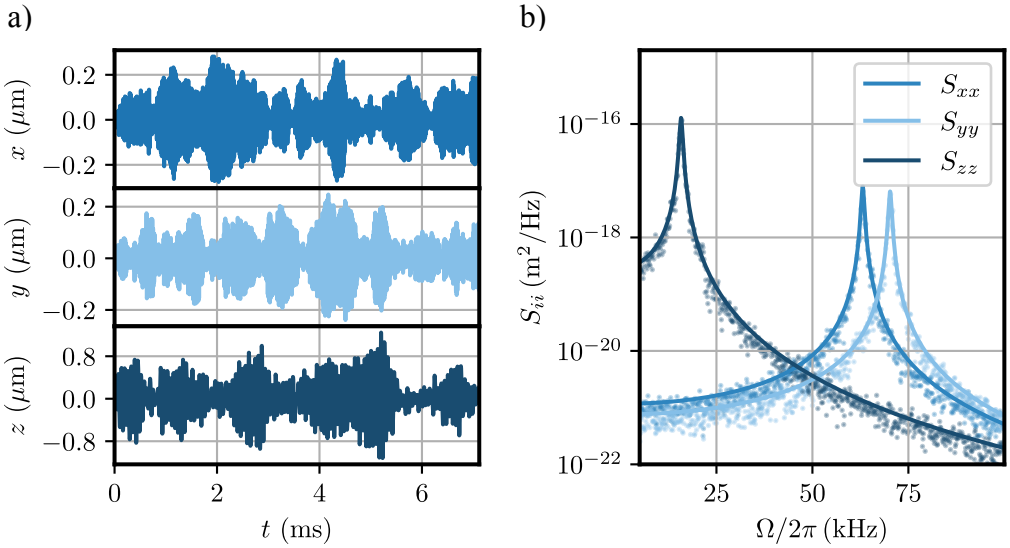

Figure 2.5: Time and frequency behavior of a tweezed nanoparticle under the dipole regime. a) An example of time traces produced using the Euler-Maruyama method to solve Eq. (2-26). b) The PSD (scatter) resulted from the averaging of 50 traces per axis, the solid lines represent fitted Lorentzian curves.

The effective center of mass temperature of the levitated nanoparticle for each axis, T^i_{eff}, can be extracted by integrating the PSD's $S_{ii}(\Omega)$ [15, 57], according to

$$T^i_{\text{eff}} = \frac{m\Omega_i^2}{k_B}\int_0^\infty \left[1 + \left(\frac{\Omega}{\Omega_i}\right)^2\right] S_{ii}(\Omega)\, d\Omega. \tag{2-32}$$

2.4 Anharmonicities in optical tweezers

The harmonic approximation presented in Section 2.2 is widely employed and can precisely describe the motion of a tweezed nanoparticle for sufficiently small displacements, nicely fitting the optical forces around the origin as showed in Fig. 2.4. We may also apply the harmonic approximation to the potential energy U, such that $U \propto r_i^2$, resulting in the plots in Fig. 2.6. As firstly presented in [29], and noticeable in Fig. 2.6, for the case of larger displacements, the particle starts to experience non-linearities in all three axis. The first higher-order mode that dictates the particle's motion results in a Duffing non-linearity, coupling all three degrees of freedom (DOF) [29].

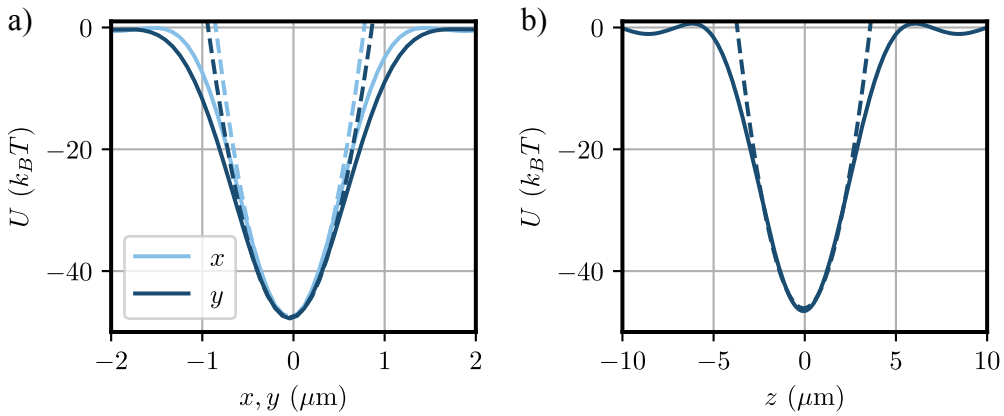

Figure 2.6: Potential landscapes along each axis: a) for x and y, b) for z. The dashed lines represent fitted harmonic potentials, successfully approximating the potential behavior near the origin.

To model these anharmonicities, the resulting field from the integral in Eq. (2-18) is approximated by a Gaussian beam in the vicinity of the focal region [29]. This treatment results in the following equation of motion,

$$\ddot{r}_i(t) + \gamma_m \dot{r}_i(t) + \Omega_i^2(1 + \sum_j \xi_j r_j^2) r_i(t) = \frac{1}{m} F_{\mathrm{th,i}}(t), \tag{2-33}$$

where $\xi_x = -2/w_x^2$, $\xi_y = -2/w_y^2$ and $\xi_z = -2/z_0^2$. Here, w_x and w_y are the beam waist radius of the fitted Gaussian beam and z_0 the fitted Rayleigh range.

3
Control theory for levitodynamics

Control theory constitutes a fundamental area of electrical engineering, representing a well-established field with a rich history of successful applications. These applications span a diverse spectrum, ranging from robotics [58–62] and industrial process control [59, 63] to biomedical engineering [64], and aircraft/spacecraft control [65]. The overarching goal of control theory is to develop and analyze control laws for physical systems or processes [66, 67]. The term *control law* denotes a mathematical function or heuristic designed to guide a system towards a desired pattern of behavior. In most cases, this function depends on a measurement of the system, giving rise to a specific category of control systems known as closed-loop or feedback systems [66]. A block diagram for an elementary feedback control scheme of a single-input single-output (SISO) dynamics is shown in Fig. 3.1.

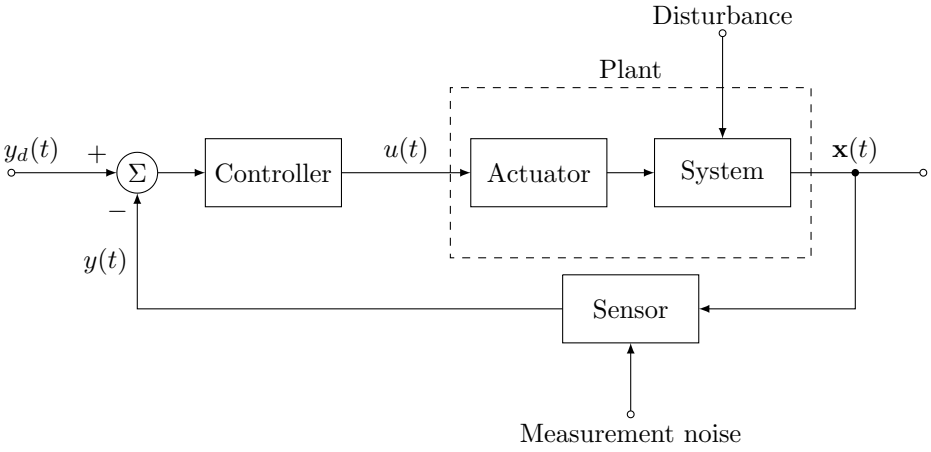

Figure 3.1: Block diagram of a basic feedback control scheme. In this illustration, $\mathbf{x}(t)$ symbolizes the states of the physical system or process, while $y(t)$ represents a real-time measurement output by the sensor. The variable $y_d(t)$ corresponds to the reference or desired value for the measurement, and $u(t)$ denotes the control signal generated by the feedback control system.

In Fig. 3.1, the main component is the plant, formed by the connection of the actuator and the controlled system. The actuator is a device engineered to

influence the system's dynamics through a controllable variable. Albeit it possess its own dynamics, ideally, it produces a linear response based on the controller's output. A disturbance term is included to refer to any external factor associated with non-deterministic events or unmodeled process characteristics. To act on the system, a control signal $u(t)$ is generated by the controller, which usually takes as input the difference between the reference and the measurement.

Control theory has played an essential role in recent advances in the field of levitodynamics. By exploring the use of optical and electrical actuators, researchers have achieved the cooling of levitated nanoparticles to sub-kelvin temperatures [34–37], even reaching its ground state with use of derivative filters [15] or optimal control and estimation techniques [14]. By manipulating the control signal applied, feedback control has also proven to be an important tool to explore non-Markovianity [31] and non-equilibrium dynamics [35, 51, 68].

In conjunction with the comprehension of the system dynamics discussed in Chapter 2, an understanding of the theoretical underpinnings of control theory becomes essential for experimentalists in optomechanics. This chapter is dedicated to presenting the formalism of key control methods. Commencing with optimal control theory for linear deterministic systems, we delve into stochastic control, state estimation and parametric control. Lastly, we finish this chapter with a brief conclusion regarding the presented techniques.

3.1 Optimal control

In many cases, linear control is sufficient to meet technical requirements defined within the application, even at the expense of neglecting stochasticities and other crucial characteristics. Moreover, the fulfilment of these requirements is often related to an iterative trial-and-error process, where various methods are applied until the design meets acceptable or optimized criteria. Optimal control theory emerges as a subarea of control focused in achieving the desired closed-loop behavior while simultaneously extremizing a performance criterion [69]. In this section, we introduce a fundamental control method aimed at minimizing the energy of linear systems. First, it proves useful to express the system's dynamics in a well-established representation within the control theory community— the state-variable representation. This enables the expression of any linear system of arbitrary order as a first-order matrix differential equation.

3.1.1 State-variable representation

Any finite dynamic linear system can be described as a set of first-order ordinary differential equations through the application of the state-variable representation, a methodology widely used in classical control theory. Consider the equation of motion introduced in Eq. (2-26), generalized for all DOF's,

$$\ddot{x}(t) + \gamma_m \dot{x}(t) + \Omega_x^2 x(t) = \frac{1}{m} F_{\mathrm{th,x}}(t), \tag{3-1a}$$

$$\ddot{y}(t) + \gamma_m \dot{y}(t) + \Omega_y^2 y(t) = \frac{1}{m} F_{\mathrm{th,y}}(t), \tag{3-1b}$$

$$\ddot{z}(t) + \gamma_m \dot{z}(t) + \Omega_z^2 z(t) = \frac{1}{m} F_{\mathrm{th,z}}(t). \tag{3-1c}$$

This model presupposes the absence of coupling between motions along distinct axes. It is crucial to underscore that the stochastic forces acting on each axis are independent, leading to the following conditions

$$\langle F_{\mathrm{th,i}}(t) \rangle = 0 \text{ , for } i \in \{x, y, z\}, \tag{3-2a}$$

$$\langle F_{\mathrm{th,i}}(t) F_{\mathrm{th,j}}(t+\tau) \rangle = 2m\gamma_m k_B T \delta_{ij} \delta(\tau) \text{ for } i \in \{x, y, z\}. \tag{3-2b}$$

With the state-variable representation, Eqs. (3-1) can be rewritten as the multiple-input multiple-output (MIMO) system

$$\begin{cases} \dot{\mathbf{x}}(t) = \mathbf{A}\mathbf{x}(t) + \mathbf{B}\mathbf{u}(t) + \mathbf{w}(t), \\ \mathbf{y}(t) = \mathbf{C}\mathbf{x}(t) + \mathbf{D}\mathbf{u}(t) + \mathbf{m}(t). \end{cases} \tag{3-3}$$

Here $\mathbf{A}$, $\mathbf{B}$, $\mathbf{C}$ and $\mathbf{D}$ are referred to as the system, input, output and direct transmission matrices, respectively. The terms $\mathbf{w}(t)$ and $\mathbf{m}(t)$ represent disturbance and measurement noise matrices, respectively. The term $\mathbf{Bu}(t)$ accounts for external forces acting on the particle, initially omitted in Eqs. (3-1). The second line in Eq. (3-3) characterizes the measurement dynamics. For a state vector $\mathbf{x}(t) = \begin{bmatrix} x(t) & y(t) & z(t) & \dot{x}(t) & \dot{y}(t) & \dot{z}(t) \end{bmatrix}^T$, and considering $\mathbf{\Omega}^2 = \begin{bmatrix} \Omega_x^2 & \Omega_y^2 & \Omega_z^2 \end{bmatrix}^T$ and $\mathbf{F}_{\mathrm{th}}(t) = \begin{bmatrix} F_{\mathrm{th,x}}(t) & F_{\mathrm{th,y}}(t) & F_{\mathrm{th,z}}(t) \end{bmatrix}^T$, we have

$$\mathbf{A} = \begin{bmatrix} \mathbf{0}_{3\times3} & \mathbf{I}_3 \\ -\mathrm{diag}(\mathbf{\Omega}^2) & -\gamma_m \mathbf{I}_3 \end{bmatrix}, \qquad \mathbf{w}(t) = \frac{1}{m} \begin{bmatrix} \mathbf{0}_{3\times1} \\ \mathbf{F}_{\mathrm{th}}(t) \end{bmatrix}. \tag{3-4}$$

The input matrix will depend on the constructive characteristics of the actuators, potentially causing coupling between DOF's. The matrices $\mathbf{C}$, $\mathbf{D}$ and $\mathbf{m}$ in the measurement dynamics hinge on the employed detection scheme and characteristics of the detectors. Subsequent sections will present some scenarios, elucidating these terms further.

3.1.2 Minimizing the energy of linear systems

Cooling or reducing the energy of a system can be easily conceptualized as an optimization problem. By considering the linear dynamics given in Eq. (3-3) — temporarily neglecting the random processes $\mathbf{w}(t)$ and $\mathbf{m}(t)$ — we express the system as

$$\dot{\mathbf{x}}(t) = \mathbf{A}\mathbf{x}(t) + \mathbf{B}\mathbf{u}(t). \tag{3-5}$$

Minimizing the total energy of the system involves finding the control policy $\mathbf{u}^*(t)$ which minimizes a positive definite cost function J. For linear systems, quadratic performance criteria are often employed,

$$J = \frac{1}{2}\int_0^\infty \bar{L}(\mathbf{x},\mathbf{u},t)\,dt = \frac{1}{2}\int_0^\infty [\mathbf{x}^T(t)\mathbf{Q}\mathbf{x}(t) + \mathbf{u}^T(t)\mathbf{R}\mathbf{u}(t)]\,dt, \tag{3-6}$$

where $\mathbf{Q}$ is the weighting matrix (a real symmetric positive semi-definite matrix) and $\mathbf{R}$ is the control effort matrix (a real symmetric positive definite matrix). The integrand $\bar{L}(\mathbf{x},\mathbf{u},t)$ in Eq. (3-6) is known as the objective or cost-to-go function. The proportion between the values that constitute $\mathbf{Q}$ and $\mathbf{R}$ signify an intention to maintain $\mathbf{x}(t)$ close to the origin without an excessive expenditure of control effort.

To determine the optimal policy $\mathbf{u}^*(t)$, we rely on one of the milestones in optimal control theory — the Pontryagin's maximum principle [69, 70]. Introducing this principle requires first presenting the concept of the *control Hamiltonian*,

$$\bar{H}(\mathbf{x},\mathbf{u},\mathbf{\Lambda},t) = \bar{L}(\mathbf{x},\mathbf{u},t) + \mathbf{\Lambda}^T(t)\dot{\mathbf{x}}(t). \tag{3-7}$$

The Hamiltonian depends on the objective function, the system's dynamics and, akin to Lagrangian multipliers in static optimization problems, $\mathbf{\Lambda}(t)$, that here assume a time-dependent behavior and constitute what is referred to as the costate vector. Equation (3-7) is equivalent to the Legendre transformation of the Lagrangian [71], denoted in the context of optimal control by the cost-to-go function $\bar{L}(\mathbf{x},\mathbf{u},t)$. The states and costates form a canonical variable pair and, as in classical mechanics, it must obey the Hamilton's equations

$$\left(\frac{\partial \bar{H}(\mathbf{x}(t),\mathbf{u}(t),\mathbf{\Lambda}(t),t)}{\partial \mathbf{\Lambda}}\right)^T = \dot{\mathbf{x}}(t), \tag{3-8a}$$

$$\left(\frac{\partial \bar{H}(\mathbf{x}(t),\mathbf{u}(t),\mathbf{\Lambda}(t),t)}{\partial \mathbf{x}}\right)^T = -\dot{\mathbf{\Lambda}}(t). \tag{3-8b}$$

These expressions set two distinct conditions for the optimal behavior. The Pontryagin's principle arises as third condition with which, when combined with Eqs. (3-8), allows one to find $\mathbf{u}^*(t)$. Considering the state and costate

trajectories for $\mathbf{u}^*(t)$ as $\mathbf{x}^*(t)$ and $\mathbf{\Lambda}^*(t)$, respectively, the maximum principle is written as

$$\frac{\partial \bar{H}(\mathbf{x}^*(t), \mathbf{u}^*(t), \mathbf{\Lambda}^*(t), t)}{\partial \mathbf{u}} = \mathbf{0}. \tag{3-9}$$

Now, by substituting Eqs. (3-5) and (3-6) into (3-8) and (3-9), and applying for optimal trajectories, we find the following three expressions

$$\left(\frac{\partial \bar{H}(\mathbf{x}^*(t), \mathbf{u}^*(t), \mathbf{\Lambda}^*(t), t)}{\partial \mathbf{\Lambda}}\right)^T = \mathbf{A}\mathbf{x}^*(t) + \mathbf{B}\mathbf{u}^*(t) \quad = \quad \dot{\mathbf{x}}^*(t), \tag{3-10a}$$

$$\left(\frac{\partial \bar{H}(\mathbf{x}^*(t), \mathbf{u}^*(t), \mathbf{\Lambda}^*(t), t)}{\partial \mathbf{x}}\right)^T = \mathbf{Q}\mathbf{x}^*(t) + \mathbf{A}^T\mathbf{\Lambda}^*(t) = -\dot{\mathbf{\Lambda}}^*(t), \tag{3-10b}$$

$$\left(\frac{\partial \bar{H}(\mathbf{x}^*(t), \mathbf{u}^*(t), \mathbf{\Lambda}^*(t), t)}{\partial \mathbf{u}}\right)^T = \mathbf{R}\mathbf{u}^*(t) + \mathbf{B}^T\mathbf{\Lambda}^*(t) = \quad \mathbf{0}. \tag{3-10c}$$

The last expression above leads to

$$\mathbf{u}^*(t) = -\mathbf{R}^{-1}\mathbf{B}^T\mathbf{\Lambda}^*(t). \tag{3-11}$$

Due to the system's linearity, we can assume $\mathbf{\Lambda}^*(t) = \mathbf{S}\mathbf{x}^*(t)$ [69]. Replacing $\mathbf{\Lambda}^*(t)$ by its linear relation with the states, we obtain the algebraic Riccati equation

$$\mathbf{S}\mathbf{A} + \mathbf{A}^T\mathbf{S} + \mathbf{Q} - \mathbf{S}\mathbf{B}\mathbf{R}^{-1}\mathbf{B}^T\mathbf{S} = \mathbf{0}. \tag{3-12}$$

Consequently, we conclude that the optimal control policy for a linear system with quadratic criteria is

$$\mathbf{u}^*(t) = -\mathbf{R}^{-1}\mathbf{B}^T\mathbf{S}\mathbf{x}^*(t), \tag{3-13}$$

where $\mathbf{S}$ is the solution of Eq. (3-12). This control law is known as the Linear Quadratic Regulator (LQR), a widely employed and a powerful method for controlling linear systems.

A simulation of the dynamics of a 3D oscillator controlled by LQR is depicted in Fig. 3.2. The frequency vector $\mathbf{\Omega} = \begin{bmatrix}\Omega_x & \Omega_y & \Omega_z\end{bmatrix}^T$ is given by $\Omega_x/2\pi = 63.10\,\mathrm{kHz}$, $\Omega_y/2\pi = 70.24\,\mathrm{kHz}$, $\Omega_z/2\pi = 15.79\,\mathrm{kHz}$, and $\gamma_m = 10\,\mathrm{s}^{-1}$. The input matrix is $\mathbf{B} = \begin{bmatrix}\mathbf{0}_{3\times3} \\ \mathbf{I}_3/m\end{bmatrix}$, the $\mathbf{Q}$ and $\mathbf{R}$ matrices are

$$\mathbf{Q} = m\begin{bmatrix}\mathrm{diag}(\mathbf{\Omega}^2) & \mathbf{0}_{3\times3} \\ \mathbf{0}_{3\times3} & \mathbf{I}_3\end{bmatrix}, \mathbf{R} = \frac{1}{m g_{fb}}\begin{bmatrix}\Omega_x^{-2} & 0 & 0 \\ 0 & \Omega_y^{-2} & 0 \\ 0 & 0 & \Omega_z^{-2}\end{bmatrix}. \tag{3-14}$$

The input matrix results from considering three actuators independently acting on each DOF. The parameter g_{fb} is an adimensional gain, which is varied to

observe the controller's behavior under different control efforts. In Fig. 3.2a) the phase portrait for each DOF demonstrates successful control of both velocity and position and Fig. 3.2b) presents the normalized cost-to-go performance criteria as function of g_{fb}, we isolated the criteria for x, y and z.

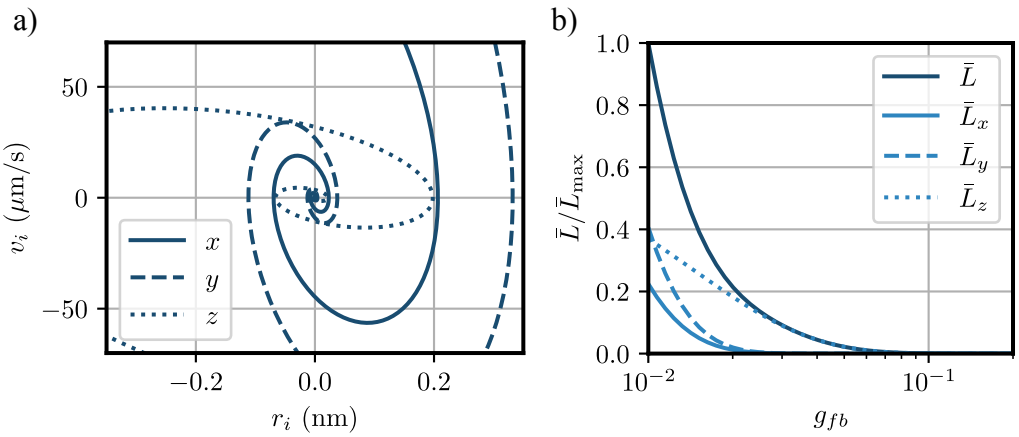

Figure 3.2: Performance of LQR for a 3D harmonic oscillator. a) Phase plot for each axis considering $g_{fb} = 0.5$. b) Cost-to-go performance criteria $\bar{L}/\bar{L}_{\max}$ as a function of g_{fb}. The simulation lasted $20\pi/\Omega_z$, which proved not to be sufficiently long for cooling in cases with small values of g_{fb}.

3.2 Stochastic control

Despite the effectiveness of LQR in minimizing the energy of a linear system, a few considerations are warranted. Firstly, when implementing control methods, the signal $\mathbf{u}(t)$ is going to be computed by a microprocessor or a Field Programmable Gate Array (FPGA). These devices calculate the policy using samples of the measurement signal captured at a specific sampling frequency f_s. This process of discretization, or digitalization, alters our model of the system dynamics [72]. Secondly, the optimal control signal $\mathbf{u}^*(t)$ is computed taking into account the complete state vector $\mathbf{x}(t)$. In the context of levitodynamics, this implies the need for measurement methods for extracting both the position and the velocity (or momentum) of the particle. When measuring only the position, methods to estimate the velocity become necessary. Lastly, it is noteworthy that, up to this point, the disturbances and noises have not been taken into account.

Stochastic control theory emerges as a field focused on studying and analysing dynamical systems subjected to stochastic disturbances. Its goal is to provide tools for problems as stochastic optimal control, states estimation and parametric optimization [61]. In this section we are going to address each one

of the considerations highlighted in the last paragraph. Starting by providing a recursive model for discrete linear systems, we are going to present the Kalman-Bucy filter—an optimal state estimator—and elaborate on how it can be leveraged to formulate an optimal control strategy for stochastic systems.

3.2.1 From a continuous to a discrete-time system

To characterize a discrete-time system, it is customary to first examine the dynamics of its continuous analogue. The solution of the first-order non-homogeneous differential equation expressed in Eq. (3-5) is well-known [66, 72]. Given an initial condition $\mathbf{x}(t_0)$, the expression for $\mathbf{x}(t)$ is

$$\mathbf{x}(t) = e^{\mathbf{A}(t-t_0)}\mathbf{x}(t_0) + \int_{t_0}^{t} e^{\mathbf{A}(t-\tau)}\mathbf{B}\mathbf{u}(\tau)\, d\tau. \tag{3-15}$$

The solution in Eq.(3-15) is the sum between the homogeneous response and the convolution between the external influence term and the state transition matrix $e^{\mathbf{A}t}$. The equation above can be employed to encounter the state vector after a certain time interval, denoted here as T_s. If this interval is sufficiently small we can assume that the signals $\mathbf{x}(t)$ and $\mathbf{u}(t)$ remain constant along T_s and that any time instant can be described as kT_s, with $k \in \mathbb{N}$. By expressing the instant t as $kT_s + T_s$, t_0 as kT_s and considering $\mathbf{u}(\tau) = \mathbf{u}(kT_s)$ for $kT_s \leq \tau \leq kT_s + T_s$, $\mathbf{x}(kT_s + T_s)$ is

$$\mathbf{x}(kT_s + T_s) = e^{\mathbf{A}T_s}\mathbf{x}(kT_s) + \int_{kT_s}^{kT_s+T_s} e^{\mathbf{A}(kT_s+T_s-\tau)}\mathbf{B}\mathbf{u}(kT_s)\, d\tau, \tag{3-16}$$

which can be directly reduced to the first-order difference equation

$$\mathbf{x}_{n+1} = \mathbf{A}_d\mathbf{x}_n + \mathbf{B}_d\mathbf{u}_n, \tag{3-17}$$

where

$$\mathbf{A}_d = e^{\mathbf{A}T_s} \text{ and } \mathbf{B}_d = \left(\int_0^{T_s} e^{\mathbf{A}\eta}\, d\eta\right)\mathbf{B}, \text{ with } \eta = kT_s + T_s - \tau. \tag{3-18}$$

These matrices can be encountered by considering the Taylor expansion of $e^{\mathbf{A}T_s}$, leading to

$$\mathbf{A}_d = \sum_{k=0}^{\infty} \frac{T_s^k}{k!}\mathbf{A}^k \text{ and } \mathbf{B}_d = (\mathbf{A}_d - \mathbf{I})\mathbf{A}^{-1}\mathbf{B}. \tag{3-19}$$

The procedure just described is equivalent to the zero-order holder sampling method, applied for a sampling time T_s, or, sampling frequency $f_s = 1/T_s$. This stands as a fundamental method for time-discretization [67], and its impact on the temporal behavior of a continuous-time signal is illustrated in Fig. 3.3. Through this method, we have established a means

to express the system evolution as a recursive equation. While there are cases where discretization may be negligible, as for example when implementing control algorithms with sufficiently fast hardware, it is imperative to consider it, specially for signal processing purposes such as filtering and estimation.

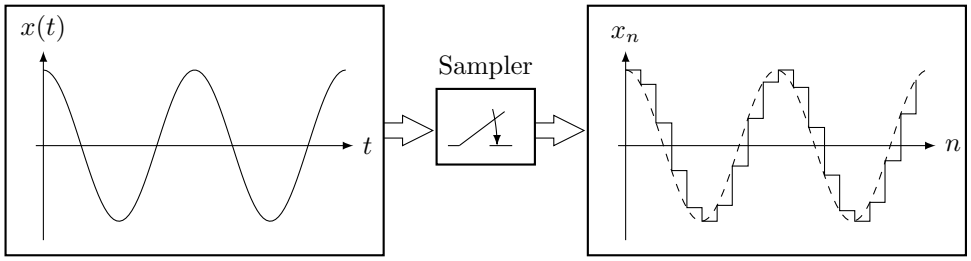

Figure 3.3: Sampling process utilizing a zero-order holder.

Until this point we have focused solely in the system dynamics. However, without any difficulties we can generalize the discretization process for the measurement equation. Also, stochastic disturbance and measurement noise can be added to the expression, yielding

$$\mathbf{x}_{n+1} = \mathbf{A}_d\mathbf{x}_n + \mathbf{B}_d\mathbf{u}_n + \mathbf{w}_{d,n}, \tag{3-20a}$$

$$\mathbf{y}_{n+1} = \mathbf{C}_d\mathbf{x}_{n+1} + \mathbf{D}_d\mathbf{u}_{n+1} + \mathbf{m}_{d,n+1}, \tag{3-20b}$$

where, $\mathbf{C}_d = \mathbf{C}$ and $\mathbf{D}_d = \mathbf{D}$, and $\mathbf{w}_d(t)$ and $\mathbf{m}_d(t)$ are zero-mean discrete-time white noise with covariances equals to $\mathbf{W}$ and $\mathbf{M}$, respectively. The term $\mathbf{D}_d$ was included just to present the more general formulation, even though in our scenario $\mathbf{D}_d = \mathbf{0}$. With the formulation presented in Eq. (3-20) we have taken into consideration one of the three points listed in the beginning of Section 3.2.

3.2.2
Kalman filter, an optimal state estimator

In both deterministic and stochastic systems, the reconstruction of the state vector $\mathbf{x}_n$ holds significant importance in the computation of control laws. The problem of estimation is articulated as follows: given the measurement equation in Eq. (3-20), estimation involves determining the state or signal $\mathbf{x}_k$ based on a set of measurements $\mathscr{Y}_n = \{\mathbf{y}_i|, i \in \mathbb{N}, , 0 \leq i \leq n\}$. This gives rise to three distinct situations:

- *Smoothing*, if $n > k$,
- *Prediction*, if $n < k$,
- *Filtering*, if $n = k$.

Throughout this subsection, our emphasis will primarily be on the last case, although the other situations can be of interest in alternative applications [73, 74]. Before examining the filtering problem in more detail, we establish two conditions necessary for implementing an estimator. First, for accurate state estimation, the system dynamics and noise characteristics must be known and precisely defined. Second, given the estimation error $\mathbf{e}_n = \mathbf{x}_n - \hat{\mathbf{x}}_n$, a suitable cost function or optimization criterion $\mathcal{L}(\mathbf{e}_n)$ must be chosen, such that the optimal estimate $\hat{\mathbf{x}}_n$ of $\mathbf{x}_n$ minimizes $\langle \mathcal{L}(\mathbf{e}_n) \rangle$. If $\mathcal{L}(\mathbf{e}_n)$ is even, non-decreasing for $\mathbf{e}_n \geq 0$, and positive definite, then the optimal estimate $\hat{\mathbf{x}}_n^*$ is

$$\hat{\mathbf{x}}_n^* = \langle \mathbf{x}_n \rangle. \tag{3-21}$$

The proof of this assertion can be found in Appendix B.1 and in the stochastic control literature [61, 75]. This expression provides the initial optimal estimation $\hat{\mathbf{x}}_0^* = \langle \mathbf{x}_0 \rangle$. To determine $\hat{\mathbf{x}}_n^*$ for any time-step n, it is important to comprehend how to propagate the average given by the initial estimation, balancing between knowledge of the theoretical model of the dynamics and measurements acquired through the iterations. For linear dynamics, where both disturbances and noises are white-noises processes, and considering a quadratic criterion, analogous to the cost-to-go function used in Subsection 3.1.2,

$$\mathcal{L}(\mathbf{e}_n) = \frac{1}{2} \langle \mathbf{e}_n^T \mathbf{e}_n \rangle, \tag{3-22}$$

the optimal estimation is given by the Linear Quadratic Estimator (LQE), commonly known as the Kalman filter, firstly proposed by [76].

As we considered the system to be subject only to white-noise processes, the statistical behavior of $\mathbf{x}_n$ can be fully described by its mean $\langle \mathbf{x}_n \rangle$ and covariance matrix, $\mathbf{P}_n$. Upon establishing the initial estimation $\langle \mathbf{x}_0 \rangle$, the covariance matrix can be computed. However, since $\hat{\mathbf{x}}_0 = \langle \mathbf{x}_0 \rangle$ and given the definition of the estimation error, the covariance matrix $\mathbf{P}_0$ can be renamed to what is known as the *error covariance matrix*, since

$$\mathbf{P}_0 = \langle (\mathbf{x}_0 - \langle \mathbf{x}_0 \rangle)(\mathbf{x}_0 - \langle \mathbf{x}_0 \rangle)^T \rangle = \langle \mathbf{e}_0 \mathbf{e}_0^T \rangle. \tag{3-23}$$

After the initialization, the first step of the Kalman filter involves predicting the behavior of $\mathbf{x}_1$ and $\mathbf{P}_1$ given information of the system dynamics previously provided to the algorithm. Appendix B.2 details the propagation of the average and covariance of a state vector $\mathbf{x}_n$. By applying Eqs. (B-9) and (B-12), $\hat{\mathbf{x}}_1$ and $\mathbf{P}_1$ are

$$\hat{\mathbf{x}}_1 = \mathbf{A}_d \hat{\mathbf{x}}_0 + \mathbf{B}_d \mathbf{u}_0, \tag{3-24a}$$

$$\mathbf{P}_1 = \mathbf{A}_d \mathbf{P}_0 \mathbf{A}_d + \mathbf{W}, \tag{3-24b}$$

where $\hat{\mathbf{x}}_1$ also obeys

$$\hat{\mathbf{x}}_1 = \langle \mathbf{x}_1 \rangle. \tag{3-25}$$

Subsequently, at the new time-step, after the propagation, a measurement $\mathbf{y}_1$ becomes available, offering new information regarding the state vector. If Eq. (3-25) is adhered to, it is possible to optimally estimate and correct the $\hat{\mathbf{x}}_1$ based on $\mathbf{y}_1$ by applying the least-square method (we refer to Appendix B.3 for more details). To distinguish between estimates made before and after acquiring a new value $\mathbf{y}_n$, we introduce the terms *a priori* (for before $\mathbf{y}_n$), denoted as $\hat{\mathbf{x}}_n^-$ and $\mathbf{P}_n^-$, and *a posteriori* (for after $\mathbf{y}_n$), denoted as $\hat{\mathbf{x}}_n^+$ and $\mathbf{P}_n^+$. The corrections from the least-squares method are

$$\hat{\mathbf{x}}_1^+ = \hat{\mathbf{x}}_1^- + \mathbf{K}_1(\mathbf{y}_1 - \mathbf{C}_d\hat{\mathbf{x}}_1^-), \tag{3-26a}$$

$$\mathbf{P}_1^+ = (\mathbf{I} - \mathbf{K}_1\mathbf{C}_d)\mathbf{P}_1^-(\mathbf{I} - \mathbf{K}_1\mathbf{C}_d)^T + \mathbf{K}_1\mathbf{M}\mathbf{K}_1^T, \tag{3-26b}$$

where

$$\mathbf{K}_1 = \mathbf{P}_1^-\mathbf{C}_d^T(\mathbf{C}_d\mathbf{P}_1^-\mathbf{C}_d^T + \mathbf{M})^{-1}. \tag{3-27}$$

Now, by amalgamating the expressions for *a priori* and *a posteriori* estimates and generalizing the recursive expression for any value of n, we obtain

$$\hat{\mathbf{x}}_n^- = \mathbf{A}_d\hat{\mathbf{x}}_{n-1}^+ + \mathbf{B}_d\mathbf{u}_n, \tag{3-28a}$$

$$\mathbf{P}_n^- = \mathbf{A}_d\mathbf{P}_{n-1}^+\mathbf{A}_d + \mathbf{W}, \tag{3-28b}$$

$$\mathbf{K}_n = \mathbf{P}_n^-\mathbf{C}_d^T(\mathbf{C}_d\mathbf{P}_n^-\mathbf{C}_d^T + \mathbf{M})^{-1}, \tag{3-28c}$$

$$\hat{\mathbf{x}}_n^+ = \hat{\mathbf{x}}_n^- + \mathbf{K}_n(\mathbf{y}_n - \mathbf{C}_d\hat{\mathbf{x}}_n^-), \tag{3-28d}$$

$$\mathbf{P}_n^+ = (\mathbf{I} - \mathbf{K}_n\mathbf{C}_d)\mathbf{P}_n^-(\mathbf{I} - \mathbf{K}_n\mathbf{C}_d)^T + \mathbf{K}_n\mathbf{M}\mathbf{K}_n^T. \tag{3-28e}$$

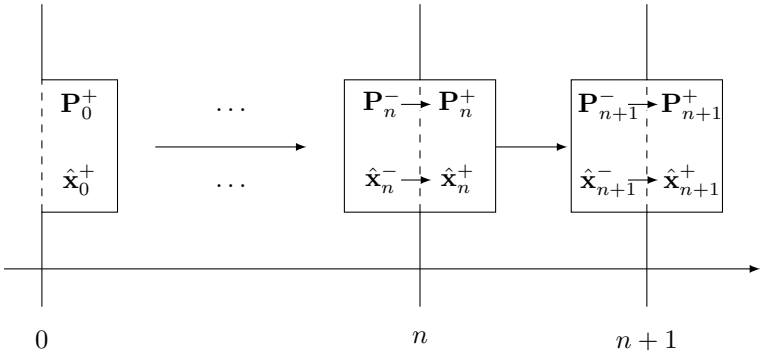

Figure 3.4: Kalman filter timeline for *a posteriori* and *a priori* terms.

To better illustrate the temporal relation between each estimate, Fig. 3.4 depicts the signal timeline where the relation between $\hat{\mathbf{x}}_n^-$, $\mathbf{P}_n^-$, $\hat{\mathbf{x}}_n^+$ and

$\mathbf{P}_n^+$ is shown. In Fig. 3.5 we present the simulation of a Kalman filter applied to estimate the coordinates and velocities of the 3D motion of a confined nanoparticle. The simulation employs the same parameters of previous simulations, except for a modification in the value of γ_m, which now is the resulting damping factor for a pressure of 10^{-5} mbar. For the output matrix we considered $\mathbf{C} = \begin{bmatrix}\mathbf{I}_3 & \mathbf{0}_{3\times3}\end{bmatrix}$, accompanied by zero-mean measurement noise characterized by a standard deviation of ≈ 0.8 nm. As evidenced by the simulated traces, the filtering algorithm adeptly estimated all the states.

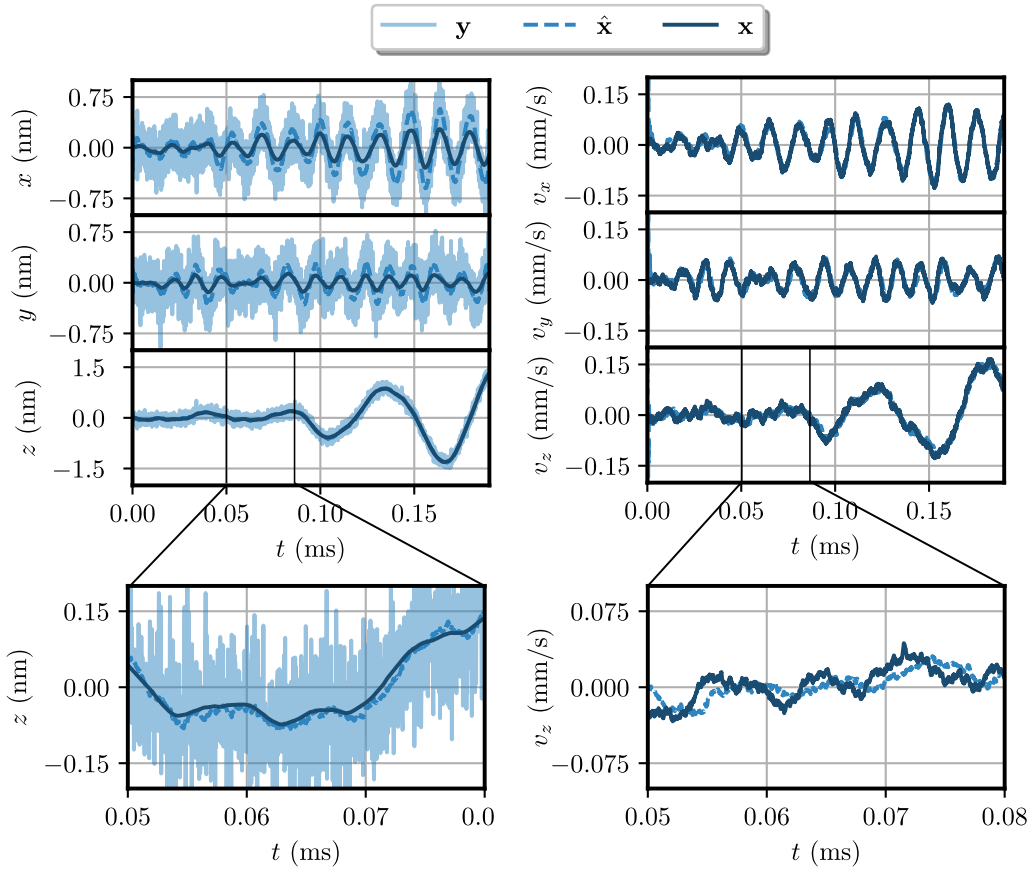

Figure 3.5: Kalman filter estimates for an optically levitated particle. The results shows the estimates convergence towards the actual states. The estimation error becomes more discernible in the insets presented in the lower part of the figure, providing a detailed view of the discrepancies.

One may question the importance of the filter initialization. While initialization plays a crucial role in its mathematical formulation and proof of optimality, incorrect initialization can still result to accurate estimation [77, 78]. However, this may prolong the time required for correct estimation and hinder the minimization of the overall cost function $\sum^{n} \mathcal{L}(\mathbf{e_n})$.

3.2.3 Optimal stochastic control

The problem of optimal control outlined in Section 3.1 can be reformulated to accommodate incomplete state information, time discretization, disturbances and measurement noise. To achieve this, we must first define a new cost function J_d, tailored for the stochastic discrete system,

$$J_d = \frac{1}{N}\sum_{n=0}^{N}\left\langle \frac{1}{2}[\mathbf{x}_n^T\mathbf{Q}\mathbf{x}_n + \mathbf{u}_n^T\mathbf{R}\mathbf{u}_n]\right\rangle. \tag{3-29}$$

Kalman's contributions weren't limited only to the formulation of LQE. His contributions also unveiled a duality between control and estimation (or observation) in linear systems [79]. While the generalization of this duality has proven challenging, the LQR and LQE have shown to form a robust pair for linear control, with each serving as the optimal solution for its respective problem. To determine the optimal control policy $\mathbf{u}_n^*$ that minimizes Eq. (3-29) we can employ a fundamental principle in stochastic control theory known as the separation principle [61].

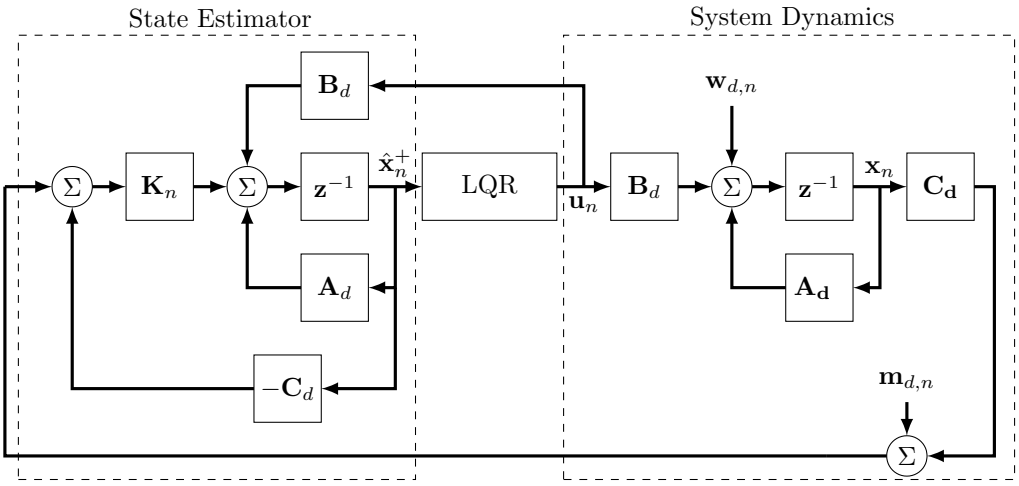

Figure 3.6: Block diagram for the LQG controller. Sub-blocks delimited by dashed lines represent system dynamics and state estimation. Middle block accounts for control gain computation.

The separation principle divides the optimal control problem into sub-problems of estimation and control. It states that the overall optimal solution is found by encountering the optimal solution for each sub-problem individually. Therefore, the optimal control law for the aforementioned criteria integrates concepts of Section 3.1 and Subsections 3.2.1 and 3.2.2, yielding [61, 80]

$$\mathbf{u}_n^* = -(\mathbf{R} + \mathbf{B}_d^T\mathbf{S}_d\mathbf{B}_d)^{-1}\mathbf{B}_d^T\mathbf{S}_d\mathbf{A}_d\hat{\mathbf{x}}_n^+, \tag{3-30}$$

where $\mathbf{S}_d$ is the solution of the discrete-time algebraic Ricatti equation.

This control method is known as the Linear Quadratic Gaussian (LQG) control law. In Fig. 3.6, a diagram of the closed-loop system, including state estimation, is presented. The diagram represents the discrete-time representation of the system dynamics. The block $\mathbf{z}^{-1}$ is the unitary delay block, which when applied to $\mathbf{x}_n$ returns $\mathbf{x}_{n-1}$. By simulating a levitated nanoparticle with the same parameters used in the LQR and Kalman filter simulations previously shown, we obtain the results depicted in Fig. 3.7.

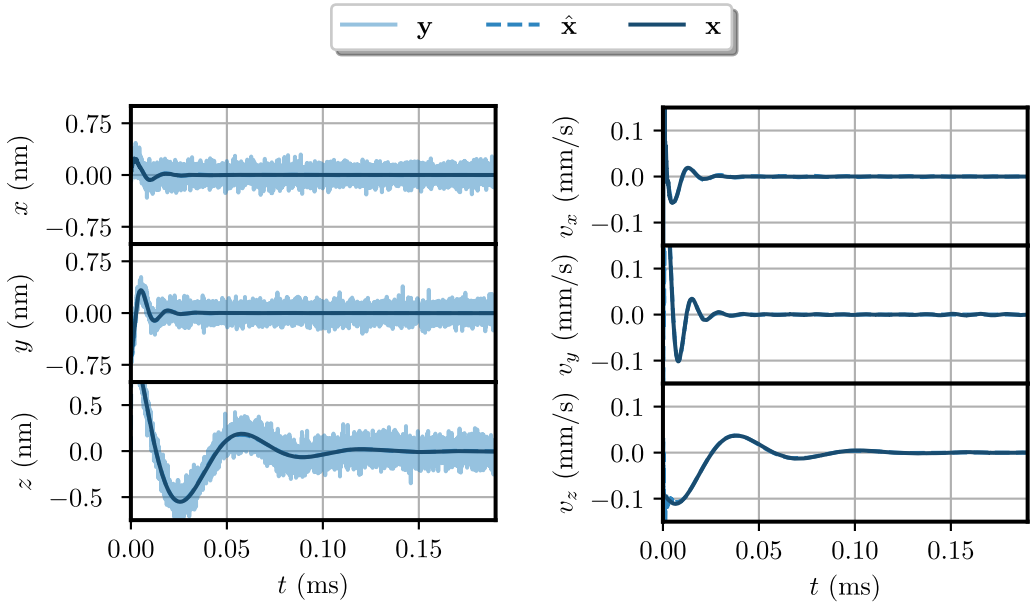

Figure 3.7: Simulation of the LQG controller applied to a levitated nanoparticle. Simulation conducted considering incorrect initialization of the LQE, still, the filtering method achieved indistinguishability between $\mathbf{x}$ and $\hat{\mathbf{x}}$.

3.3 Parametric control

Up to this point, the previously presented control methods have computed $\mathbf{u}(t)$ as linear functions of $\mathbf{x}(t)$, not jeopardizing the system's linearity [81]. An emerging class of control techniques, particularly advantageous for thermal processes [81] and extensively applied in levitodynamics [14, 15, 34, 36, 37], are the parametric controllers. In contrast to classical control methods, parametric control acts on a system parameter. For instance, in parametric cooling, the trap stiffness is modulated with a frequency Ω_m, introducing an extra force term

$$\mathbf{F}_p(\mathbf{r}, t) = 2m \sum_{j\in\{x,y,z\}} \Omega_j^{*\,2} \cos(\Omega_{m,j} t + \phi_i)\mathbf{r}, \tag{3-31}$$

with $\mathbf{\Omega}^{*2} = \begin{bmatrix}\Gamma_x\Omega_x & \Gamma_y\Omega_y & \Gamma_z\Omega_z\end{bmatrix}^T$ and $\mathbf{r} = \begin{bmatrix}x & y & z\end{bmatrix}^T$. The modulation frequency can be defined as $\Omega_{m,i} = 2\Omega_i$ and $\Gamma_i = b_i\Omega_i$, with b_i being the modulation factor for the i-axis. To illustrate the mechanism behind parametric cooling, let us first analyse the one-dimensional equation of motion as presented in [82], considered here for the z-axis. We will consider only the deterministic forces acting upon the particle and neglect any effect related to time-discretization. Also, for now, we consider modulation only in Ω_z, resulting in

$$\ddot{z}(t) = -\gamma_m\dot{z}(t) - \Omega_z^2 z(t) + 2b_z\Omega_z^2\cos(2\Omega_z t + \phi_z)z(t). \tag{3-32}$$

Assuming $z(t) = \bar{z}(t)e^{-\gamma_m t/2}$ and $\bar{t} = \Omega_z t + \phi_z$, and considering $\Omega_z \approx \sqrt{\Omega_z^2 - \frac{\gamma_m^2}{4}}$, which is true for sufficiently low pressures, Eq. (3-32) can be reformulated as a Mathieu differential equation,

$$\frac{d^2\bar{z}(\bar{t})}{d\bar{t}^2} + \left[1 - 2b_z\cos\left(2\bar{t}\right)\right]\bar{z}(\bar{t}) = 0. \tag{3-33}$$

As demonstrated in [82], the solution of Eq. (3-33) can be approximated as

$$z(t) = A_- e^{-\frac{(\gamma_m+\Gamma_z)t}{2}}\cos(\Omega_z t + \phi_z) + A_+ e^{-\frac{(\gamma_m-\Gamma_z)t}{2}}\sin(\Omega_z t + \phi_z). \tag{3-34}$$

Here, A_- and A_+ are constants defined by the initial conditions of the problem, such that

$$A_- = \frac{[-(\gamma_m - \Gamma_z)\sin\phi_z + 2\Omega_z\cos\phi_z]z_0 - 2\sin\phi_z\dot{z}_0}{2(\Omega_z + \Gamma_z\sin\phi_z\cos\phi_z)}, \tag{3-35a}$$

$$A_+ = \frac{[(\gamma_m + \Gamma_z)\cos\phi_z + 2\Omega_z\sin\phi_z]z_0 + 2\cos\phi_z\dot{z}_0}{2(\Omega_z + \Gamma_z\sin\phi_z\cos\phi_z)}. \tag{3-35b}$$

Further examination of Eq. (3-34) reveals that with increasing time, and for pressures such that $\gamma_m < \Gamma_z$, the second term on the left side will start to dominate, causing heating and leading to instability, potentially removing the particle from the optical trap. Balancing between heating and cooling is possible by adjusting the phase ϕ_z. To maintain stability during phase drifts, active feedback is essential for stable cooling [34, 82, 83]. Experimentally, modulation of the trap stiffness can be achieved by adjusting the total optical power of the trapping beam, with the modulation locked to the phase of the particle's motion using a Phase Lock-in Loop (PLL).

Parametric cooling has been successfully applied in several works in the levitodynamics literature [14, 15, 34, 36, 37, 51]. Although the presented treatment focuses on one-dimensional motion, this control scheme is applicable for 3D cooling, provided there are no degenerate modes ($\Omega_i \neq \Omega_j$ for $i \neq j$). However, as indicated by Eq. (3-31), the component of $\mathbf{F}_p$ acting on each axis

depends on the modulation frequency of all three DOFs, as power modulation affects the particle's motion entirely. In Figure 3.8, simulation results show the transient effective temperature, computed with Eq. (2-32), of a particle subject to parametric cooling.

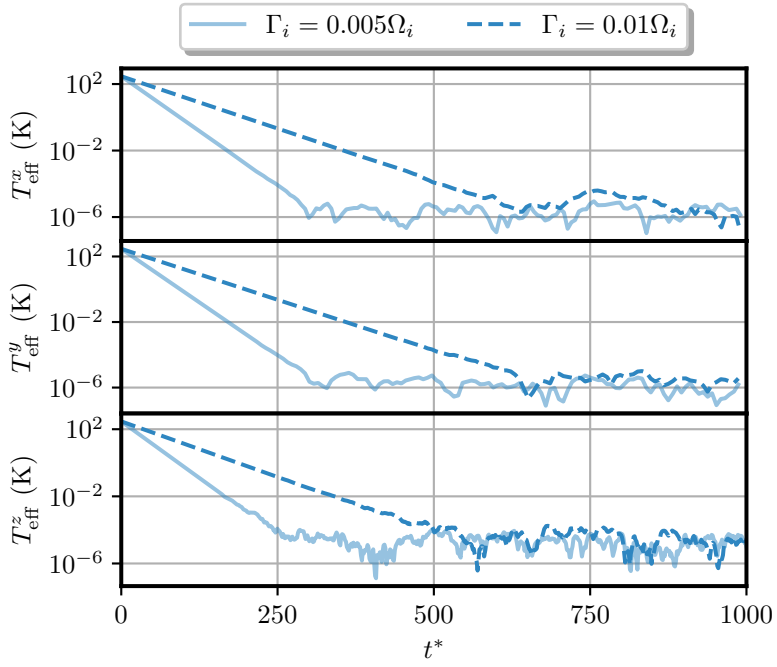

Figure 3.8: Simulation of parametric cooling. Parametric cooling successfully reduces the effective temperature for each axis of a tweezed nanoparticle for two different values of modulation amplitudes. The timescale used, t^*, is t normalized by a factor $2\pi/\Omega_i$.

3.4 Conclusion

Control methods have been successfully applied to levitodynamics, employing well-established methodologies such as proportional-derivative controllers and innovative techniques like parametric control. In this chapter, we briefly presented some of the most relevant methods applied in optomechanical cooling. The simulations presented considered the tweezed nanoparticle as a classical system, not accounting for quantum aspects such as measurement uncertainty or back-action. Despite this, the importance of these simulations in showcasing the potential to reduce the system's energy, even reaching sub-kelvin temperatures, remains significant.

4
Perturbative nonlinear feedback forces for optical levitation experiments

As mentioned in the beginning of Chapter 3, the introduction of an additional force term to influence the particle's motion, facilitated by feedback loops, has proven to be a powerful tool for exploring non-equilibrium dynamics and non-markovianity [31, 35, 51, 68]. This approach can also be applied to enhance our understanding of how trapped nano-objects behave when subjected to nonlinear forces. The theoretical predictions concerning the effects of perturbative nonlinear forces on the motion of tweezed nanoparticles were presented in [30]. In this chapter, we report the experimental validation of these predictions, specifically focusing on the underdamped regime. The findings reported here were published in [84]. Its content follows just as in the article, minor adjustments were made to the notation for consistency within this dissertation. Lastly, the supplementary material from the publication has been consolidated into the Section 4.5.

4.1
Introduction

Optical levitation of nanoparticles provides a robust setup for both fundamental and applied physics [4, 85], from classical stochastic thermodynamics [86–89] to mesoscopic quantum science [26, 90, 91]. In the typical levitated optomechanics experiment, a dielectric particle is trapped in a tightly focused Gaussian beam providing, to leading order approximation, a confining harmonic potential [42, 56]. The particle undergoes Brownian motion due to interaction with its surrounding medium and measurements of its position correlation functions, notably the auto-correlation and the associated power spectrum, allows for the characterization of the trap's parameters [56, 92].

While the harmonic approximation is commonly employed in optical trapping, the ability to engineer potential landscapes beyond the quadratic approximation is central to optomechanics. Nonlinear force landscapes are a valuable resource to nonequilibrium Brownian machines [93, 94], the preparation of non-classical and non-Gaussian quantum states [95] and matter wave interference experiments [96], to mention just a few examples. Nonlinear

potential landscapes also appear in structured light optical tweezers [97], as in double-well landscapes [98–101], structured light beams with pattern revivals [102], cylindrical vector beams [103] and dark focus traps [104, 105].

In these nonlinear potential landscapes, to which we refer here as *nonlinear optical tweezers*, quantitative statistical description of the stochastic particle motion is significantly more complicated as it involves nonlinear stochastic differential equations. To make quantitative predictions regarding the statistical correlators of the trapped particle's motion we can, however, resort to perturbation theory [106].

A perturbative method for nonlinear optical tweezers has been developed in [30], wherein it is possible to compute corrections to the statistical moments of particle motion, in particular the position power spectrum. The purpose of the present work is to experimentally validate these methods. In standard Gaussian optical tweezers, the ratio between linear and nonlinear spring constants cannot be varied independently, given that both scale linearly with the trapping power [29, 107]. Thus, we turn to effective feedback potential landscapes to implement nonlinear position-dependent forces upon a levitated nanosphere. We implement the nonlinearity via electric feedback and characterize its effects on the particle motion.

This article is organized as follows. In the next section, we briefly review the perturbation theory for computing corrections to the correlation functions of a trapped particle under the influence of a nonlinear force, and generalize it to include the effect of delayed forces. Since we deal with artificial electric feedback potentials relying on measurements and processing of the trapped particle's position, they imply an inherent delay to the nonlinear force and therefore accounting for the effects of this delay is essential to validating the methods of [30]. We then describe the experimental setup used to generate nonlinear potential landscapes through electric feedback on the particle and numerically compute the effects of delay, showing that within the range of parameters employed in our experiment they are negligible. We implement a cubic force (quartic potential) on the particle and finally verify the perturbation theory by comparing the predicted center frequency of the position power spectral density with experimental results. We conclude with a brief discussion on the applications of artificial nonlinear forces to levitated optomechanics experiments.

4.2 Theory

4.2.1 Formulation of the perturbation theory

We model the stochastic motion of a particle in a fluid at thermal equilibrium at temperature T and under a force field $F(r_i)$ using the Langevin equation,

$$\ddot{r}_i(t) = -\gamma_m \dot{r}_i(t) + F(r_i(t))/m + \sqrt{C}\eta_i(t), \tag{4-1}$$

where m is the particle's mass, $\gamma_m = \gamma/m$, $C = 2\gamma k_B T/m^2$ with γ the drag coefficient and $\eta_i(t)$ is isotropic Gaussian white noise, whose components satisfy

$$\mathbb{E}[\eta_i(t)\eta_j(t')] = \delta_{ij}\delta(t-t'). \tag{4-2}$$

Concentrating in the motion along the longitudinal z-direction, Eq. (4-1) reduces to a one dimensional Langevin equation

$$\ddot{z}(t) = -\gamma_m \dot{z}(t) + F_z(z(t))/m + \sqrt{C}\eta(t). \tag{4-3}$$

For an approximately linear trapping force perturbed by nonlinear corrections, the steady state position auto-correlation $A(t) \equiv \mathbb{E}[z(t)z(0)]$ can be perturbatively approximated. We next summarize the perturbation theory outlined in [30] and used throughout this work.

Consider the force acting on the particle,

$$F_z(z) = -m\Omega_z^2 z - G_{fb}z^3, \tag{4-4}$$

where the first term accounts for an optical trap with resonance frequency Ω_z and the second term is a small nonlinear correction, which in the experiment originates from a feedback force on the particle proportional to the *feedback gain* G_{fb} times a nonlinear function of the particle's position. We define the Green's function

$$G(t) = \frac{\sin(\Omega_z' t)}{\Omega_z'} \exp\left(-\frac{\gamma_m t}{2}\right) H(t), \tag{4-5}$$

where $\Omega_z' = \sqrt{\Omega_z^2 - \gamma_m^2/4}$ and $H(t)$ is the Heaviside step function with $H(t) = 1$ for $t > 0$ and $H(t) = 0$ for $t \leq 0$. We introduce the auxiliary variable (also referred to as the response paths) $\tilde{z}(s)$ and define the Wick sum bracket $\langle(\cdots)\rangle_0$:

$$\langle z(t_1)\cdots z(t_n)\tilde{z}(s_1)\cdots\tilde{z}(s_m)\rangle_0 = \delta_{nm}\sum_{\sigma}\prod_{j=1}^{n} G(t_j - s_{\sigma(j)}) \tag{4-6}$$

where the sum goes over all permutations σ of indexes $\{1,\ldots,n\}$. The response variables $\tilde{z}(s)$ can be understood as auxiliary integration variables in a stochastic path integral defining the perturbation theory expansion; we

refer to [30, 106] for details on stochastic perturbation methods. Note that the second order correlator is given by the Green function, $\langle z(t)\tilde{z}(s)\rangle_0 = G(t-s)$. The perturbation theory is summarized by the expression for the position auto-correlation function,

$$A(t) \equiv \mathbb{E}[z(t)z(0)] = \langle z(t)z(0)e^{\frac{C}{2}\int \tilde{z}^2(s)ds} e^{\frac{G_{fb}}{m}\int \tilde{z}^3(t')z(t')dt'}\rangle_0, \tag{4-7}$$

where the right-hand side is defined by expanding both exponentials inside the brackets as a power series in C and in G_{fb}/m and interchanging summations and integrations by applying the Wick bracket $\langle(\cdots)\rangle_0$. Note that only brackets with an equal number of z and $\tilde{z}$ variables are non-vanishing [30, 106].

The first non-vanishing term in the expansion of Eq. (4-7) is

$$\frac{C}{2}\int \langle z(t)z(0)\tilde{z}^2(s)\rangle_0\, ds = C\int G(t-s)G(-s)ds\ , \tag{4-8}$$

which gives the auto-correlation for the case of a linear force $F_z(x) = -m\Omega_z^2 z$,

$$A(t)_{(G_{fb}=0)} = \frac{Ce^{-\gamma_m|t|/2}(2\Omega_z' \cos\Omega_z'|t| + \gamma_m \sin\Omega_z'|t|)}{\gamma_m\Omega_z'(\gamma_m^2 + 4\Omega_z'^2)}. \tag{4-9}$$

The leading order correction in the feedback gain reads,

$$\Delta A(t) \equiv \frac{C^2 G_{fb}}{8m}\int \langle \tilde{z}^2(s_1)\tilde{z}^2(s_2)\tilde{z}(t_1)z^3(t_1)z(t)z(0)\rangle_0\, ds_1 ds_2 dt_1. \tag{4-10}$$

Expanding the brackets using (4-6) would produce a sum with $5! = 120$ terms, but many of these vanish since $\langle\tilde{z}(t_1)z(t_1)\rangle = G(0) = 0$. Moreover, by symmetry of the integration variables s_1 and s_2, the contribution to the integral of the non-vanishing terms is equal to the contribution of $G(t-t_1)G(-s_1)G(t_1-s_1)G^2(t_1-s_2)$ or $G(-t_1)G(t-s_1)G(t_1-s_1)G^2(t_1-s_2)$. Therefore, the integral in (4-10) is computed by integrating these two terms over t_1, s_1, s_2 and multiplying both integrals by a multiplicity factor $2^3(3!) = 48$. We note that a diagrammatic expansion can be employed to organize non-vanishing terms in the Wick sum; for more details we refer to [30].

From the auto-correlation function perturbation ΔA we can obtain the correction in the PSD of the particle motion by taking the Fourier transform [30],

$$\Delta S = \frac{3G_{fb}C^2}{\gamma_m\Omega_z^2}\frac{\Omega^2 - \Omega_z^2}{[\gamma_m^2\Omega^2 + (\Omega^2 - \Omega_z^2)^2]^2}. \tag{4-11}$$

The PSD of the motion of a particle with unperturbed resonance frequency Ω_z subject to a frequency shift $\Delta\Omega$ can be expanded to first order as:

$$\frac{C}{\gamma_m^2\Omega^2 + [\Omega^2 - (\Omega_z + \Delta\Omega)^2]^2} \approx \frac{C}{\gamma_m^2\Omega^2 + (\Omega^2 - \Omega_z^2)^2}$$

$$+ 4C\Omega_z\Delta\Omega\frac{\Omega^2-\Omega_z^2}{[\gamma_m^2\Omega^2+(\Omega^2-\Omega_z^2)^2]^2}, \quad (4\text{-}12)$$

Comparing the first order correction in Eq. (4-12) with the correction in Eq. (4-11), we conclude that the nonlinearity causes a frequency shift given by:

$$\frac{\Delta\Omega}{2\pi} = \frac{3k_BT}{4\pi m^2\Omega_z^3}G_{fb} \equiv \kappa G_{fb}. \quad (4\text{-}13)$$

We see that effectively, the nonlinear perturbation manifests as a shift in the PSD central frequency scaling linearly with the feedback gain G_{fb} and with a slope given by the constant κ. This is valid for small G_{fb},

$$G_{fb} \ll \frac{m^2\Omega_z^4}{2k_BT}. \quad (4\text{-}14)$$

The right-hand side of (4-14) can be used to delimit the validity region of perturbation theory. The shift $\Delta\Omega$ in the central frequency of the PSD is the experimental signature which we use as an indicator of the effect of nonlinear perturbations. It is worth noticing that the shift described by (4-13) also includes intrinsic nonlinearities of the tweezer, which arise due to anharmonicities of the trapping potential [29]. Note, however, that only relative shifts to the original resonance frequency (with the cubic feedback off but in presence of the intrinsic nonlinearities) are measured. Thus, our experiment is not sensitive to the intrinsic anharmonicities of the trap, but only to those effected by the cubic feedback.

4.2.2 Delayed nonlinearities

Besides nonlinear force perturbations, we will be interested in delayed forces. Artificially produced feedback forces will naturally be subject to electronic delay. Accounting for the effects of such delays in perturbation theory allows us to understand the limits of validity of Eq. (4-7) for modelling the artificial feedback forces. More broadly, understanding the role of delays might also enable the study of perturbative nonlinear non-Markovian stochastic dynamics [32].

We consider the generalized Langevin equation,

$$\ddot{z}(t) = -\gamma_m\dot{z}(t) - \Omega_z^2 z(t) - \frac{G_{fb}}{m}\,z^3(t-\tau) + \sqrt{C}\,\eta(t), \quad (4\text{-}15)$$

where $\tau > 0$ is a fixed (constant) time delay. Note the delayed position can be

written in terms of a memory kernel,

$$z(t-\tau) = \int z(s)K(t-s)\,ds, \tag{4-16}$$

where

$$K(t-s) = \delta(t-\tau-s). \tag{4-17}$$

The perturbation expansion for $\tau = 0$ (Eq. (4-7)) can then be generalized to

$$A(t,\tau) \equiv \mathbb{E}[z(t)z(0)] = \langle z(t)z(0)e^{\frac{C}{2}\int \tilde{z}^2(s)ds} e^{\frac{G_{fb}}{m}\int \tilde{z}(t')z^3(t'-\tau)dt'}\rangle_0. \tag{4-18}$$

Expanding the exponentials in power series and using the Wick sum as defined in (4-6), the leading correction to the auto-correlation function (4-9) is given by the following integrals,

$$\begin{aligned}\Delta A(t,\tau) \propto & \\ &\int G(t-t_1)G(-s_1)G(t_1-s_1-\tau)G^2(t_1-s_2-\tau)dt_1ds_1ds_2 \\ &+\int G(-t_1)G(t-s_1)G(t_1-s_1-\tau)G^2(t_1-s_2-\tau)dt_1ds_1ds_2\ .\end{aligned} \tag{4-19}$$

We note both integrals are multiplied by the constant $3G_{fb}C^2/m$, which we omit to avoid cluttering the notation. Evaluating the integrals leads to the corrected auto-correlation function to first order in the perturbation,

$$\begin{aligned}A(t,\tau) = \frac{Ce^{-\gamma_m|t|/2}(2\Omega'_z\cos\Omega'_z|t| + \gamma_m\sin\Omega'_z|t|)}{\gamma_m\Omega'_z(\gamma_m^2+4\Omega_z'^2)} + \frac{3C^2G_{fb}e^{-\gamma_m|t|/2}}{64m\gamma_m^3\Omega_z'^4\Omega_z^6}\Bigg\{ & \\ e^{\gamma_m\tau/2}[8\gamma_m\Omega_z'^4 - 4\Omega_z^2\gamma_m^2\Omega_z'^2(|t|-\tau)]\cos(\Omega'_z(|t|-\tau)) & \\ + e^{\gamma_m\tau/2}[8\gamma_m\Omega_z'^3\Omega_z^2(|t|-\tau) + 8\Omega_z'^5 + 4\gamma_m^2\Omega_z^2\Omega'_z + 6\gamma_m^2\Omega_z'^3]\sin(\Omega'_z(|t|-\tau)) & \\ + e^{-\gamma_m\tau/2}[\Omega_z'^2(2\gamma_m^2\Omega'_z - 8\Omega_z'^3)\sin(\Omega'_z(|t|+\tau)) & \\ + 8\gamma_m\Omega_z'^4\cos(\Omega'_z(|t|+\tau))]\Bigg\} + \mathcal{O}\Big(G_{fb}^2, C^3\Big),\end{aligned} \tag{4-20}$$

The quantity $A(0,\tau)$ can be experimentally obtained from the area under the PSD of the particle's motion, which in turn can be related to the mean occupation number of the mechanical modes. In what follows, we use these expressions to account for the effects of delay in the artificially generated nonlinear forces, and to show that perturbation theory in the absence of delay provides a good approximation to current experiments.

4.3 Experiment

A simplified schematic of the experimental setup is shown in Fig. 4.1. A CW laser at 780 nm (Toptica DL-Pro) is amplified using a tapered amplifier (Toptica BoosTa) producing up to 1.5 W at the output of a single mode fiber, yielding a high quality Gaussian beam. The beam is expanded to overfill an aspheric lens of numerical aperture NA = 0.77 (LightPath 355330) mounted inside a vacuum chamber, which provides a tightly focused Gaussian beam to form the optical trap. A solution of silica spheres of diameter $2R = 143$ nm (MicroParticles GmbH) is mono-dispersed in ethanol and delivered into the optical trap using a nebulizer. Once a single particle is trapped, the pressure in the chamber is reduced to 10 mbar. The trapped particle's axial center-of-mass (CoM) motion, $z(t)$, is recorded by collecting forward scattered light with an aspheric lens of numerical aperture NA = 0.50, and directing it to a photodiode (Thorlabs PDA100A2), generating an electric signal proportional to $z(t)$.

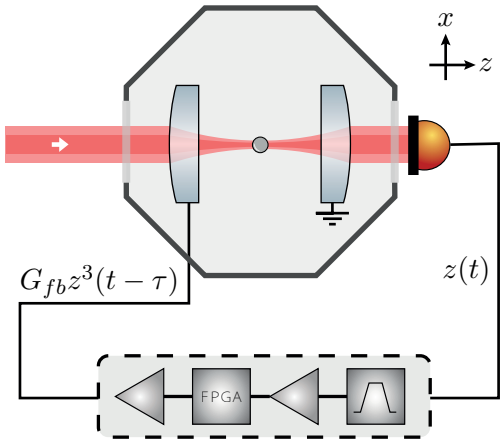

Figure 4.1: Experimental setup. A silica nanoparticle is trapped by an optical tweezer in vacuum. The forward scattered light is collected and sent to a photodiode, producing a signal proportional to the particle's axial coordinate, $z(t)$. An FPGA processes the signal to produce a voltage that induces a force on the trapped particle proportional to $z^3(t-\tau)$. Amplification prior to and after the FPGA enhance the maximum resolution of its analog-to-digital converter, enabling the exploration of a broader range of values for the applied electrical force. The x-direction pictured in the scheme is parallel to the optical table.

The signal from the detector is sent to a wide band-pass filter, amplified and then input into an FPGA. The FPGA introduces a tunable delay, raises the signal to the third power and multiplies it by a tunable gain. The output signal is then amplified once again and applied to the mount of the trapping

lens, producing a voltage difference with respect to the mount of the collection lens, which is grounded. This generates an electric force at the particle position given by $G_{fb}z^3(t-\tau)$, where τ is the total delay introduced by the electronics and G_{fb} is the overall feedback gain. For more details on the generated electric field and electronics, see Subsections 4.5.1 and 4.5.2.

The electronics naturally introduce a delay to the applied position-dependent electric forces, which could lead to deviations from the predictions of the perturbation theory discussed in Subsection 4.2.1. To qualitatively understand the effects of a delayed feedback nonlinear force, we have exaggerated the electronic delay τ applying a cubic force of the form $G_{fb}x^3(t-\tau)$ for $\tau = 2\pi/4\Omega_z$ and $\tau = 6\pi/4\Omega_z$, and subsequently measured the PSDs of the particle motion along the longitudinal direction, these delays are equivalent, respectively, to an additional phase ϕ of $\pi/2$ and $3\pi/2$. The results can be seen in Fig. 4.2a), in comparison to the PSD of the trapped particle in the absence of nonlinear feedback. We see that depending on the delay, the particle undergoes cooling ($\phi = \pi/2$) or heating ($\phi = 3\pi/2$). This can be understood as the nonlinear analogue of cold damping, where the delayed feedback signal acquires a force component proportional to the velocity [15, 36, 37].

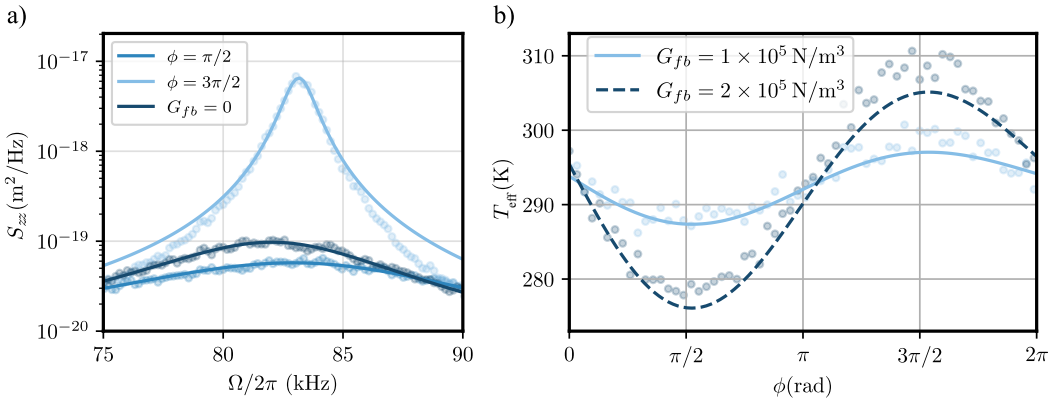

Figure 4.2: Effect of a delayed nonlinearity. a) Longitudinal position PSDs for the reference measurement (—) in comparison to cubic feedback forces at a gain of $G_{fb} = 5.31 \times 10^6\,\mathrm{N/m^3}$ and delays of $\phi = \pi/2$ (—) and $\phi = 3\pi/2$ (—). These comparisons reveal how the introduction of a delayed cubic force can either cool or heat the particle's motion. b) Numerically simulated effective temperature T_{eff} of particle's motion as a function of the delay in the cubic feedback force, displaying cooling and heating in accordance to the predictions of nonlinear delayed perturbation theory described in Subsection 4.2.2. With this analysis, we conclude that the electronic delay present in our experiment, measured to be $\tau = (4.2 \pm 0.6)\%$ of a period, can be safely neglected.

We can quantify the effect of delay for the case of our experiment using the theory described in Subsection 4.2.2. To do that, we have simulated the particle dynamics under the influence of a delayed feedback cubic force for two different values of the feedback gain G_{fb} within the regime of perturbation theory. For each simulation, we extract the particle motion traces and compute the position variance, from which the effective temperature T_{eff} of the mechanical oscillator can be obtained. The results are plotted in Fig. 4.2b) as a function of τ, in comparison to the theoretical prediction given by Eq. (4-20). The simulations confirm the qualitative cooling/heating results shown in Fig. 4.2 and are in good agreement to the perturbation theory with the inclusion of delay. Notably, for the electronic delay in our experiment, characterized to be $\tau = (0.518 \pm 0.074) \times 10^{-6}\,\text{s}$, we verify that the expected cooling/heating effects due to a delayed nonlinear feedback provide a correction to the auto-correlation at the level of 1.10% and are buried within experimental uncertainties. With this analysis we conclude that any effect associated to electronic delay in our experiment is negligible and the perturbation theory in the absence of delay can be used to model the effect of nonlinear perturbations.

We next proceed to verify the perturbation theory as described in Section 4.2.1 (without delay, $\tau = 0$). We apply an effective quartic perturbation to the optical potential by acting on the trapped particle with a cubic force which was generated, as previously described, from the position measurement feedback. PSDs of particle motion under the influence of the cubic feedback force with positive and negative feedback gains can be seen in Fig. 4.3a). These measurements qualitatively confirm the effect of the cubic force predicted by perturbation theory as a shift in the PSD central frequency. Note the shift depends on the sign of the feedback gain, in accordance to Eq. (4-13), indicating an effective hardening or softening of the optical trap due to the cubic actuation.

To quantitatively compare the frequency shifts with the predictions from perturbation theory, we acquired the longitudinal motion PSD for different values of feedback gain G_{fb}. Note that all parameters going into κ (see Eq. (4-13)) are obtained from additional setup characterizations, leaving no free parameters for adjusting the theory to the data. For instance, the trap central frequency Ω_z and mechanical damping γ_m are obtained from Lorentzian fits of the unperturbed PSD, the nanoparticle mass m is calculated from the diameter provided by the manufacturer and from the density of silica, and the applied feedback gain G_{fb} is obtained after the calibration of the detector, electrode and other intermediate electronic elements as described in more detail in Subsection 4.5.2. The particle is taken to be at ambient temperature $T = 293\,\text{K}$; note that a 5 K variation in temperature yields a 2 % variation in theoretical prediction.

Once these characterizations have been performed, the central frequencies of the perturbed PSDs – and consequently the associated shifts – can be obtained by a Lorentzian fit as a function of feedback gain and compared to the theoretical predictions. The result of these measurements is shown in Fig. 4.3b), in comparison to the theoretical prediction given in Eq. (4-13) for our experimental parameters.

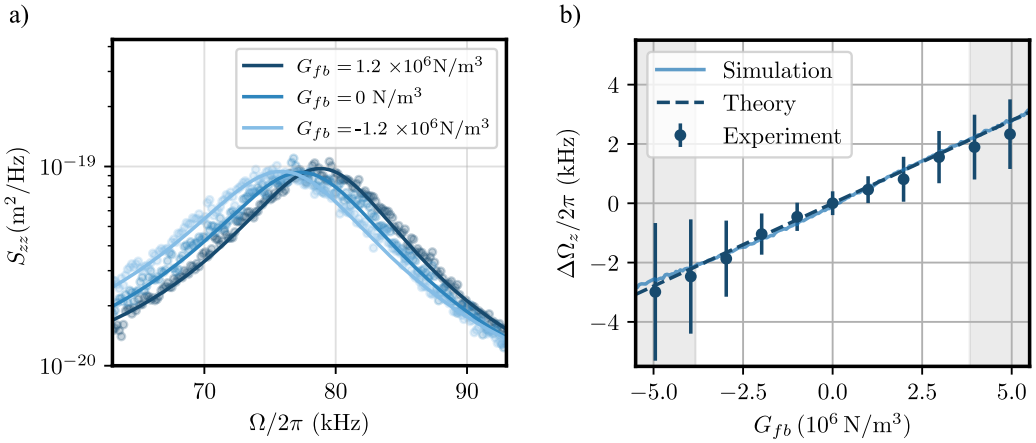

Figure 4.3: Verifying the predictions of perturbation theory. a) PSDs of the trapped particle's longitudinal motion under cubic force, displaying central frequency shifts. The data was taken at 293 K and a pressure of 10 mbar. The reference PSD (—) has a central frequency of 77.8 kHz and a shift of ±1.4 kHz was measured for $G_{fb} = \pm 1.2 \times 10^6\,\mathrm{N/m^3}$. b) Frequency shifts as a function of G_{fb}, verifying the prediction of perturbation theory given by Eq. (4-13) (dashed line). The grey shaded region marks the regime of validity for perturbation theory described in Eq. (4-14). Each point corresponds to 250 seconds of data acquisition at 500 kHz divided into 1000 traces and organized into batches of 5 traces each. All data points were collected using the same nanoparticle.

Good agreement between the data and the theoretical prediction was observed within the perturbation regime, indicated by the non-shaded region of the plot. Note also that outside the regime of perturbation theory (grey shaded regions in Fig. 4.3b), the measured shifts fall systematically slightly bellow the predicted first order correction, consistent with the second-order correction scaling of $\mathcal{O}(G_{fb}^2)$ [30]. Note the error bars in Fig. 4.3b) are larger for negative feedback in comparison to positive feedback gains. We attribute this to the fact that the intrinsic nonlinearity of the optical trap introduces an effective negative feedback gain ($G_{\mathrm{optical}} \approx 10^6\,\mathrm{N/m^3}$), shifting the regime of validity of perturbation to the right, towards positive gains [29]. Finally, the

experimentally obtained angular coefficient κ_e was measured to be

$$\kappa_e = (5.46 \pm 0.10) \times 10^{-4}\,\mathrm{Hz\,m^3\,N^{-1}}, \tag{4-21}$$

which compares to the theoretical prediction given the parameters for our experiment,

$$\kappa_t = 5.69 \times 10^{-4}\,\mathrm{Hz\,m^3\,N^{-1}}\ . \tag{4-22}$$

4.4 Conclusions

In conclusion, we have implemented a cubic nonlinear force based on position measurement feedback acting on an underdamped levitated nanoparticle. Effects of the cubic force on the particle's stochastic dynamics have been experimentally studied. In particular, shifts introduced in the particle motion power spectrum due to the presence of the cubic feedback force have been measured. We have verified that these shifts are in accordance to the predictions of the stochastic path integral perturbation theory for nonlinear optical tweezers introduced in [30]. To account for the experimental imperfections due to electronic delay in the feedback, we have also extended the perturbation theory and showed that for feedback schemes currently available in levitated optomechanics experiments the effects of electronic delay can be made negligible.

We anticipate that nonlinear electric feedback potentials will find a number of applications in levitated optomechanics experiments, both in the classical stochastic and quantum regimes. For instance, delayed nonlinear feedback can be used to engineer a non-conservative system with nonlinear damping of the Van der Pol type [108]. Finally, weak measurements of a levitated optomechanical system in a cavity might allow for feedback-induced nonlinear dynamics in the quantum regime [109] – the non-classical version of feedback-induced nonlinear forces. In combination with recent advances in levitated quantum control experiments [14,15], weak nonlinear feedback could then enable the preparation of non-Gaussian states beyond the nonlinearities naturally present in optical potentials [27,96].

4.5 Supplementary material

4.5.1 Electric field simulation

One of the experiment's central assumptions is that the electric force acting upon the trapped particle is proportional to the voltage applied to the electrodes and does not depend on its position. Moreover, due to symmetry around the optical axis, we expect the components of the electric force orthogonal to the optical axis to be negligible. To verify these assumptions, a simulation of the electric potential and electric field generated by the geometry of the optical setup was conducted using COMSOL Multiphysics software (version 5.4).

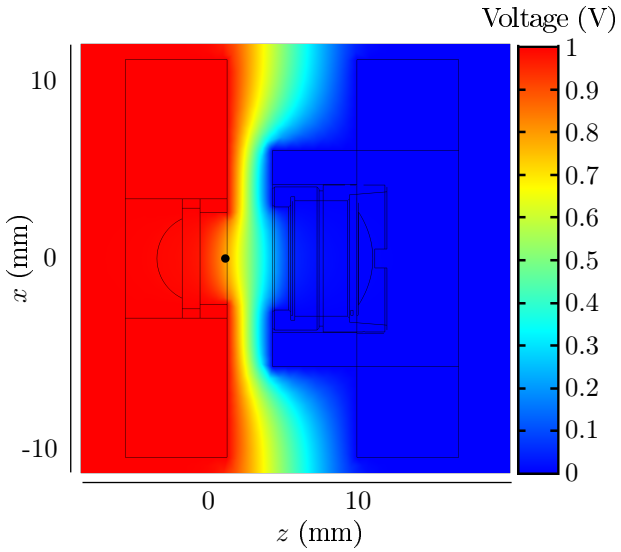

Figure 4.4: Electric potential generated by the electrode's geometry for a slice in the xz plane passing through the optical axis. The contour shows the internal structure of the optical setup with the black dot marking the average position of the trapped particle, about 1.59 mm away from the flat base of the trapping lens.

In Fig. 4.4, the electrical potential between the electrodes is shown for a slice in the xz plane, where the internal contour of the optical setup is displayed for clarity. The left electrode, which contains the trapping lens, is set at 1 V relative to the right one, which holds the collection lens. The black dot denotes the average position of the trapped particle, 1.59 mm away from the flat base of the aspheric lens. Figures 4.5a) and 4.5b) show the electric field components in the vicinity of the particle. Considering an average amplitude of 100 nm for the CoM motion, the simulation shows a percent change of roughly 0.01% for the z component of the electric field. Moreover, the x and y components are

four to five orders of magnitude smaller than the z component, thus providing a firm foundation for our assumptions.

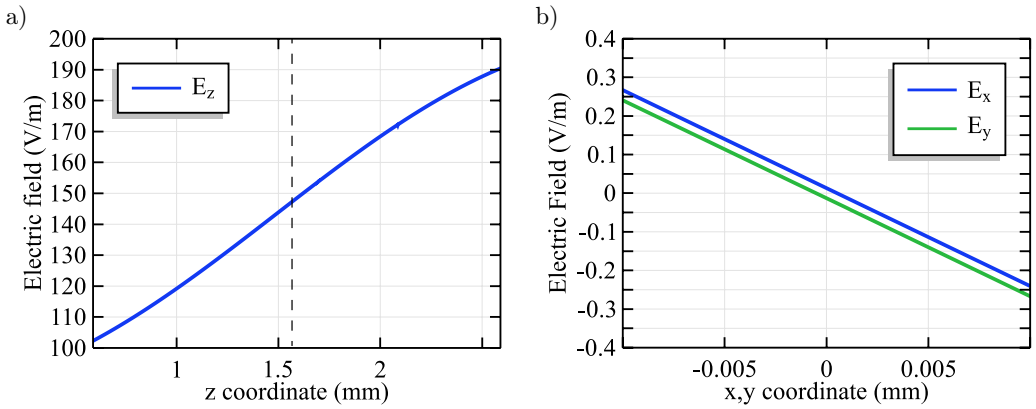

Figure 4.5: a)-b) The z and x, y components of the electric field in the vicinity of the trapped particle. The dashed line denotes the average position of the particle.

4.5.2 Electronics

In order to apply the feedback signal, essential steps were undertaken regarding the implementation of an electronic setup aimed at preprocessing the detection signal. First, it was crucial to address a strong DC component present in the signal obtained from the photodetector. To prevent saturation of the Red Pitaya RF input used in the experiment, an analog band-pass filter was implemented for its capability to remove both DC and high-frequency components effectively. While it is common to opt for a Butterworth filter based on the Sallen-Key topology [110], it is important to highlight that this choice introduces an undesirable phase effect.

As demonstrated by simulation results showed in Fig. 4.6a), the addition of a Butterworth filter results in a shift of the PSD central frequency, which deviates from the theoretical prediction presented in [30]. To overcome this problem a passive RC filter is used along with a non-inverter amplifier. As evident from Fig. 4.6b), the comparison of the Bode diagrams for both topologies illustrates that the passive filter will have minimal impact on the signal phase, while simultaneously maintaining a flat band over a wider frequency range.

The addition of a non-inverting amplifier after the band-pass filter enables the utilization of the full resolution of the ADC on the Red Pitaya board. Furthermore, a second amplifier is incorporated after the FPGA, facilitating the generation of voltage values approximately ten times higher than the board's limit. Upon characterization of both amplifiers, we found that the gains, A_1 and

A_2, before and after the FPGA were measured as 11.00 V/V and 11.27 V/V, respectively. These values will be necessary for the calibration of the overall feedback gain G_{fb}, detailed in Subsection 4.5.3.

In Fig. 4.6c) we illustrate an example of input and output signals of the Red Pitaya. In order to implement the non-linear function, we employed fixed-point arithmetic—a method for representing fractional numbers within a specified range. This approach enables us to execute complex mathematical operations without suffering from information loss [111], as is often the case with binary representation. Furthermore, it offers straightforward means of extending the code to implement higher-order polynomial functions.

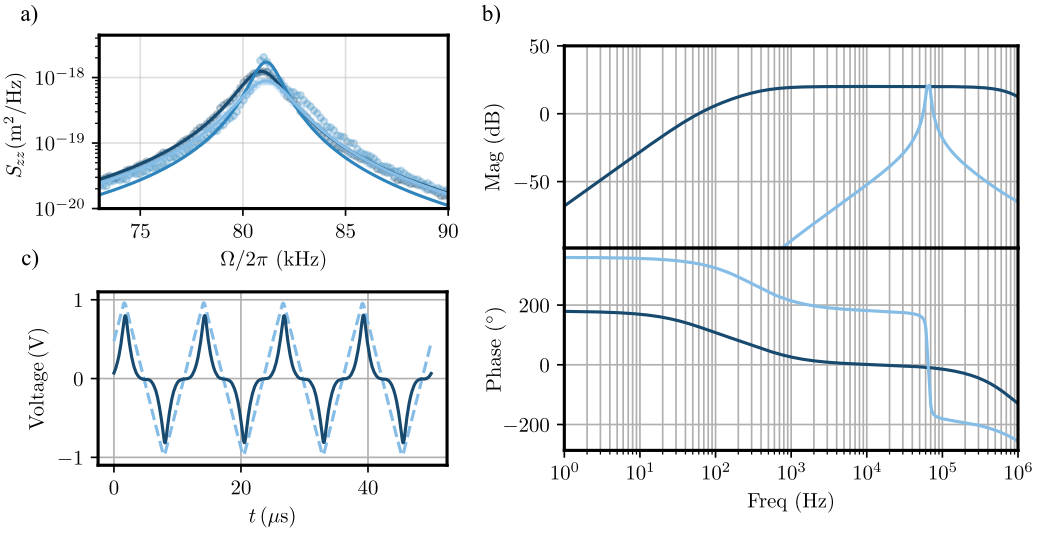

Figure 4.6: Electronics design. a) PSDs obtained from simulations of a tweezed nanoparticle ($\Omega_z/2\pi = 81.5\,\text{kHz}$ and $\gamma_m = 1.3 \times 10^4\,\text{s}^{-1}$) under the influence of a cubic force. Three scenarios were considered: second-order Butterworth filter with 1 kHz bandwidth (—), 10 kHz bandwidth (—) and, lastly, with no filter (—).b) Bode diagrams of a highly selective Butterworth filter (—) and of a passive RC filter (—), both circuits were simulated using LTspice XVII. c) Results from the FPGA program. The dashed line represents the input, which is a triangular wave with a frequency of 81 kHz. The solid line corresponds to the output, which is proportional to the input raised to the third power.

4.5.3 Calibration of applied force

To validate the theoretical predictions outlined in [30], it was necessary to calibrate the overall feedback gain G_{fb}, defined as

$$G_{fb} = C_{NV} A_2 A_d A_1^3 C_{Vm}^3, \tag{4-23}$$

where A_1 and A_2 represent the gains originating from the electronic amplifiers, A_d is the tunable digital gain defined within the FPGA, C_{Vm} is the calibration factor which converts the measured voltage into corresponding displacement in meters and C_{NV} is the transduction coefficient that establishes the connection between applied voltage across the electrodes and the resulting force applied to the particle; see Subsection 4.5.2 for further details.

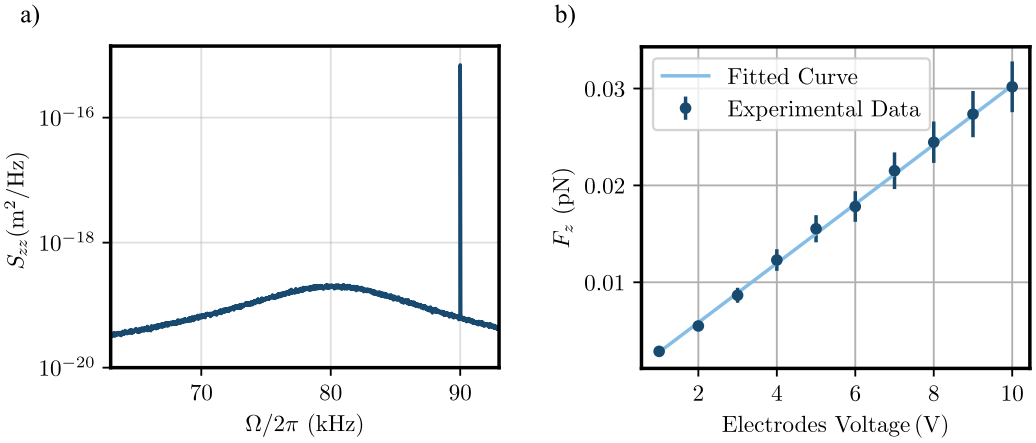

Figure 4.7: Electrode calibration. (a) PSD obtained from a trapped nanoparticle at 10 mbar and $T = 293\,\mathrm{K}$ under the action of a sinusoidal drive (voltage amplitude $V_0 = 10\,\mathrm{V}$ and frequency $\Omega_{dr}/2\pi = 90\,\mathrm{kHz}$). b) Calibration curve for electrodes used to map the applied voltage to the resulting force applied on the nanoparticle.

To calibrate the photodetector, 1000 traces of 0.1 seconds were collected. The PSD of the time traces is fitted by a Lorentizan distribution,

$$S_{VV}(\Omega) = \frac{D}{\gamma_m^2\Omega^2 + (\Omega^2 - \Omega_z^2)^2}, \tag{4-24}$$

where $D = 2\gamma_m k_B T C_{Vm}^2/m$; this take in consideration that $S_{VV}(\Omega) = C_{Vm}^2 S_{zz}(\Omega)$ [92]. This procedure led to a calibration factor of $C_{Vm} = (1.504 \pm 0.073) \times 10^4\,\mathrm{V/m}$. After calibration of the detector, we proceed to determine the transduction coefficient, denoted as C_{NV}. To obtain C_{NV}, we subjected the particle to a series of sinusoidal signals with varying amplitudes and measured the particle's response in the position PSD [24]. For a particle subjected to Eq. (4-3), the total PSD $S_{zz}^T(\Omega)$ in the presence of an electric drive $F_{el}(t) = F_0\cos(\Omega_{dr}t)$ can be expressed as [24],

$$S_{zz}^T(\Omega) = S_{zz}(\Omega) + S_{zz}^{el}(\Omega) = \frac{2\gamma_m k_B T}{m[(\Omega^2 - \Omega_z^2)^2 + \gamma_m^2\Omega^2]} + \frac{F_0^2\tau_{el}\,\mathrm{sinc}^2[(\Omega - \Omega_{dr})\tau_{el}]}{m^2[(\Omega^2 - \Omega_z^2)^2 + \gamma_m^2\Omega^2]}, \tag{4-25}$$

with τ_{el} being the duration of the measure. In Fig. 4.7a), we display one of the PSDs used for the electrode calibration. The resulting calibration curve is presented in Fig. 4.7b), which yields a transduction coefficient $C_{NV} = (3.06 \pm 0.13) \times 10^{-15}\,\mathrm{N/V}$. All measurements described in the main text were performed with the same nanoparticle.

5
All electrical cooling of an optically levitated nanoparticle

Optically trapped nanoparticles are a promising platform for investigating quantum mechanics in the mesoscopic regime [26, 27, 112]. However, to explore their quantum properties effectively, particles motion must be decoupled entirely from the thermal environment. This necessitates precise control over their motion, high detection efficiency, and an ultra-high vacuum environment. Typically, parametric cooling is utilized to pre-cool the particle's motion in three dimensions [14, 15, 34, 36, 37, 51]. However, this approach introduces additional experimental requirements, such as the need for electro or acoustic-optic devices for laser beam modulation and electronic equipment for phase locking. In this chapter, we explore the use of an all-electrical control approach, wherein a set of electrodes is employed to apply a three-dimensional linear control law aimed at reducing the energy of the trapped nanoparticle. This dissertation was finished a few days before the findings reported in this chapter were published in a pre-print [113], and the content of this chapter closely mirrors that of the article. Similar to Chapter 4, the supplementary material from the publication has been integrated, resulting in Section 5.6.

5.1 Introduction

Optical tweezers [19] have emerged as a valuable tool for isolating and controlling the motion of micro- and nano-objects [4, 56, 85]. By clever combinations with electric and magnetic traps and actuators [114–118], optical traps can be used to design highly sensitive sensors for force, acceleration, and torque [22, 24, 119–121], with a high degree of control enabling cooling of the center-of-mass motion of a levitated nanoparticle to the ground state [13–15, 122]. Moreover, tweezers provide a versatile platform for many-body [123–127] and fundamental physics experiments, with applications in diverse areas such as stochastic thermodynamics [31, 86, 128–130], nonlinear dynamics [29, 31, 84, 99, 131], the search for new particles and forces of nature [132–137], and unprecedented tests of quantum mechanics [138–142]. All these applications require the levitated object to be well isolated from its surrounding environment, which is mainly limited by the vacuum quality of the experiment, photon recoil

heating [51], and black body radiation [143]. Regarding the vacuum quality, since the nano-object is initially trapped at atmospheric pressure, it is thermalized at room temperature, preventing stable trapping at low pressures and rendering the trapping potential nonlinear due to large thermal fluctuations [29]. Therefore, cooling the object's motion is often a prerequisite for levitation experiments.

Active feedback cooling [36, 37], in particular parametric cooling, has emerged as the standard technique for achieving 3D cooling of the levitated nanoparticle's motion [34], enabling temperatures as low as sub-mK [51]. In practice, parametric control techniques are often used as a precooling mechanism. The performance of parametric feedback, however, comes at the cost of employing a nonlinear control protocol which modulates a portion of the optical trapping power according to the resonance frequencies of the nanoparticle. In addition, expensive electro- (EOM) or acousto-optic (AOM) modulators must be used in combination with lock-in devices capable of modulating a signal locked to the particle's motion. Alongside the parametric control, once the thermal occupation number has been reduced to around 10^3, the levitated object's charge can be exploited to further control its motion along one direction to even lower temperatures all the way into the quantum ground state [14, 15].

In this letter we explore an all electrical approach to pre-cool the motion of a levitated nanoparticle from room temperature to a point where the trap's nonlinear features are significantly reduced and stable trapping can be achieved in high-vacuum ($p < 10^{-3}$ mbar). To do so, we design a simple electric actuator based on a custom made printed circuit board (PCB), capable of influencing the particle's motion via Coulomb forces. Fine alignment of the PCB with the levitated nanoparticle is not required. After a careful calibration of the electrical forces, we employ a delayed feedback scheme to 3D cool the CoM motion of the particle. We experimentally measure the effect of the delay in the feedback force and show excellent agreement with theoretical predictions [144]. Finally, we successfully demonstrate 3D cooling down to sub-Kelvin temperatures while completely avoiding modulation of the trap's power, in a first step towards the larger effort of simplifying optomechanical cooling experiments. With numerical simulations based on our electrical actuator we argue that, in combination with a stiffer optical trap, quantum-limited detection for all three axes [145] and optimal quantum state estimation [38, 146, 147], all electrical 3D ground state cooling can be achieved in our setup.

We highlight that 3D electrical feedback cooling of levitated nanoparticles has been recently implemented in levitated optomechanics experiments – see [148–150] for examples using integrated chip photonics, hybrid optical Paul trap and finely aligned electrode tips. Our setup adds a simplified solution

to that list, while still offering the possibility of 3D quantum control of a levitated nanoparticle. This paper is organized as follows. In Section 5.2 we briefly describe the equations of motion and the LQR, used to evaluate the optimal proportional and derivative gains used in the control feedback. Next, Section 5.3 describes the experimental setup, while 5.4 shows the results on all electrical feedback cooling and the prospects for 3D ground state cooling. We conclude in Section 5.5 with a brief discussion.

5.2 Theory

The CoM motion along the x, y and z-axes of an optically levitated nanoparticle trapped by a strongly focused Gaussian beam can be effectively modeled through a set of second-order Langevin equations,

$$\ddot{x}(t) + \gamma_m \dot{x}(t) + \Omega_x^2 x(t) = \frac{1}{m} F_{\mathrm{th},x}(t) + b_x u_x, \tag{5-1a}$$

$$\ddot{y}(t) + \gamma_m \dot{y}(t) + \Omega_y^2 y(t) = \frac{1}{m} F_{\mathrm{th},y}(t) + b_y u_y, \tag{5-1b}$$

$$\ddot{z}(t) + \gamma_m \dot{z}(t) + \Omega_z^2 z(t) = \frac{1}{m} F_{\mathrm{th},z}(t) + b_z u_z, \tag{5-1c}$$

where m is the particle's mass, γ_m the drag coefficient, Ω_i the angular frequency along the i-axis and $F_{\mathrm{th},i}$ represents the (white-noise) stochastic force on each axis due to residual gas pressure in the vacuum chamber, satisfying

$$\langle F_{\mathrm{th},i}(t) \rangle = 0, \tag{5-2a}$$

$$\langle F_{\mathrm{th},i}(t) F_{\mathrm{th},j}(t+\tau) \rangle = 2m\gamma_m k_B T \delta_{ij} \delta(\tau), \tag{5-2b}$$

where k_B is the Boltzmann constant, T the residual gas temperature, δ_{ij} is the Kronecker delta and $i, j \in \{x, y, z\}$. The $b_i u_i$ terms in Eqs. (5-1) account for external forces that may influence the particle's motion, with u_i representing the control signals defining feedback forces acting on the trapped particle.

By defining the state vector

$$\mathbf{x}(t) \equiv \begin{bmatrix} x(t) & y(t) & z(t) & \dot{x}(t) & \dot{y}(t) & \dot{z}(t) \end{bmatrix}^T, \tag{5-3}$$

one can then write Eqs. (5-1) in the state-variable representation [66], resulting in the MIMO system

$$\dot{\mathbf{x}}(t) = \mathbf{A}\mathbf{x}(t) + \mathbf{B}\mathbf{u}(t) + \mathbf{w}(t), \tag{5-4}$$

where

$$\mathbf{A} = \begin{bmatrix} \mathbf{0}_{3\times 3} & \mathbf{I}_3 \\ -\mathrm{diag}(\mathbf{\Omega}^2) & -\gamma_m \mathbf{I}_3 \end{bmatrix}, \ \mathbf{w}(t) = \frac{1}{m} \begin{bmatrix} \mathbf{0}_{3\times 1} \\ \mathbf{F}_{\mathrm{th}}(t) \end{bmatrix}, \tag{5-5}$$

and

$$\mathbf{B} = \begin{bmatrix} \mathbf{0}_{3\times3} \\ \mathrm{diag}(b_x, b_y, b_z) \end{bmatrix}, \ \mathbf{u} = \begin{bmatrix} u_x \\ u_y \\ u_z \end{bmatrix}, \tag{5-6}$$

with $\mathbf{\Omega}^2 = \begin{bmatrix} \Omega_x^2 & \Omega_y^2 & \Omega_z^2 \end{bmatrix}^T$ and $\mathbf{F}_{\mathrm{th}}(t) = \begin{bmatrix} F_{\mathrm{th,x}}(t) & F_{\mathrm{th,y}}(t) & F_{\mathrm{th,z}}(t) \end{bmatrix}^T$. Note that due to the geometry of the feedback actuators in our experiment, the submatrix in $\mathbf{B}$ is not block diagonal, but assumes a more complicated form; see Section 5.3 for more details.

Optimal control theory provides tools to find a control policy $\mathbf{u}(t)$ capable of minimizing the energy of a physical system. For linear systems, such as the one described by Eq. (5-4), this is achieved by the LQR, a controller where the optimization task targets the minimization of a quadratic cost criterion J of the form

$$J = \frac{1}{2}\int_0^\infty [\mathbf{x}^T(t)\mathbf{Q}\mathbf{x}(t) + \mathbf{u}^T(t)\mathbf{R}\mathbf{u}(t)]\, dt, \tag{5-7}$$

where $\mathbf{Q}$ is the weighting matrix and $\mathbf{R}$ is the control effort matrix. The optimal control policy which minimizes Eq.(5-7) is [69]

$$\mathbf{u} = -\mathbf{K}\mathbf{x}, \tag{5-8}$$

where $\mathbf{K} = \mathbf{R}^{-1}\mathbf{B}\mathbf{S}$ is the controller's gain matrix and $\mathbf{S}$ is the solution of the algebraic Riccati equation

$$\mathbf{S}\mathbf{A} + \mathbf{A}^T\mathbf{S} + \mathbf{Q} - \mathbf{S}\mathbf{B}\mathbf{R}^{-1}\mathbf{B}^T\mathbf{S} = \mathbf{0}. \tag{5-9}$$

Practical application of the LQR poses the significant challenge of obtaining the complete state vector $\mathbf{x}$. Experimentally, access is not granted to $\mathbf{x}$ but rather to a measurement vector $\mathbf{y}$, which is related to the states according to

$$\mathbf{y}(t) = \mathbf{C}\mathbf{x}(t) + \mathbf{m}(t), \tag{5-10}$$

where $\mathbf{C}$ is known as the output matrix. The term $\mathbf{m}$ is the measurement noise vector and can be expressed as $\mathbf{m} = \begin{bmatrix} \zeta_x(t) & \zeta_y(t) & \zeta_z(t) \end{bmatrix}^T$. Here $\zeta_i(t)$ are zero-mean white-noise processes with variance σ_i^2, satisfying

$$\langle \zeta_i(t) \rangle = 0, \tag{5-11a}$$

$$\langle \zeta_i(t)\zeta_j(t+\tau) \rangle = \sigma_i^2 \delta_{ij} \delta(\tau). \tag{5-11b}$$

On the one hand, measurements of $x(t)$, $y(t)$ and $z(t)$ can be implemented by collecting forward or backward-scattered light from the nanoparticle [145]. On the other hand, the velocities are not accessible experimentally. An optimal estimation $\hat{\mathbf{x}}$ can be computed by applying real-time filtering techniques to estimate $\mathbf{x}$. For linear dynamics where the disturbances and measurement noises adhere to Eq. (5-2) and (5-11), $\mathbf{x}$ is best estimated using the Kalman filter

[61, 76].

Implementing the Kalman filter significantly increases the complexity of the feedback loop. As a simplification, it is possible to estimate the velocity as being proportional to a delayed position measurement. This approach has proven successful for cooling one of the spatial degrees of freedom of the levitated nanoparticle [37], albeit increasing the minimal effective temperature achievable. The effective temperature for each axis can be computed by using the integral [15]

$$T_{\text{eff}}^{i} = \frac{m\Omega_i^2}{k_B}\int_0^\infty \left(1+\frac{\Omega^2}{\Omega_i^2}\right) S_{ii}(\Omega)\, d\Omega - \frac{1}{2}, \tag{5-12}$$

where S_{ii} is the double-sided PSD for the particle's motion along the i-axis, expressed as

$$S_{ii} = \frac{2\gamma_m k_B T}{m[(\Omega^2-\Omega_i^2)^2+\gamma_m^2\Omega_i^2]}. \tag{5-13}$$

5.3 Experiment

The experimental setup is schematically illustrated in Fig. 5.1a). A CW laser at 1550 nm (RIO Orion) amplified by an Erbium-doped fiber amplifier (Keopsys CEFA-C-BO-HP-SM) is used to produce a high-quality Gaussian beam linearly polarized along the x direction with a power of $P_t \approx 2\,\text{W}$, at the output of a single-mode fiber. The beam is focused by an aspheric lens (Thorlabs C330TM-C, NA = 0.68) assembled inside a vacuum chamber, allowing for stable optical trapping. The light scattered by the particle along the forward direction is collimated by a collecting lens (Thorlabs C110TM-C, NA = 0.40). Silica nanoparticles (diameter 143 nm, MicroParticles GmbH) are loaded into the vacuum chamber by a nebulizer and trapped at atmospheric pressure. The trapped particle oscillates with resonance frequencies along the three axes given by $\Omega_x/2\pi = 96.24\,\text{kHz}$, $\Omega_y/2\pi = 101.49\,\text{kHz}$ and $\Omega_z/2\pi = 31.52\,\text{kHz}$.

Detection of transversal motion, $x(t)$ and $y(t)$, is carried out using balanced photodiodes (Newport 2117-FC), while information about the longitudinal $z(t)$ direction is obtained by direct intensity photodetection. The optical trap is characterized through measurements of the particle's PSDs for each direction. Information on the occupation numbers and effective temperatures of each direction can also be obtained from the PSDs by using Eq. (5-12).

A PCB containing two orthogonal pairs of electrodes, illustrated in Fig. 5.1b), is placed in the vicinity of the optical trap's focus, allowing for two-dimensional electrical feedback control of the nanoparticle's CoM motion. The PCB is designed to be compatible with cage plate optical systems (Thorlabs

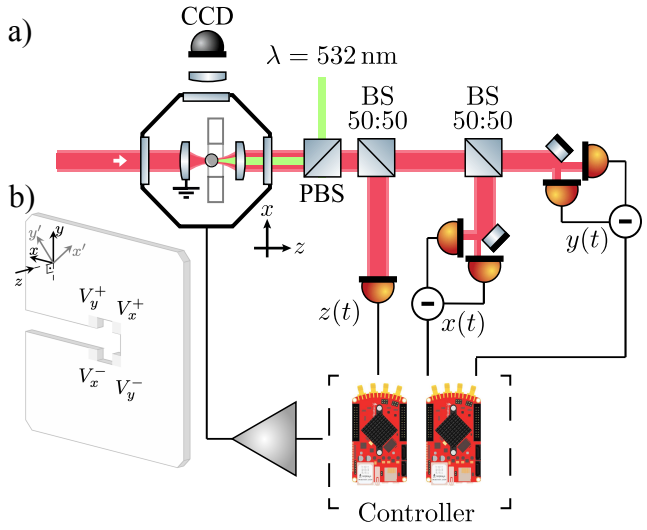

Figure 5.1: Experimental setup. a) Simplified scheme of the setup. An optical tweezer is assembled within a vacuum chamber, and a CCD is used for imaging of the tweezed particle upon illumination with a 532 nm laser beam. The trapping lens is grounded, and detection of forward-scattered light is used to generate the electrical feedback signal sent to the electrodes. The collection lens works as the z-electrode, whilst the board shown in b) is placed close to the trap's focus and contains the x- and y-electrodes. The axes at the top left indicate the orientation between the electrodes' axes (x', y') and the coordinate system of the detection.

SP02). Note also that only coarse alignment of the PCB with respect to the levitated nanoparticle is required, and this can be achieved by placing the PCB near the optical focus. Due to the employed control method, coupling between degrees of freedom in the transverse plane is compensated by the calibration process.

A third pair of electrodes is implemented by applying an electric signal to the mount of the collection lens, producing a voltage difference with respect to the grounded trapping lens. The signal from the detection is digitally processed by two FPGAs (STEMlab 125-14, Red Pitaya) and analogically amplified before being fed back to the electrodes. We remove any cross-talk between z and xy electrodes by digital filtering, which is facilitated by the difference in characteristic frequencies between the longitudinal and transversal degrees of freedom. Taking this and the geometry of the actuators into consideration, the gain matrix assumes a block diagonal form,

$$\mathbf{K} = \begin{bmatrix} \mathbf{K}_{p,xy} & 0 & \mathbf{K}_{d,xy} & 0 \\ \mathbf{0}_{1\times 2} & k_{p,z} & \mathbf{0}_{1\times 2} & k_{d,z} \end{bmatrix} \tag{5-14}$$

A detailed description of the analogical amplification and the digital processing of the detection signal can be found in Subsection 5.6.2. Digital processing includes frequency filtering, delaying and application of derivative/proportional gains to the signal. The choice of optimal gains was based on control theory, as presented in Subsection 5.6.1. Since the theory predicts only a weak dependence of optimal gain on pressure, we consider a single gain to be optimal throughout the experiment.

Appropriate calibration of the electrodes accounts for misalignment between the electrodes' axes and the mechanical modes, allowing for a partial reconstruction of the **B** matrix, which assumes a 45° rotated form with respect to the diagonal matrix given by Eqs. (5-1). During calibration, the effect of the z-electrode was observed to be too weak, such that only the x- and y-electrodes could be calibrated. This has led to applying the control LQR only to the x and y motion and a cold damping protocol [15, 36] along the z direction ($k_{p,z} = 0$). We refer to Subsection 5.6.3 for more information on the calibration procedure.

5.4 Results

Proper implementation of the control method as previously described requires precisely delaying each detection signal. The delay characterization process involves applying a force proportional to the delayed position independently in the x and y directions. For instance, referring to Eq. (5-1), this translates to $u_x = G_x x(t - \tau_x)$ for the x coordinate (and similarly for y and z). Each delay τ_i consists of two components, the intrinsic electronic delay $\tau_{e,i}$, and an adjustable delay $\tau_{c,i}$. Fig. 5.2 shows measures of T^x_{eff} and T^y_{eff} while subjecting the particle to the delayed force. The controllable delay $\tau_{c,i}$ was varied to span the range of τ_i from $\tau_{e,i}$ to one period of oscillation ($\phi = 2\pi$). The experimental results show excellent agreement with the theoretical predictions from [144]. Furthermore, this measurement allowed for the characterization of the electronic delays, $\tau_{e,x}$ and $\tau_{e,y}$, both of which were determined to be $0.639\,\mu$s. We assume $\tau_{e,z}$ has the same value.

Figure 5.3a) shows the results of 3D feedback cooling. The minimal effective temperatures achieved in the experiment are $T^x_{\text{eff}} = (0.58 \pm 0.12)\,\text{K}$, $T^y_{\text{eff}} = (0.55 \pm 0.11)\,\text{K}$ and $T^z_{\text{eff}} = (3.63 \pm 0.77)\,\text{K}$, for each of the three axes. The gray shaded area in Fig. 5.3a) depicts an instability region observed near $10^{-2}\,\text{mbar}$, characterized by a sudden increase in T^i_{eff}. We attribute this phenomenon to variations on the net charge of the nanoparticle [151]. The net charge acts as a linear parameter affecting the input matrix, thus linearly impacting the control gain. As electrode calibration was performed at

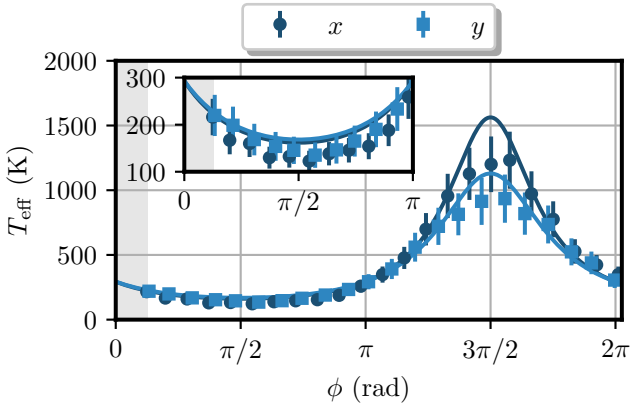

Figure 5.2: Effect of delayed feedback forces. Comparison between experimental results and theory (solid lines) is presented. Measurements were conducted at room temperature (293 K) and a pressure of 1.2 mbar. Each data point corresponds to 10,000 50 ms-traces. The used gains were $G_x = (9.17 \pm 0.98) \times 10^{-9}$ N/m and $G_y = (8.97 \pm 0.97) \times 10^{-9}$ N/m. The gray shaded area marks the region that could not be measured due to the minimal delay imposed by the electronics. The horizontal axis, ϕ, represents the phase $\Omega_i \tau_i$ introduced by the delay. In the inset, the interval where the delay induces cooling is presented with more detail.

high pressure (> 1 mbar), for pressures smaller than 0.01 mbar, it cannot be assumed that the applied gain was optimal. Nonetheless, stable cooling has been implemented by using only electrical actuators and the application of LQR returned a gain matrix capable of handling any coupling between DOFs in the dynamics. The PSD of the CoM motion for the y direction under three distinct pressures is shown in Fig. 5.3b). Feedback cooling not only reduces the area of the PSD, from which the effective temperatures are estimated, but also introduces a term which increases its linewidth, as expected due to the presence of derivative terms in the nanoparticle's motion.

For pressures smaller than 0.01 mbar, no instability has been encountered. As previously established, when the net charge is controlled, its values have been shown to be conserved as pressure reduces below [152]. Therefore, the control protocol employed should be capable of successfully controlling the nanoparticle until the stochastic thermal force becomes negligible and the dynamics starts to be dominated by measurement back-action and photon recoil heating. When compared to parametric cooling, an all electrical approach is advantageous since it avoids contamination of the signal by spurious modulation signals, which are rendered unnecessary. Additionally, in contrast to parametric cooling, the LQR employs a linear control law, thus not affecting the overall linearity of

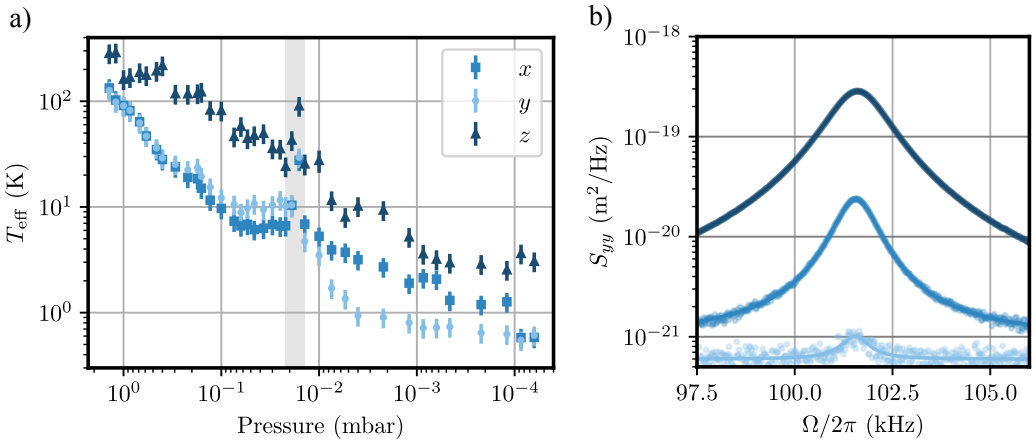

Figure 5.3: All electrical cooling. a) Dependence between pressure and x, y and z effective temperatures. The grey shaded region shows a region of instability, as discussed in the main text. b) PSD of the y motion. Measures were made at 1.0 mbar(—), 5.4×10^{-2} mbar (—) and 1.2×10^{-4} mbar (—).

the system.

Since the LQR has been successfully employed in conjunction with Kalman filter for ground-state cooling along the longitudinal axis [14], extending its application as a 3D quantum control policy should be experimentally achievable. By considering the electrode parameters presented in Subsection 5.6.3 and the trapping and detection efficiency parameters reported in [14], we numerically simulated 3D all electrical cooling of a trapped nanoparticle. Figure 5.4 presents the expected final mean occupation numbers with our all electrical controller. To account for quantum effects, the same parameters of measurement uncertainty, detection efficiency η_z and back-action provided in [14] were taken into account in the simulation. The detection efficiency along the transversal axes, η_x and η_y, were computed given the expected proportion between the efficiency along these axes and the longitudinal one for the given NA [145]. The simulation results for pressures on the order of 10^{-10} mbar agree with the experimental findings in [14], while for higher pressures the simulation may seen optimistic. It must be noted that experimental imperfections were not considered. Moreover, while it is evident that in simulation the thermal occupancy for y exceed that of x, the experimental results in Fig. 5.3a) shows the opposite. This most likely arises from experimental imperfections in the x-axis detection.

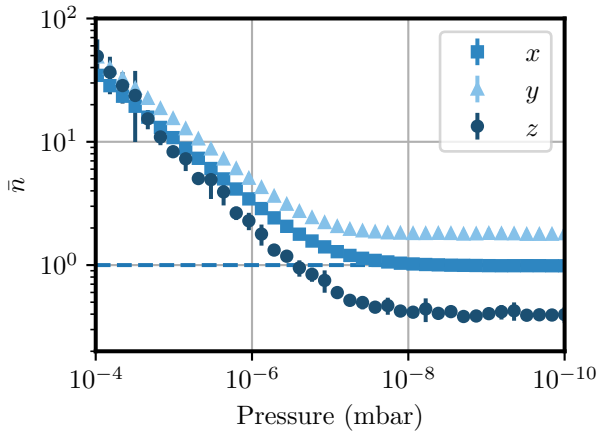

Figure 5.4: Simulation of optimal all electrical 3D cooling with improved trapping lens and detection scheme: expected thermal occupation numbers, $\bar{n}$, as a function of pressure for the x, y and z directions. Dashed line marks a single phonon. Error bars correspond to one standard deviation over 30 simulation runs.

5.5 Conclusions

In conclusion, we have demonstrated an all electrical feedback cooling scheme for reducing the CoM temperature of a levitated nanoparticle in high vacuum. Through a simple custom-designed electrical actuator, we have shown sub-Kelvin temperatures for the transverse directions of motion, avoiding the use of nonlinear feedback cooling schemes such as parametric feedback cooling. This greatly simplifies levitated optomechanics experiments by avoiding the need for modulation of the trapping power. Numerical simulations point that future improvements over our setup, in particular implementation of a higher NA trapping lens and of the optimal backward detection scheme reported in [14], should enable all electrical 3D cooling near the ground state, reaching thermal occupation numbers below unity.

5.6 Supplementary material

5.6.1 Digital control theory

In the study and analysis of physical systems, time is conventionally treated as a continuous variable. However, when employing signal processing and control methods, a transition to a discrete representation becomes necessary. This is specially crucial when implementing systems on microprocessors or

FPGAs, where a set of instructions is executed based on a sampling frequency f_s [72]. The discrete-time formulation of a state-space model can be obtained through the integral approximation, which is based on the assumption that $\mathbf{x}$ and $\mathbf{u}$ remain constant during a sampling period $T_s = 1/f_s$. The system evolution is then considered to unfold at fixed time-steps $t_n = nT_s$, leading to the following recursive equations

$$\mathbf{x}_{n+1} = \mathbf{A}_d\mathbf{x}_n + \mathbf{B}_d\mathbf{u}_n + \bar{\mathbf{w}}_n, \tag{5-15a}$$

$$\mathbf{y}_{n+1} = \mathbf{C}_d\mathbf{x}_{n+1} + \bar{\mathbf{m}}_{n+1}, \tag{5-15b}$$

where $\mathbf{A}_d$, $\mathbf{B}_d$ and $\mathbf{C}_d$ can be expressed in terms of their continuous analogues,

$$\mathbf{A}_d = \sum_{k=0}^{\infty} \frac{T_s^k}{k!}\mathbf{A}^k, \tag{5-16a}$$

$$\mathbf{B}_d = (\mathbf{A}_d - \mathbf{I})\mathbf{A}^{-1}\mathbf{B}, \tag{5-16b}$$

$$\mathbf{C}_d = \mathbf{C}. \tag{5-16c}$$

Also, $\mathbf{x}_n = \mathbf{x}(nT_s)$ and $\mathbf{u}_n = \mathbf{u}(nT_s)$. The discrete disturbance and noise terms, $\bar{\mathbf{w}}_n$ and $\bar{\mathbf{m}}_n$, represent discrete-time white-noise processes adhering to conditions akin to those established in Eqs. (5-2) and (5-11) in the main text. Considering $\bar{\mathbf{w}}_n = \frac{1}{m}\begin{bmatrix}\mathbf{0}_{3\times1} & \bar{\mathbf{F}}_{\mathrm{th,n}}\end{bmatrix}^T$, with $\bar{\mathbf{F}}_{\mathrm{th,n}} = \begin{bmatrix}\bar{F}_{\mathrm{th,x,n}} & \bar{F}_{\mathrm{th,y,n}} & \bar{F}_{\mathrm{th,z,n}}\end{bmatrix}^T$ and $\bar{\mathbf{m}}_n = \begin{bmatrix}\bar{\zeta}_{x,n} & \bar{\zeta}_{y,n} & \bar{\zeta}_{z,n}\end{bmatrix}^T$, the conditions are

$$\langle \bar{F}_{\mathrm{th,i,k}} \rangle = 0, \tag{5-17a}$$

$$\langle \bar{F}_{\mathrm{th,i,k}} F_{\mathrm{th,j,k'}} \rangle = 2m\gamma_m k_B T T_s \delta_{ij}\delta_{kk'}, \tag{5-17b}$$

and

$$\langle \bar{\zeta}_{i,k}(t) \rangle = 0, \tag{5-18a}$$

$$\langle \bar{\zeta}_{i,k}\bar{\zeta}_{j,k'} \rangle = \frac{\sigma_i}{T_s}\delta_{ij}\delta_{kk'}. \tag{5-18b}$$

Similar to its continuous version, the LQR for discrete-time systems returns an optimal control law, expressed as a linear combination on the states $\mathbf{x}_n$,

$$\mathbf{u}_n = -\mathbf{K}_d\mathbf{x}_n, \tag{5-19}$$

however, the expression for the controller's gain changes to

$$\mathbf{K}_d = (\mathbf{R}_d + \mathbf{B}_d^T\mathbf{S}_d\mathbf{B}_d)^{-1}\mathbf{B}_d^T\mathbf{S}_d\mathbf{A}_d, \tag{5-20}$$

where $\mathbf{S}_d$ is the solution of the discrete algebraic Ricatti equation

$$\begin{aligned}\mathbf{S}_d = &\mathbf{A}_d^T\mathbf{S}_d\mathbf{A}_d + \mathbf{Q}_d \\ &- \mathbf{A}_d^T\mathbf{S}_d\mathbf{B}_d(\mathbf{R}_d + \mathbf{B}_d^T\mathbf{S}_d\mathbf{B}_d)^{-1}\mathbf{B}_d^T\mathbf{S}_d\mathbf{A}_d,\end{aligned} \tag{5-21}$$

and $\mathbf{Q}_d$ and $\mathbf{R}_d$ are the matrices defining the cost function J_d for the digital control law, which reads

$$J_d = \frac{1}{2}\sum_{n=0}^{\infty}[\mathbf{x}_n^T\mathbf{Q}_d\mathbf{x}_n + \mathbf{u}_n^T\mathbf{R}_d\mathbf{u}_n]. \tag{5-22}$$

5.6.2 Electronic setup

The control law defined in Eq. (5-19) was implemented using two Red Pitayas, each equipped with a Xilinx Zynq 7010 FPGA and a 2 channel 14-bits ADC, allowing for a maximum sampling frequency of 125 MHz for two distinct inputs, x_a and x_b. The feedback loop incorporated a decimation block, increasing the sampling time T_s from 8.00 ns to 64.00 ns, enabling synchronous execution of more complex tasks.

In Fig. 5.5 a simplified block diagram of the main components implemented within each FPGA is shown. The controller block is responsible for computing the output signal $u_{a,n}$ and $u_{b,n}$, being equivalent to the following expression

$$\begin{bmatrix} u_{a,n} \\ u_{b,n} \end{bmatrix} = \begin{bmatrix} k_{p,aa}^d & k_{p,ab}^d & k_{d,aa}^d & k_{d,ab}^d \\ k_{p,ba}^d & k_{p,bb}^d & k_{d,ba}^d & k_{d,bb}^d \end{bmatrix} \begin{bmatrix} \tilde{x}_{a,n} \\ \tilde{x}_{b,n} \\ \tilde{x}_{a,n-N_a} \\ \tilde{x}_{b,n-N_b} \end{bmatrix}. \tag{5-23}$$

The signals $\tilde{x}_{a,n}$, $\tilde{x}_{b,n}$ result from passing the inputs through a D.C block and a notch filter, both implemented by using digital biquadratic filters. The constant $k_{p,ij}^d$ and $k_{d,ij}^d$ refer to the digital proportional and derivative gains. The signals $\tilde{x}_{a,n-N_a}$, $\tilde{x}_{b,n-N_b}$ are the delayed positions, serving as estimates of the particle's velocity.

The notch filter transfer function is shown in Fig. 5.5b). For the FPGA processing the x and y signals, the transfer function used was H_{xy} to remove harmonic components near Ω_z. In the other FPGA, a filter H_z was applied to remove any components sufficiently close to Ω_x and to Ω_y. The filter's impact on the phase of each signal is approximately constant near each resonance frequency, being included in the overall intrinsic delay of the electronic setup, already described in Section 5.4. The computed control signals were sent to non-inverting analog amplifiers, providing a constant gain $A = 5.00\,\mathrm{V/V}$ with minimal phase impact for signals with harmonic components from D.C up to 150.00 kHz.

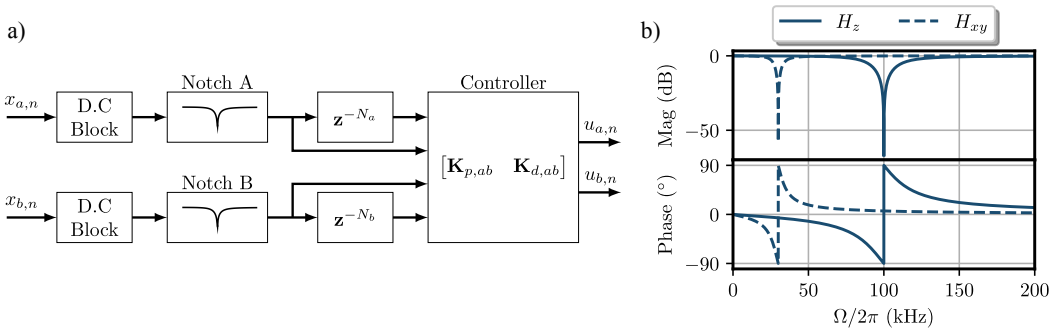

Figure 5.5: Digital electronic implementation. a) Block diagram illustrating the FPGA implementation for stable control of the particle CoM motion. The digital filters are responsible for signal conditioning. A Block Random Access Memory allows the implementation of delay blocks, delaying the signal in multiples (N_a, N_b) of the sampling time. The delayed and non-delayed filtered signals are then transmitted to the controllers to compute the output signals. b) Bode plots for each notch filter H_z and H_{xy}, depicting their magnitude and phase behavior for the frequency range of interest.

5.6.3 Model parameters

Implementation of LQR relies on the accurate extraction of the **A** and **B** matrices, essential for the correct computation of $\mathbf{A}_d$ and $\mathbf{B}_d$. This appendix clarifies how the parameters that allow the reconstruction of these matrices were extracted for the experiment.

5.6.3.1 Detector calibration

Assuming the trapped nanoparticle reaches thermal equilibrium with the residual gas in the vacuum chamber, its initial effective temperature along the three axes is approximately 293 K. Calibration of the detection system involves establishing the linear relationship between the PSD of the detector output for motion along the i-axis, denoted as $S_{V_iV_i}(\Omega)$, and the displacement PSD for the same axis, denoted as $S_{ii}(\Omega)$ [92],

$$S_{V_iV_i}(\Omega) = (C^i_{Vm})^2 S_{ii}(\Omega), \tag{5-24}$$

with C^i_{Vm} representing the calibration factor and $S_{V_iV_i}$ being defined by the Lorentzian function,

$$S_{V_iV_i}(\Omega) = (C^i_{Vm})^2 \frac{2\gamma_m k_B T}{m[(\Omega^2 - \Omega_i^2)^2 + \gamma_m^2 \Omega_i^2]} \tag{5-25}$$

Calibration was done by collecting 10,000 traces, each with a duration of

50 ms. The average PSDs were then fitted to Eq. (5-25), enabling the extraction of C^i_{Vm}, Ω_i and γ_m. The coefficients were found to be

$$C^x_{Vm} = (6.87 \pm 0.72) \times 10^5 \,\mathrm{V/m}$$

$$C^y_{Vm} = (7.08 \pm 0.75) \times 10^5 \,\mathrm{V/m}$$

$$C^z_{Vm} = (1.07 \pm 0.11) \times 10^6 \,\mathrm{V/m}$$

5.6.3.2 Electrodes calibration

To compute the controller's gain matrix $\mathbf{K}_d$ described in Subsection 5.6.1, it is necessary to measure the transduction coefficient C^{ij}_{NV} that provides the linear relation between the applied voltage across the electrodes j and the resulting force along the i-axis. From these, it is possible to reconstruct the terms of the $\mathbf{B}$ matrix, which due to the geometry of the actuators couples the x and y-axes.

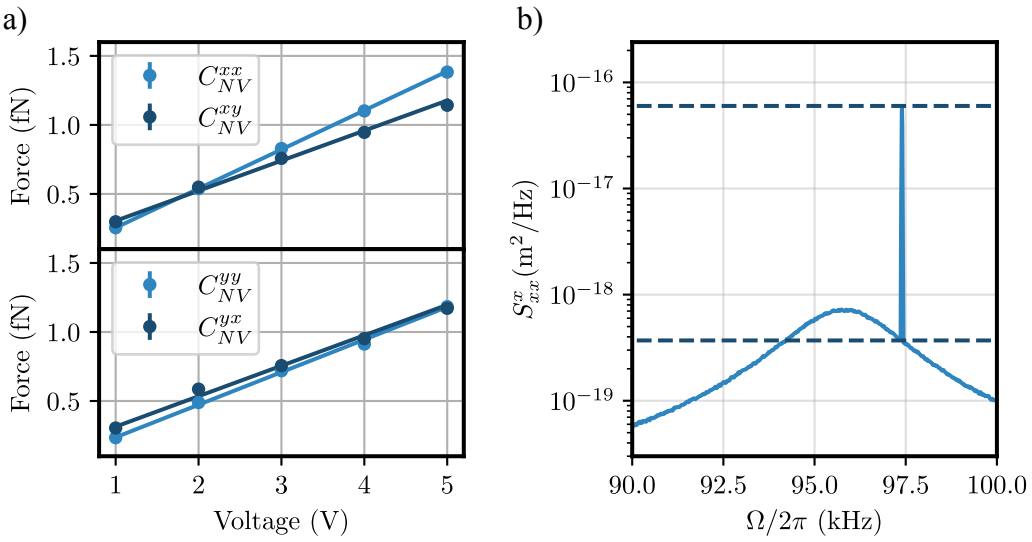

Figure 5.6: Electrode calibration. a) Calibration curves are presented for each coefficient of the xy plane. Each point corresponds to the analysis of 7000 traces with an individual duration of 50 ms. The particle was driven with a sinusoidal signal at $\Omega_{dr}/2\pi = 97.50$ kHz. b) PSD of the particle's CoM motion under the action of a sinusoidal force. The dashed line delineates the peak region from which the amplitude of the force F_0 can be extracted.

Force calibration of the electrodes can be carried out by measuring the particle's response to sinusoidal voltage drives applied to an individual pair of electrodes at known frequencies near each resonance [24]. The driving voltage in

the electrode j introduces a sinusoidal force $F_i^j \cos(\Omega_{dr} t)$ which can be observed within the PSD of the driven CoM motion of the i direction S_{ii}^j,

$$S_{ii}^j = S_{ii}(\Omega) + S_{ii}^{j,el}(\Omega), \tag{5-26}$$

where $S_{ii}(\Omega)$ follows Eq. (5-13) and $S_{ii}^{j,el}(\Omega)$ is

$$S_{ii}^{j,el}(\Omega) = \frac{F_i^{j2} \tau_{el} \,\mathrm{sinc}^2[(\Omega - \Omega_{dr})\tau_{el}]}{m^2[(\Omega^2 - \Omega_i^2)^2 + \gamma_m^2 \Omega^2]}, \tag{5-27}$$

with τ_{el} being the duration of the measure.

In Figure 5.6a), the calibration curves for each coefficient is shown, yielding

$$C_{NV}^{xx} = (2.83 \pm 0.14) \times 10^{-16}\,\mathrm{N/V}$$

$$C_{NV}^{xy} = (2.18 \pm 0.13) \times 10^{-16}\,\mathrm{N/V}$$

$$C_{NV}^{yx} = (2.21 \pm 0.13) \times 10^{-16}\,\mathrm{N/V}$$

$$C_{NV}^{yy} = (2.36 \pm 0.12) \times 10^{-16}\,\mathrm{N/V}$$

An example of one of the PSDs used for calibration is presented in Fig. 5.6b).

5.6.3.3 Gain matrix

After ensuring proper calibration of the detectors and actuators, computation of the LQR gains becomes feasible. Analysis of the PSDs of the x, y and z confirms the trapped nanoparticle's oscillation frequencies $\Omega_x/2\pi = 96.24\,\mathrm{kHz}$, $\Omega_y/2\pi = 101.49\,\mathrm{kHz}$ and $\Omega_z/2\pi = 31.52\,\mathrm{kHz}$. Given the average diameter of the nanoparticle as provided by the manufacturer, the its mass is calculated to be $m \approx 3.37\,\mathrm{fg}$. The weighting and cost-effort matrices used were

$$\mathbf{R}_d = m \begin{bmatrix} \mathrm{diag}(\mathbf{\Omega}^2) & \mathbf{0}_{3\times3} \\ \mathbf{0}_{3\times3} & I_3 \end{bmatrix}, \tag{5-28}$$

and

$$\mathbf{Q}_d = \frac{100}{m} \begin{bmatrix} \Omega_x^{-2} & 0 & 0 \\ 0 & \Omega_y^{-2} & 0 \\ 0 & 0 & \Omega_z^{-2} \end{bmatrix}. \tag{5-29}$$

These matrices were selected to ensure that the cost function J_d possesses appropriate energy units, considering the states measured in S.I units and $\mathbf{u}$ accounting for feedback forces. Such dimensional considerations are crucial for converting the controller's gain from the LQR theory to the digital gains configured in the FPGA. The $\mathbf{B}$ matrix is expressed as

$$\mathbf{B} = \begin{bmatrix} \mathbf{0}_{3\times3} \\ \mathbf{B}_{xyz} \end{bmatrix}, \text{ where } \mathbf{B}_{xyz} = \begin{bmatrix} \mathbf{B}_{xy} & 0 \\ \mathbf{0}_{1\times2} & b_z \end{bmatrix}. \tag{5-30}$$

The submatrix $\mathbf{B}_{xy}$, expressed in kg^{-1}, is determined by m and the proportion of the electrodes coefficients C_{NV}^{ij},

$$\mathbf{B}_{xy} = \frac{1}{m} \begin{bmatrix} -1 & C_{NV}^{xy}/C_{NV}^{xx} \\ C_{NV}^{yx}/C_{NV}^{xx} & C_{NV}^{yy}/C_{NV}^{xx} \end{bmatrix}. \tag{5-31}$$

Without loss of generality, its terms were normalized by the biggest transduction coefficient, C_{NV}^{xx}. The negative sign accounts for the orientation of the electrodes axes, x' and y', as illustrated in Fig. 5.1.

The final parameter required to fully describe the dynamics given by Eq. (5-4), is γ_m. To assess the impact of varying it, we substitute the values for the resonance frequencies, $\mathbf{B}$, T_s, $\mathbf{Q}_d$, and $\mathbf{R}_d$ and compute $\mathbf{K}_d$ for different drag coefficients. The results of this evaluation are depicted in Fig. 5.7. Notably, for pressures below 1 mbar, the influence of γ_m on the controller's gains is negligible. Therefore, under the premise that pressure solely affects the drag coefficient, $\mathbf{K}_d$ can be computed only once, even as pressure reduces.

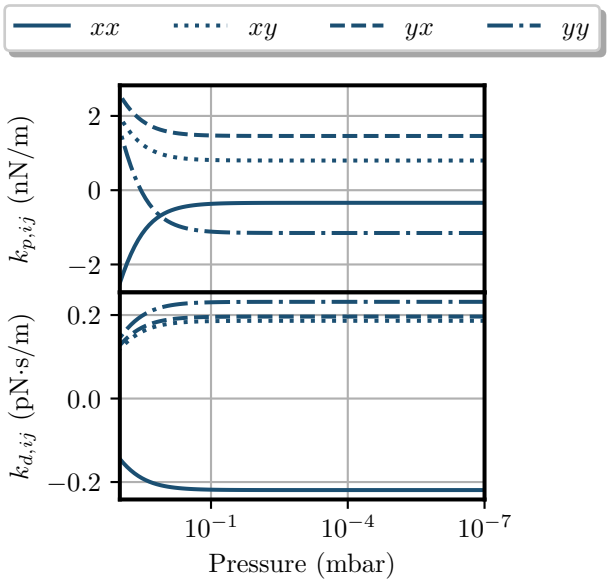

Figure 5.7: Optimal gains dependence with pressure. The constant behavior for values bellow 1 mbar allows one to employ the same matrix $\mathbf{K}_d$ for the underdamped and undamped regimes.

After completing the system characterization, with γ_m considered as zero, $\mathbf{K}_d$ can be properly computed. The next step involves converting the theoretical gains into digital values configured within the FPGA. The following expressions

govern this conversion

$$k^d_{p,ij} = \frac{k_{p,ij}}{AC^{xx}_{NV}C^j_{Vm}}, \tag{5-32a}$$

$$k^d_{d,ij} = -\frac{\Omega_j k_{d,ij}}{AC^{xx}_{NV}C^j_{Vm}}. \tag{5-32b}$$

Here, Ω_j emerges from estimating the velocity as proportional to the delayed position, leading, for example, to $\dot{x} = -\Omega_x x(t - \tau_x)$, for a delay τ_x. The factor C^{xx}_{NV} arises from the $\mathbf{B}_{xy}$ matrix normalization, while C^j_{Vm} is used to convert displacement in the j-axis to output voltages from its detector. In Table 5.1, both theoretical and digital gains are presented. Note that the digital gains had to pass through a conversion to a fixed-point representation during the VHDL implementation, allowing arithmetical operations with minimal loss of numerical resolution [111].

Gain	LQR (Eq. 5-19)	Digital Gains (Eq. 5-32)
$k_{p,xx}$	$-3.40 \times 10^{-10}\,\mathrm{N/m}$	-0.35
$k_{p,xy}$	$7.99 \times 10^{-10}\,\mathrm{N/m}$	0.80
$k_{p,yx}$	$1.46 \times 10^{-9}\ \mathrm{N/m}$	1.50
$k_{p,yy}$	$-1.15 \times 10^{-9}\ \mathrm{N/m}$	-1.15
$k_{d,xx}$	$-2.19 \times 10^{-13}\,\mathrm{N \cdot s/m}$	136.45
$k_{d,xy}$	$1.86 \times 10^{-13}\,\mathrm{N \cdot s/m}$	-119.14
$k_{d,yx}$	$1.96 \times 10^{-13}\,\mathrm{N \cdot s/m}$	-122.22
$k_{d,yy}$	$2.32 \times 10^{-13}\,\mathrm{N \cdot s/m}$	-148.23

Table 5.1: Controller's gains. Values returned by optimal control theory and implemented values within the FPGA are shown according to the system characterization and Eq. (5-32).

6
Outlook

While conclusions of each experiment were separately detailed in their respective chapters, the exploration of numerous potential research avenues remains open for both experiments. This final chapter will outline some of the possibilities that can be implemented in the near future and give general closing remarks.

Exploring nonlinearities and artificial stochastic forces

The fourth chapter of this dissertation detailed the experimental setup, which employed an FPGA to generate a feedback signal represented as $G_{fb}z^3(t)$. This setup offers versatility for exploring various feedback forces, such as the delayed cubic forces detailed in [84], artificial higher-order anharmonicities as discussed in [30], or additional stochastic forces akin to those in [153]. Specifically addressing stochastic forces, the experimental platform can facilitate investigations into the particle's response to colored noise, thereby extending the existing examination of extra stochastic terms. To enable this, the FPGA should first function as a pseudorandom number generator, a topic that will be addressed in more detail here.

Various methods can be used to implement pseudorandom number generators capable of producing a sequence of random numbers conforming to a Gaussian distribution. In electronic systems, generating a Gaussian distribution typically involves capturing environmental noise through open-circuited inputs. However, this approach presents certain challenges that could potentially impact experiments negatively. The resolution of digital conversion electronics and the low amplitude of environment noise (on the order of few mV) result in a limited range of possible distinct values for the distribution. Furthermore, environmental noise is often temperature-dependent, leading to variations in its statistical properties with changes in the room temperature [154].

An alternative approach involves employing Linear-Feedback Shift Register (LFSR) generators [155], which were first introduced by Tausworthe in [156]. The general structure of a LFSR is illustrated in Fig. 6.1a), where a set of linear operations, typically XOR operations, are applied to an N-bit variable.

The specific bits used in the operations are called *taps*. After applying XOR operations to the designated taps sequentially, all bits are right-shifted, and the leftmost bit becomes the result of the XOR operations. The starting value of the LSFR is denominated *seed*. This process is iterated at fixed time-steps, producing a sequence of pseudorandom numbers following a uniform distribution. The arrangement of taps determines the number of different values this sequence can possess, constrained by $2^N - 1$, where N is the number of bits in the variable. While identifying the optimal tap positions for achieving maximum-length LFSRs falls outside the scope of this dissertation, interested readers can refer to [157] for more details.

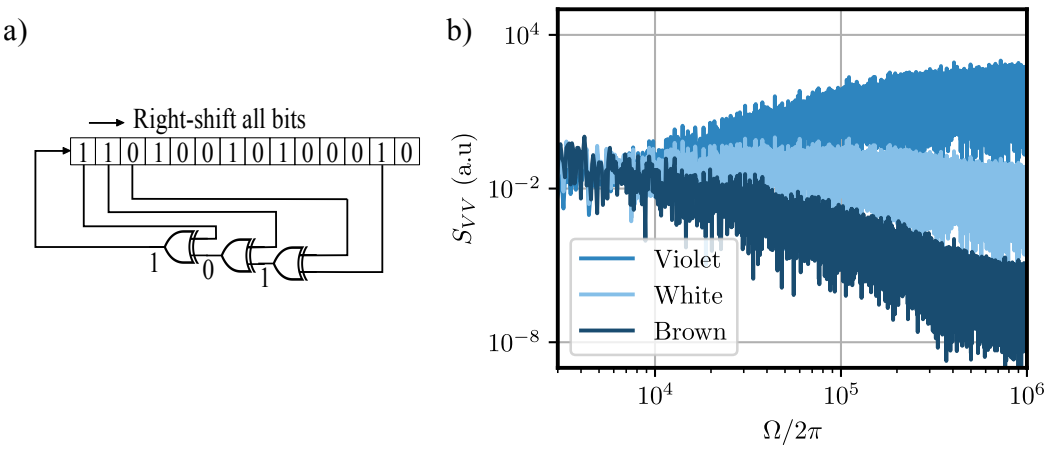

Figure 6.1: Pseudorandom number generation. a) A maximum length 14-bit LSFR structure with taps located at bits 2, 12, 13 and 14. b) PSD of synthetically created white and colored noises.

By implementing multiples LSFRs with distinct seeds and summing their outputs, it becomes possible to generate a pseudorandom number signal that, according to the central limit theorem, conforms to a Gaussian distribution. White noise with an arbitrary standard deviation can be generated straightforwardly in this manner, and colored noise, as brown and violet noise, can be produced by applying discrete integration or differentiation operators. Figure 6.1b) shows the PSD of white, brown and violet noise generated considering the sum of 50 14-bit LFSRs. The synthesized white noise presents an almost flat band across the frequency spectrum, while brown and violet noises are defined by a decrease and increase of 20 dB/dec, respectively. This definition is outlined in the Federal Standard 1037C of the Telecommunications Glossary [158].

A roadmap to ground-state cooling

Despite the demonstration of 3-D cooling presented in Chapter 5, to achieve ground-state cooling some steps are necessary. Firstly, ground-state cooling of levitated silica nanoparticles has been accomplished at pressures on the order of $\approx 10^{-9}$ mbar [14, 15]. This means that an improvement by a factor of 10^4 is necessary given the minimal pressure reached in the all-electrical cooling experiment. Achieving this enhancement could involve replacing vacuum elements incompatible with ultra-high vacuum, incorporating an ion pump, and employing chamber baking to reach the necessary vacuum level.

A significant upgrade to the experimental setup would involve replacing the current pair of lenses used for trapping and collection. Substitution of the trapping lens with the Lightpath 355617 aspheric lens would increase the NA used for trapping from 0.68 to 0.75, resulting in higher resonance frequencies for the nanoparticle's motion. This modification would require a corresponding adjustment in the collection lens to optimize light collection efficiency. Additionally, two other important improvements in terms of detection would involve implementing collection of light backscattered by the particle to enhance the Signal-to-Noise Ratio (SNR) for the z-axis detection [145] and incorporating a heterodyne detection scheme to enable absolute measurement of the particle's effective temperature [159].

Finally, modifications on the controller and actuators are necessary. To implement the LQG control law for the particle's 3-D motion, as simulated in Chapter 3, the actuator responsible for the z direction must be correctly characterized, and the estimation method used should be substituted with a LQE. However, as observed in the experiment, silica nanoparticles undergo changes in their properties as pressure decreases. These changes directly affect the validity of the characterization, and, therefore, jeopardize the LQG's implementation. Solving this issue could be approached in two ways. One approach would be to control the particle's charge as conducted in [152]. Alternatively, it is possible to expand the controller's policy to accommodate a regime where the system's parameters are unknown.

Adaptive control theory offers algorithms for stable control of linear, stochastic and nonlinear systems with unknown parameters [62] or even partially known dynamics [59, 160], with techniques ranging from parameters estimation to self-tunning controllers. A particularly interesting controller is the Model-Reference Adaptive Controller (MRAC). While most controllers focus on making a system behave according to a reference signal $y_d(t)$, MRAC focuses on determining the correct control law $\mathbf{u}(t)$ capable of making a linear system,

such as the one described in Eq. (6-1a), mimic the behavior of a reference system with the same order, Eq. (6-1b), when this reference process is being excited by a command signal $\mathbf{u}_c(t)$. In Eq. (6-1), $\mathbf{x}_r(t)$ refers to the state-vector trajectory for the reference system defined by the matrices $\mathbf{A}_r$ and $\mathbf{B}_r$, and $\mathbf{x}(t)$ the state-trajectory for the nominal system.

$$\dot{\mathbf{x}}(t) = \mathbf{A}\mathbf{x}(t) + \mathbf{B}\mathbf{u}(t), \tag{6-1a}$$

$$\dot{\mathbf{x}}_r(t) = \mathbf{A}_r\mathbf{x}_r(t) + \mathbf{B}_r\mathbf{u}_c(t). \tag{6-1b}$$

To make $\mathbf{x}(t)$ follow $\mathbf{x}_r(t)$, $\mathbf{u}(t)$ must adhere to

$$\mathbf{u}(t) = \mathbf{B}^{-1}[(\mathbf{A}_r - \mathbf{A})\mathbf{x}(t) + \mathbf{B}_r\mathbf{u}_c(t)], \tag{6-2}$$

which is feasible only if $\mathbf{B}^{-1}$, the left inverse of $\mathbf{B}$, exists. The main challenge in computing Eq. (6-2) lies in the fact that only the matrices $\mathbf{A}_r$ and $\mathbf{B}_r$ are known. Due to the lack of information of the system parameters, an alternative control law must implemented,

$$\mathbf{u}(t) = -\mathbf{K}_\mathbf{x}(t)\mathbf{x}(t) + \mathbf{K}_\mathbf{u}(t)\mathbf{u}_c(t), \tag{6-3}$$

where $\mathbf{K}_\mathbf{x}(t)$ and $\mathbf{K}_\mathbf{u}(t)$ are estimations of $-\mathbf{B}^{-1}(\mathbf{A}_r - \mathbf{A})$ and $\mathbf{B}^{-1}\mathbf{B}_r$, respectively. MRAC provides the adaptation rules for these estimations, ensuring convergence from $\mathbf{x}(t)$ to $\mathbf{x}_r(t)$. These rules are governed by Eq. (6-4), where $\mathbf{e}(t)$ represents the error vector, defined as $\mathbf{e}(t) = \mathbf{x}(t) - \mathbf{x}_r(t)$, and $\mathbf{\Gamma}$ is the adaptation gain matrix, a symmetric positive-defined matrix, with its elements defined within the controller's project. The proof of Eq. (6-4) is cumbersome, but can be conducted by analysing the necessary conditions for the Lyapunov stability of the closed-loop system. For more details we refer to [161].

$$\dot{\mathbf{K}}_\mathbf{x}(t) = \mathbf{B}_r^T\mathbf{\Gamma}\mathbf{e}(t)\mathbf{x}^T(t), \tag{6-4a}$$

$$\dot{\mathbf{K}}_\mathbf{u}(t) = -\mathbf{B}_r^T\mathbf{\Gamma}\mathbf{e}(t)\mathbf{u}_c^T(t). \tag{6-4b}$$

To showcase the effectiveness of MRAC, Fig. 6.2 presents application of this adaptive controller to a second-order system as a toy-problem scenario. The command signal $\mathbf{u}_c(t)$ used was a combination of a cold damping controller and an additional stimulus signal, a square wave at 80 kHz. This stimulus signal is added to reduce the likelihood of incorrect estimation, which commonly occurs when both $\mathbf{x}(t)$ and $\mathbf{x}_r(t)$ have reduced amplitudes, consequently diminishing $\mathbf{u}_c(t)$ and the adaptation factors $\dot{\mathbf{K}}_\mathbf{x}(t)$ and $\dot{\mathbf{K}}_\mathbf{u}(t)$. Figure 6.2b) presents the artificial b^* term of the closed-loop system, which starts in b and correctly converges to b_r after approximately 1.5 ms.

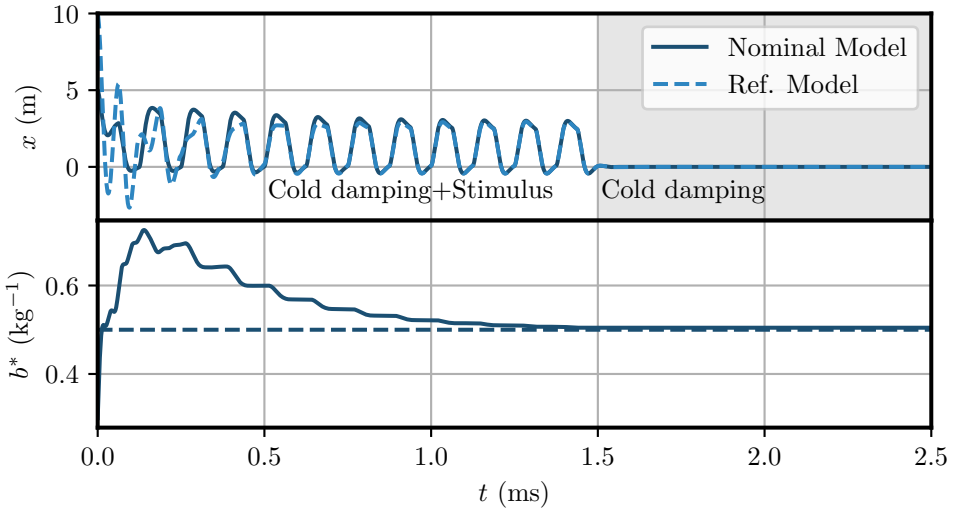

Figure 6.2: MRAC. Parameters used for simulation: $\gamma_{m,r} = \gamma_m = 80\,\mathrm{kHz}$, $\Omega_{0,r}/2\pi = \Omega_0/2\pi = 80\,\mathrm{kHz}$, $b_r = 0.5\,\mathrm{kg}^{-1}$ and $b = 0.3\,\mathrm{kg}^{-1}$. a) Trajectories for both nominal and reference model. The gray shaded area marks the region where only cold damping was used. b) Effective b^* parameter (solid line) resulted from applying adaptive control. Dashed line represents the reference model value.

In the context of levitodynamics, the directly application of this method for feedback cooling involves considering $\mathbf{u}_c(t)$ as the signal returned by LQG. When considering the MRAC correct convergence, only the parameters of the reference model would be required in this approach, eliminating the need of proper system calibration. Additionally, if parameters change, but much slower than the particle dynamics or the controller's processing capability, MRAC should be capable of correctly re-adapting the matrices $\mathbf{K}_\mathbf{x}(t)$ and $\mathbf{K}_\mathbf{u}(t)$, thereby effectively counteracting any variations in the system parameters.

Closing remarks

This dissertation explored feedback control theory within the domain of optically levitated nanoparticles. Albeit the points already raised in this outlook focused on technical aspects of specific future research paths, both experimental apparatus (at 780 nm and 1550 nm) could be employed for research on a much more vast variety of areas, some of which levitodynamics has already found successful results, both for applied and fundamental research. Lastly, the presented findings represent the initial steps towards a long-term goal: ground-state cooling and quantum control of a mesoscopic particle.

Bibliography

[1] A. Einstein *et al.*, *Zur quantentheorie der strahlung*. Hirzel Leipzig, 1917, vol. 18.

[2] E. F. Nichols and G. F. Hull, "A preliminary communication on the pressure of heat and light radiation," *Physical Review (Series I)*, vol. 13, no. 5, p. 307, 1901.

[3] P. Lebedew, "Untersuchungen über die druckkräfte des lichtes," *Annalen der Physik*, vol. 311, no. 11, pp. 433–458, 1901.

[4] J. Millen, T. S. Monteiro, R. Pettit, and A. N. Vamivakas, "Optomechanics with levitated particles," *Reports on Progress in Physics*, vol. 83, no. 2, p. 026401, 2020.

[5] F. Marquardt and S. M. Girvin, "Optomechanics," *Physics*, vol. 2, p. 40, 2009.

[6] R. Reimann, M. Doderer, E. Hebestreit, R. Diehl, M. Frimmer, D. Windey, F. Tebbenjohanns, and L. Novotny, "Ghz rotation of an optically trapped nanoparticle in vacuum," *Physical review letters*, vol. 121, no. 3, p. 033602, 2018.

[7] J. A. Zielińska, F. van der Laan, A. Norrman, R. Reimann, M. Frimmer, and L. Novotny, "Spinning a levitated mechanical oscillator far into the deep-strong coupling regime," *arXiv preprint arXiv:2310.03706*, 2023.

[8] F. M. Fazal and S. M. Block, "Optical tweezers study life under tension," *Nature photonics*, vol. 5, no. 6, pp. 318–321, 2011.

[9] H. M. Nussenzveig, "Cell membrane biophysics with optical tweezers," *European Biophysics Journal*, vol. 47, no. 5, pp. 499–514, 2018.

[10] B. Abbott, R. Abbott, R. Adhikari, P. Ajith, B. Allen, G. Allen, R. Amin, S. Anderson, W. Anderson, M. Arain *et al.*, "Ligo: the laser interferometer gravitational-wave observatory," *Reports on Progress in Physics*, vol. 72, no. 7, p. 076901, 2009.

[11] J. Thompson, B. Zwickl, A. Jayich, F. Marquardt, S. Girvin, and J. Harris, "Strong dispersive coupling of a high-finesse cavity to a micromechanical membrane," *Nature*, vol. 452, no. 7183, pp. 72–75, 2008.

[12] J. Chan, T. M. Alegre, A. H. Safavi-Naeini, J. T. Hill, A. Krause, S. Gröblacher, M. Aspelmeyer, and O. Painter, "Laser cooling of a nanomechanical oscillator into its quantum ground state," *Nature*, vol. 478, no. 7367, pp. 89–92, 2011.

[13] U. Delić, M. Reisenbauer, K. Dare, D. Grass, V. Vuletić, N. Kiesel, and M. Aspelmeyer, "Cooling of a levitated nanoparticle to the motional quantum ground state," *Science*, vol. 367, no. 6480, pp. 892–895, 2020.

[14] L. Magrini, P. Rosenzweig, C. Bach, A. Deutschmann-Olek, S. G. Hofer, S. Hong, N. Kiesel, A. Kugi, and M. Aspelmeyer, "Real-time optimal quantum control of mechanical motion at room temperature," *Nature*, vol. 595, no. 7867, pp. 373–377, 2021.

[15] F. Tebbenjohanns, M. L. Mattana, M. Rossi, M. Frimmer, and L. Novotny, "Quantum control of a nanoparticle optically levitated in cryogenic free space," *Nature*, vol. 595, no. 7867, pp. 378–382, 2021.

[16] A. Ashkin, "Acceleration and trapping of particles by radiation pressure," *Physical review letters*, vol. 24, no. 4, p. 156, 1970.

[17] A. Ashkin, J. M. Dziedzic, and T. Yamane, "Optical trapping and manipulation of single cells using infrared laser beams," *Nature*, vol. 330, no. 6150, pp. 769–771, 1987.

[18] A. Ashkin and J. Dziedzic, "Feedback stabilization of optically levitated particles," *Applied Physics Letters*, vol. 30, no. 4, pp. 202–204, 1977.

[19] A. Ashkin, J. M. Dziedzic, J. E. Bjorkholm, and S. Chu, "Observation of a single-beam gradient force optical trap for dielectric particles," *Optics letters*, vol. 11, no. 5, pp. 288–290, 1986.

[20] A. Ashkin, "Trapping of atoms by resonance radiation pressure," *Physical Review Letters*, vol. 40, no. 12, p. 729, 1978.

[21] K. Stannigel, P. Rabl, A. S. Sørensen, P. Zoller, and M. D. Lukin, "Optomechanical transducers for long-distance quantum communication," *Physical review letters*, vol. 105, no. 22, p. 220501, 2010.

[22] G. Ranjit, M. Cunningham, K. Casey, and A. A. Geraci, "Zeptonewton force sensing with nanospheres in an optical lattice," *Physical Review A*, vol. 93, no. 5, p. 053801, 2016.

[23] F. Monteiro, S. Ghosh, A. G. Fine, and D. C. Moore, "Optical levitation of 10-ng spheres with nano-g acceleration sensitivity," *Physical Review A*, vol. 96, no. 6, p. 063841, 2017.

[24] F. Ricci, M. T. Cuairan, G. P. Conangla, A. W. Schell, and R. Quidant, "Accurate mass measurement of a levitated nanomechanical resonator for precision force-sensing," *Nano letters*, vol. 19, no. 10, pp. 6711–6715, 2019.

[25] J. Millen, T. Deesuwan, P. Barker, and J. Anders, "Nanoscale temperature measurements using non-equilibrium brownian dynamics of a levitated nanosphere," *Nature nanotechnology*, vol. 9, no. 6, pp. 425–429, 2014.

[26] O. Romero-Isart, A. C. Pflanzer, F. Blaser, R. Kaltenbaek, N. Kiesel, M. Aspelmeyer, and J. I. Cirac, "Large quantum superpositions and interference of massive nanometer-sized objects," *Physical review letters*, vol. 107, no. 2, p. 020405, 2011.

[27] J. Bateman, S. Nimmrichter, K. Hornberger, and H. Ulbricht, "Near-field interferometry of a free-falling nanoparticle from a point-like source," *Nature communications*, vol. 5, no. 1, p. 4788, 2014.

[28] S. Barzanjeh, A. Xuereb, S. Gröblacher, M. Paternostro, C. A. Regal, and E. M. Weig, "Optomechanics for quantum technologies," *Nature Physics*, vol. 18, no. 1, pp. 15–24, 2022.

[29] J. Gieseler, L. Novotny, and R. Quidant, "Thermal nonlinearities in a nanomechanical oscillator," *Nature physics*, vol. 9, no. 12, pp. 806–810, 2013.

[30] B. Suassuna, B. Melo, and T. Guerreiro, "Path integrals and nonlinear optical tweezers," *Physical Review A*, vol. 103, no. 1, p. 013110, 2021.

[31] M. Debiossac, D. Grass, J. J. Alonso, E. Lutz, and N. Kiesel, "Thermodynamics of continuous non-markovian feedback control," *Nature communications*, vol. 11, no. 1, p. 1360, 2020.

[32] M. Innerbichler, A. Militaru, M. Frimmer, L. Novotny, and C. Dellago, "White-noise fluctuation theorem for langevin dynamics," *New Journal of Physics*, vol. 24, no. 11, p. 113028, 2022.

[33] N. Meyer, A. De los Rios Sommer, P. Mestres, J. Gieseler, V. Jain, L. Novotny, and R. Quidant, "Resolved-sideband cooling of a levitated nanoparticle in the presence of laser phase noise," *Physical review letters*, vol. 123, no. 15, p. 153601, 2019.

[34] J. Gieseler, B. Deutsch, R. Quidant, and L. Novotny, "Subkelvin parametric feedback cooling of a laser-trapped nanoparticle," *Physical review letters*, vol. 109, no. 10, p. 103603, 2012.

[35] J. Vijayan, Z. Zhang, J. Piotrowski, D. Windey, F. van der Laan, M. Frimmer, and L. Novotny, "Scalable all-optical cold damping of levitated nanoparticles," *Nature Nanotechnology*, vol. 18, no. 1, pp. 49–54, 2023.

[36] F. Tebbenjohanns, M. Frimmer, A. Militaru, V. Jain, and L. Novotny, "Cold damping of an optically levitated nanoparticle to microkelvin temperatures," *Physical review letters*, vol. 122, no. 22, p. 223601, 2019.

[37] G. P. Conangla, F. Ricci, M. T. Cuairan, A. W. Schell, N. Meyer, and R. Quidant, "Optimal feedback cooling of a charged levitated nanoparticle with adaptive control," *Physical review letters*, vol. 122, no. 22, p. 223602, 2019.

[38] H. M. Wiseman and G. J. Milburn, *Quantum measurement and control*. Cambridge university press, 2009.

[39] O. Kremer, I. Califrer, D. Tandeitnik, and T. Guerrerio, 2024. [Online]. Available: https://github.com/QuantumAdventures/non-linearity-experiment

[40] O. Kremer, G. Temporao, and T. Guerreiro, 2024. [Online]. Available: https://github.com/oscarkremer/dissertation-codes

[41] L. Novotny and B. Hecht, *Principles of nano-optics*. Cambridge university press, 2012.

[42] P. H. Jones, O. M. Maragò, and G. Volpe, *Optical tweezers: Principles and applications*. Cambridge University Press, 2015.

[43] A. E. Siegman, *Lasers*. University science books, 1986.

[44] B. E. Saleh and M. C. Teich, *Fundamentals of photonics*. john Wiley & sons, 2019.

[45] E. Wolf, "Electromagnetic diffraction in optical systems-i. an integral representation of the image field," *Proceedings of the Royal Society of London. Series A. Mathematical and Physical Sciences*, vol. 253, no. 1274, pp. 349–357, 1959.

[46] B. Richards and E. Wolf, "Electromagnetic diffraction in optical systems, ii. structure of the image field in an aplanatic system," *Proceedings of the Royal Society of London. Series A. Mathematical and Physical Sciences*, vol. 253, no. 1274, pp. 358–379, 1959.

[47] Y. Harada and T. Asakura, "Radiation forces on a dielectric sphere in the rayleigh scattering regime," *Optics communications*, vol. 124, no. 5-6, pp. 529–541, 1996.

[48] I. C. Lenton, A. B. Stilgoe, H. Rubinsztein-Dunlop, and T. A. Nieminen, "Visual guide to optical tweezers," *European Journal of Physics*, vol. 38, no. 3, p. 034009, 2017.

[49] S. Albaladejo, M. I. Marqués, M. Laroche, and J. J. Sáenz, "Scattering forces from the curl of the spin angular momentum of a light field," *Physical review letters*, vol. 102, no. 11, p. 113602, 2009.

[50] S. Beresnev, V. Chernyak, and G. Fomyagin, "Motion of a spherical particle in a rarefied gas. part 2. drag and thermal polarization," *Journal of Fluid Mechanics*, vol. 219, pp. 405–421, 1990.

[51] V. Jain, J. Gieseler, C. Moritz, C. Dellago, R. Quidant, and L. Novotny, "Direct measurement of photon recoil from a levitated nanoparticle," *Physical review letters*, vol. 116, no. 24, p. 243601, 2016.

[52] R. G. Brown and P. Y. Hwang, "Introduction to random signals and applied kalman filtering: with matlab exercises and solutions," *Introduction to random signals and applied Kalman filtering: with MATLAB exercises and solutions*, 1997.

[53] S. Miller and D. Childers, *Probability and random processes: With applications to signal processing and communications*. Academic Press, 2012.

[54] K. Berg-Sørensen and H. Flyvbjerg, "Power spectrum analysis for optical tweezers," *Review of Scientific Instruments*, vol. 75, no. 3, pp. 594–612, 2004.

[55] E. Hebestreit, M. Frimmer, R. Reimann, and L. Novotny, "Sensing static forces with free-falling nanoparticles," *Physical review letters*, vol. 121, no. 6, p. 063602, 2018.

[56] J. Gieseler, J. R. Gomez-Solano, A. Magazzù, I. P. Castillo, L. P. García, M. Gironella-Torrent, X. Viader-Godoy, F. Ritort, G. Pesce, A. V. Arzola *et al.*, "Optical tweezers—from calibration to applications: a tutorial," *Advances in Optics and Photonics*, vol. 13, no. 1, pp. 74–241, 2021.

[57] C. Genes, D. Vitali, P. Tombesi, S. Gigan, and M. Aspelmeyer, "Ground-state cooling of a micromechanical oscillator: Comparing cold damping and cavity-assisted cooling schemes," *Physical Review A*, vol. 77, no. 3, p. 033804, 2008.

[58] F. Lewis, C. Abdallah, and D. Dawson, "Control of robot," *Manipulators, Editorial Maxwell McMillan, Canada*, pp. 25–36, 1993.

[59] J.-J. E. Slotine, W. Li *et al.*, *Applied nonlinear control*. Prentice hall Englewood Cliffs, NJ, 1991, vol. 199, no. 1.

[60] M. W. Spong, S. Hutchinson, and M. Vidyasagar, *Robot modeling and control*. John Wiley & Sons, 2020.

[61] K. J. Åström, *Introduction to stochastic control theory*. Courier Corporation, 2012.

[62] K. J. Åström and B. Wittenmark, *Adaptive control*. Courier Corporation, 2013.

[63] J. Degrave, F. Felici, J. Buchli, M. Neunert, B. Tracey, F. Carpanese, T. Ewalds, R. Hafner, A. Abdolmaleki, D. de Las Casas *et al.*, "Magnetic control of tokamak plasmas through deep reinforcement learning," *Nature*, vol. 602, no. 7897, pp. 414–419, 2022.

[64] G. W. Swan *et al.*, *Applications of optimal control theory in biomedicine*. M. Dekker New York, 1984.

[65] A. E. Bryson, *Control of spacecraft and aircraft*. Princeton university press Princeton, 1993, vol. 41.

[66] G. F. Franklin, J. D. Powell, and A. Emami-Naeini, *Feedback control of dynamic systems*. Pearson London, 2015, vol. 33.

[67] A. V. Oppenheim, A. S. Willsky, S. H. Nawab, and J.-J. Ding, *Signals and systems*. Prentice hall Upper Saddle River, NJ, 1997, vol. 2.

[68] Q. Wu, L. Mancino, M. Carlesso, M. A. Ciampini, L. Magrini, N. Kiesel, and M. Paternostro, "Nonequilibrium quantum thermodynamics of a particle trapped in a controllable time-varying potential," *PRX Quantum*, vol. 3, no. 1, p. 010322, 2022.

[69] D. E. Kirk, *Optimal control theory: an introduction*. Courier Corporation, 2004.

[70] E. B. Lee and L. Markus, *Foundations of optimal control theory*. Wiley New York, 1967, vol. 87.

[71] H. J. Sussmann and J. C. Willems, "300 years of optimal control: from the brachystochrone to the maximum principle," *IEEE Control Systems Magazine*, vol. 17, no. 3, pp. 32–44, 1997.

[72] G. F. Franklin, J. D. Powell, M. L. Workman *et al.*, *Digital control of dynamic systems*. Addison-wesley Menlo Park, CA, 1998, vol. 3.

[73] M. Briers, A. Doucet, and S. Maskell, "Smoothing algorithms for state–space models," *Annals of the Institute of Statistical Mathematics*, vol. 62, pp. 61–89, 2010.

[74] R. J. Hyndman and G. Athanasopoulos, *Forecasting: principles and practice*. OTexts, 2018.

[75] D. Simon, *Optimal state estimation: Kalman, H infinity, and nonlinear approaches*. John Wiley & Sons, 2006.

[76] R. E. Kalman *et al.*, "A new approach to linear filtering and prediction problems [j]," *Journal of basic Engineering*, vol. 82, no. 1, pp. 35–45, 1960.

[77] S. Zhao and B. Huang, "Trial-and-error or avoiding a guess? initialization of the kalman filter," *Automatica*, vol. 121, p. 109184, 2020.

[78] B. D. Anderson and J. B. Moore, *Optimal filtering*. Courier Corporation, 2012.

[79] E. Todorov, "General duality between optimal control and estimation," in *2008 47th IEEE Conference on Decision and Control*. IEEE, 2008, pp. 4286–4292.

[80] W. H. Fleming and R. W. Rishel, *Deterministic and stochastic optimal control*. Springer Science & Business Media, 2012, vol. 1.

[81] J. Richalet and D. O'Donovan, *Predictive functional control: principles and industrial applications*. Springer Science & Business Media, 2009.

[82] A. Ghosh, P. Kumar, C. Sommer, F. G. Jimenez, V. Sudhir, and C. Genes, "Theory of phase-adaptive parametric cooling," *Physical Review A*, vol. 107, no. 5, p. 053521, 2023.

[83] A. Yariv, *Quantum electronics*. John Wiley & Sons, 1989.

[84] O. Kremer, D. Tandeitnik, R. Mufato, I. Califrer, B. Calderoni, F. Calliari, B. Melo, G. Temporão, and T. Guerreiro, "Perturbative nonlinear feedback forces for optical levitation experiments," *arXiv preprint arXiv:2309.15976*, 2023.

[85] C. Gonzalez-Ballestero, M. Aspelmeyer, L. Novotny, R. Quidant, and O. Romero-Isart, "Levitodynamics: Levitation and control of microscopic objects in vacuum," *Science*, vol. 374, no. 6564, p. eabg3027, 2021.

[86] J. Gieseler and J. Millen, "Levitated nanoparticles for microscopic thermodynamics—a review," *Entropy*, vol. 20, no. 5, p. 326, 2018.

[87] J. Gieseler, R. Quidant, C. Dellago, and L. Novotny, "Dynamic relaxation of a levitated nanoparticle from a non-equilibrium steady state," *Nature Nanotechnology*, vol. 9, pp. 358–364, 2014.

[88] V. Svak, J. Flajšmanová, L. Chvátal, M. Šiler, A. Jonáš, J. Ježek, S. H. Simpson, P. Zemánek, and O. Brzobohatý, "Stochastic dynamics of optically bound matter levitated in vacuum," *Optica*, vol. 8, no. 2, 2021.

[89] J. Sheng, C. Yang, and H. Wu, "Nonequilibrium thermodynamics in cavity optomechanics," *Fundamental Research*, vol. 3, no. 1, pp. 75–86, 2023.

[90] G. Gasbarri, A. Belenchia, M. Carlesso, S. Donadi, A. Bassi, R. Kaltenbaek, M. Paternostro, and H. Ulbricht, "Testing the foundation of quantum physics in space via interferometric and non-interferometric experiments with mesoscopic nanoparticles," *Communication Physics*, vol. 4, no. 155, 2021.

[91] R. M. Pettit, W. Ge, P. Kumar, D. R. Luntz-Martin, J. T. Schultz, L. P. Neukirch, M. Bhattacharya, and A. N. Vamivakas, "An optical tweezer phonon laser," *Nature Photonics*, vol. 13, pp. 402–405, 2019.

[92] E. Hebestreit, M. Frimmer, R. Reimann, C. Dellago, F. Ricci, and L. Novotny, "Calibration and energy measurement of optically levitated nanoparticle sensors," *Review of Scientific Instruments*, vol. 89, no. 3, 2018.

[93] L. A. Defaveri, S. M. D. Queirós, and W. A. Morgado, "Dependence of efficiency on the nonlinear nature of a nanomachine," *Physical Review E*, vol. 98, no. 6, p. 062106, 2018.

[94] L. A. C. A. Defaveri, W. A. M. Morgado, and S. M. D. Queirós, "Power output for a nonlinear brownian machine," *Physical Review E*, vol. 96, no. 052115, 2017.

[95] F. Albarelli, A. Ferraro, M. Paternostro, and M. G. Paris, "Nonlinearity as a resource for nonclassicality in anharmonic systems," *Physical Review A*, vol. 93, no. 3, p. 032112, 2016.

[96] L. Neumeier, M. A. Ciampini, O. Romero-Isart, M. Aspelmeyer, and N. Kiesel, "Fast quantum interference of a nanoparticle via optical potential control," *arXiv preprint arXiv:2207.12539*, 2022.

[97] Y. Yang, Y.-X. Ren, M. Chen, Y. Arita, and C. Rosales-Guzmán, "Optical trapping with structured light: a review," *Advanced Photonics*, vol. 3, no. 3, pp. 034 001–034 001, 2021.

[98] L. Rondin, J. Gieseler, F. Ricci, R. Quidant, C. Dellago, and L. Novotny, "Direct measurement of kramers turnover with a levitated nanoparticle," *Nature nanotechnology*, vol. 12, no. 12, pp. 1130–1133, 2017.

[99] F. Ricci, R. A. Rica, M. Spasenović, J. Gieseler, L. Rondin, L. Novotny, and R. Quidant, "Optically levitated nanoparticle as a model system for stochastic bistable dynamics," *Nature communications*, vol. 8, no. 1, p. 15141, 2017.

[100] Y. Zhang, J. Shen, C. Min, Y. Jin, Y. Jiang, J. Liu, S. Zhu, Y. Sheng, A. V. Zayats, and X. Yuan, "Nonlinearity-induced multiplexed optical trapping and manipulation with femtosecond vector beams," *Nano Letters*, vol. 18, no. 9, pp. 5538–5543, 2017.

[101] M. A. Ciampini, T. Wenzl, M. Konopik, E. Lutz, G. Thalhammer, M. Ritsch-Marte, M. Aspelmeyer, and N. Kiesel, "Non-equilibrium memories with levitated nanoparticles: experimental verification of the generalised landauer's principle," in *Optical Trapping and Optical Micromanipulation XVII*, vol. 11463. SPIE, 2020, p. 114631N.

[102] B. P. da Silva, V. Pinillos, D. Tasca, L. Oxman, and A. Khoury, "Pattern revivals from fractional gouy phases in structured light," *Physical review letters*, vol. 124, no. 3, p. 033902, 2020.

[103] H. Moradi, V. Shahabadi, E. Madadi, E. Karimi, and F. Hajizadeh, "Efficient optical trapping with cylindrical vector beams," *Optics express*, vol. 27, no. 5, pp. 7266–7276, 2019.

[104] B. Melo, I. Brandão, R. Rodrigues, A. Khoury, T. Guerreiro *et al.*, "Optical trapping in a dark focus," *Physical Review Applied*, vol. 14, no. 3, p. 034069, 2020.

[105] F. Almeida, I. Sousa, O. Kremer, B. P. da Silva, D. S. Tasca, A. Z. Khoury, G. Temporão, and T. Guerreiro, "Trapping microparticles in a structured dark focus," *Phys. Rev. Lett.*, vol. 131, p. 163601, Oct 2023.

[106] C. C. Chow and M. A. Buice, "Path integral methods for stochastic differential equations," *The Journal of Mathematical Neuroscience (JMN)*, vol. 5, pp. 1–35, 2015.

[107] M. T. Cuairan, J. Gieseler, N. Meyer, and R. Quidant, "Precision calibration of the duffing oscillator with phase control," *Physical Review Letters*, vol. 128, no. 21, p. 213601, 2022.

[108] N. Bullier, A. Pontin, and P. Barker, "Quadratic optomechanical cooling of a cavity-levitated nanosphere," *Physical Review Research*, vol. 3, no. 3, p. L032022, 2021.

[109] S. Lloyd and J.-J. E. Slotine, "Quantum feedback with weak measurements," *Physical Review A*, vol. 62, no. 1, p. 012307, 2000.

[110] R. Schaumann, H. Xiao, and V. V. Mac, *Design of analog filters*, 2nd ed. Oxford University Press, Inc., 2009.

[111] P. Wilson, *Design recipes for FPGAs*. Newnes, 2015.

[112] O. Romero-Isart, "Quantum superposition of massive objects and collapse models," *Physical Review A*, vol. 84, no. 5, p. 052121, 2011.

[113] O. Kremer, I. Califrer, D. Tandeitnik, J. P. von der Weid, G. Temporão, and T. Guerreiro, "All electrical cooling of an optically levitated nanoparticle," *In preparation*, 2024.

[114] W. Paul, "Electromagnetic traps for charged and neutral particles," *Reviews of modern physics*, vol. 62, no. 3, p. 531, 1990.

[115] D. Goldwater, B. A. Stickler, L. Martinetz, T. E. Northup, K. Hornberger, and J. Millen, "Levitated electromechanics: all-electrical cooling of charged nano-and micro-particles," *Quantum Science and Technology*, vol. 4, no. 2, p. 024003, 2019.

[116] L. Dania, D. S. Bykov, M. Knoll, P. Mestres, and T. E. Northup, "Optical and electrical feedback cooling of a silica nanoparticle levitated in a paul trap," *Physical Review Research*, vol. 3, no. 1, p. 013018, 2021.

[117] D. S. Bykov, M. Meusburger, L. Dania, and T. E. Northup, "Hybrid electro-optical trap for experiments with levitated particles in vacuum," *Review of Scientific Instruments*, vol. 93, no. 7, p. 073201, 2022.

[118] E. Bonvin, L. Devaud, M. Rossi, A. Militaru, L. Dania, D. S. Bykov, O. Romero-Isart, T. E. Northup, L. Novotny, and M. Frimmer, "State expansion of a levitated nanoparticle in a dark harmonic potential," *arXiv preprint arXiv:2312.13111*, 2023.

[119] D. Hempston, J. Vovrosh, M. Toroš, G. Winstone, M. Rashid, and H. Ulbricht, "Force sensing with an optically levitated charged nanoparticle," *Applied Physics Letters*, vol. 111, no. 13, 2017.

[120] J. Ahn, Z. Xu, J. Bang, P. Ju, X. Gao, and T. Li, "Ultrasensitive torque detection with an optically levitated nanorotor," *Nature Nanotechnology*, vol. 15, no. 2, pp. 89–93, 2020.

[121] C. Montoya, E. Alejandro, W. Eom, D. Grass, N. Clarisse, A. Witherspoon, and A. A. Geraci, "Scanning force sensing at micrometer distances from a conductive surface with nanospheres in an optical lattice," *Applied optics*, vol. 61, no. 12, pp. 3486–3493, 2022.

[122] J. Piotrowski, D. Windey, J. Vijayan, C. Gonzalez-Ballestero, A. de los Ríos Sommer, N. Meyer, R. Quidant, O. Romero-Isart, R. Reimann, and L. Novotny, "Simultaneous ground-state cooling of two mechanical modes of a levitated nanoparticle," *Nature Physics*, pp. 1–5, 2023.

[123] J. Rieser, M. A. Ciampini, H. Rudolph, N. Kiesel, K. Hornberger, B. A. Stickler, M. Aspelmeyer, and U. Delić, "Tunable light-induced dipole-dipole interaction between optically levitated nanoparticles," *Science*, vol. 377, no. 6609, pp. 987–990, 2022.

[124] T. Penny, A. Pontin, and P. Barker, "Sympathetic cooling and squeezing of two colevitated nanoparticles," *Physical Review Research*, vol. 5, no. 1, p. 013070, 2023.

[125] V. Liška, T. Zemánková, V. Svak, P. Jákl, J. Ježek, M. Bráneckỳ, S. H. Simpson, P. Zemánek, and O. Brzobohatỳ, "Cold damping of levitated optically coupled nanoparticles," *Optica*, vol. 10, no. 9, pp. 1203–1209, 2023.

[126] I. Brandão, D. Tandeitnik, and T. Guerreiro, "Coherent scattering-mediated correlations between levitated nanospheres," *Quantum Science and Technology*, vol. 6, no. 4, p. 045013, 2021.

[127] J. Vijayan, J. Piotrowski, C. Gonzalez-Ballestero, K. Weber, O. Romero-Isart, and L. Novotny, "Cavity-mediated long-range interactions in levitated optomechanics," *arXiv preprint arXiv:2308.14721*, 2023.

[128] A. Dechant, N. Kiesel, and E. Lutz, "All-optical nanomechanical heat engine," *Physical review letters*, vol. 114, no. 18, p. 183602, 2015.

[129] J. Millen and A. Xuereb, "Perspective on quantum thermodynamics," *New Journal of Physics*, vol. 18, no. 1, p. 011002, 2016.

[130] M. Debiossac, M. L. Rosinberg, E. Lutz, and N. Kiesel, "Non-markovian feedback control and acausality: an experimental study," *Physical Review Letters*, vol. 128, no. 20, p. 200601, 2022.

[131] R. Muffato, T. Georgescu, J. Homans, T. Guerreiro, Q. Wu, D. Chisholm, M. Carlesso, M. Paternostro, and H. Ulbricht, "Generation of classical non-gaussian distributions by squeezing a thermal state into non-linear motion of levitated optomechanics," *arXiv preprint arXiv:2401.04066*, 2024.

[132] A. Arvanitaki and A. A. Geraci, "Detecting high-frequency gravitational waves with optically levitated sensors," *Physical review letters*, vol. 110, no. 7, p. 071105, 2013.

[133] G. Afek, F. Monteiro, J. Wang, B. Siegel, S. Ghosh, and D. C. Moore, "Limits on the abundance of millicharged particles bound to matter," *Physical Review D*, vol. 104, no. 1, p. 012004, 2021.

[134] F. Monteiro, G. Afek, D. Carney, G. Krnjaic, J. Wang, and D. C. Moore, "Search for composite dark matter with optically levitated sensors," *Physical Review Letters*, vol. 125, no. 18, p. 181102, 2020.

[135] D. C. Moore and A. A. Geraci, "Searching for new physics using optically levitated sensors," *Quantum Science and Technology*, vol. 6, no. 1, p. 014008, 2021.

[136] G. Afek, D. Carney, and D. C. Moore, "Coherent scattering of low mass dark matter from optically trapped sensors," *Physical review letters*, vol. 128, no. 10, p. 101301, 2022.

[137] G. P. Winstone, D. H. Grass, A. Wang, S. Klomp, A. Laeuger, C. Galla, C. Montoya, N. Aggarwal, J. Sprague, A. Poverman *et al.*, "High frequency gravitational wave detection with optically levitated nanoparticles: an update on lsd (levitated sensor detector)," in *Optical and Quantum Sensing and Precision Metrology II*, vol. 12016. SPIE, 2022, pp. 57–66.

[138] I. Pikovski, M. R. Vanner, M. Aspelmeyer, M. Kim, and Č. Brukner, "Probing planck-scale physics with quantum optics," *Nature Physics*, vol. 8, no. 5, pp. 393–397, 2012.

[139] T. Weiss, M. Roda-Llordes, E. Torrontegui, M. Aspelmeyer, and O. Romero-Isart, "Large quantum delocalization of a levitated nanoparticle using optimal control: Applications for force sensing and entangling via weak forces," *Physical Review Letters*, vol. 127, no. 2, p. 023601, 2021.

[140] L. Neumeier, M. A. Ciampini, O. Romero-Isart, M. Aspelmeyer, and N. Kiesel, "Fast quantum interference of a nanoparticle via optical potential control," *Proceedings of the National Academy of Sciences*, vol. 121, no. 4, p. e2306953121, 2024.

[141] P. T. Grochowski, H. Pichler, C. A. Regal, and O. Romero-Isart, "Quantum control of continuous systems via nonharmonic potential modulation," *arXiv preprint arXiv:2311.16819*, 2023.

[142] K. Aikawa and M. Kamba, "Revealing the velocity uncertainties of a levitated particle in the quantum ground state," *Physical Review Letters*, vol. 131, 2023.

[143] L. Hackermüller, K. Hornberger, B. Brezger, A. Zeilinger, and M. Arndt, "Decoherence of matter waves by thermal emission of radiation," *Nature*, vol. 427, no. 6976, pp. 711–714, 2004.

[144] M. Rosinberg, T. Munakata, and G. Tarjus, "Stochastic thermodynamics of langevin systems under time-delayed feedback control: Second-law-like inequalities," *Physical Review E*, vol. 91, no. 4, p. 042114, 2015.

[145] F. Tebbenjohanns, M. Frimmer, and L. Novotny, "Optimal position detection of a dipolar scatterer in a focused field," *Physical Review A*, vol. 100, no. 4, p. 043821, 2019.

[146] V. Belavkin, "Quantum filtering of markov signals with white quantum noise," in *Quantum communications and measurement*. Springer, 1995, pp. 381–391.

[147] ——, "Measurement, filtering and control in quantum open dynamical systems," *Reports on Mathematical Physics*, vol. 43, no. 3, pp. A405–A425, 1999.

[148] B. Melo, M. T. Cuairan, G. F. Tomassi, N. Meyer, and R. Quidant, "Vacuum levitation and motion control on chip," *arXiv preprint arXiv:2311.14016*, 2023.

[149] E. Bonvin, L. Devaud, M. Rossi, A. Militaru, L. Dania, D. S. Bykov, M. Teller, T. E. Northup, L. Novotny, and M. Frimmer, "Hybrid paul-optical trap with large optical access for levitated optomechanics," *arXiv preprint arXiv:2312.10131*, 2023.

[150] J. Gosling, A. Pontin, J. Iacoponi, P. Barker, and T. Monteiro, "Sensing directional noise baths in levitated optomechanics," *Physical Review Research*, vol. 6, no. 1, p. 013129, 2024.

[151] F. Ricci, M. T. Cuairan, A. W. Schell, E. Hebestreit, R. A. Rica, N. Meyer, and R. Quidant, "A chemical nanoreactor based on a levitated nanoparticle in vacuum," *ACS nano*, vol. 16, no. 6, pp. 8677–8683, 2022.

[152] M. Frimmer, K. Luszcz, S. Ferreiro, V. Jain, E. Hebestreit, and L. Novotny, "Controlling the net charge on a nanoparticle optically levitated in vacuum," *Physical Review A*, vol. 95, no. 6, p. 061801, 2017.

[153] A. Militaru, A. Lasanta, M. Frimmer, L. L. Bonilla, L. Novotny, and R. A. Rica, "Kovacs memory effect with an optically levitated nanoparticle," *Physical Review Letters*, vol. 127, no. 13, p. 130603, 2021.

[154] N. Silver, *The signal and the noise: Why so many predictions fail-but some don't*. Penguin, 2012.

[155] J. E. Gentle, *Random number generation and Monte Carlo methods*. Springer, 2003, vol. 381.

[156] R. C. Tausworthe, "Random numbers generated by linear recurrence modulo two," *Mathematics of Computation*, vol. 19, no. 90, pp. 201–209, 1965.

[157] S. W. Golomb, *Shift register sequences: secure and limited-access code generators, efficiency code generators, prescribed property generators, mathematical models*. World Scientific, 2017.

[158] N. C. S. Technology and S. Division, "Federal standard 1037c: telecommunications: glossary of telecommunication terms," 1996.

[159] F. Tebbenjohanns, M. Frimmer, V. Jain, D. Windey, and L. Novotny, "Motional sideband asymmetry of a nanoparticle optically levitated in free space," *Physical Review Letters*, vol. 124, no. 1, p. 013603, 2020.

[160] C. Edwards and S. Spurgeon, *Sliding mode control: theory and applications*. Crc Press, 1998.

[161] P. A. Ioannou and J. Sun, *Robust adaptive control*. PTR Prentice-Hall Upper Saddle River, NJ, 1996, vol. 1.

A
List of publications

1. F. Almeida, I. Sousa, O. Kremer, B. P. da Silva, D. S. Tasca, A. Z. Khoury, G. Temporão, and T. Guerreiro, "Trapping microparticle in a structured dark focus," *Phys. Rev. Lett.*, vol. 131, p. 163601, Oct 2023. [Online]. Available: https://link.aps.org/doi/10.1103/PhysRevLett.131.163601;

2. O. Kremer, D. Tandeitnik, R. Mufato, I. Califrer, B. Calderoni, F. Calliari, B. Melo, G. Temporão, and T. Guerreiro, "Perturbative nonlinear feedback forces for optical levitation experiments," *arXiv preprint arXiv:2309.15976*, 2023 (Accepted for publication at Physical Review A);

3. O. Kremer, I. Califrer, D. Tandeitnik, G. Temporão, and T. Guerreiro, "All electrical cooling of an optically levitated nanoparticle" (In preparation);

4. I. Califrer, O. Kremer, G. Temporão, and T. Guerreiro, "Levitated single photon detectors,"(In preparation);

5. D. Tandeitnik, F. Almeida, O. Kremer, A. Zelaquett Khoury, and T. Guerreiro, "Optical saddle beam" (In preparation).

B
Fundamentals for optimal linear filtering

B.1
Expected value as optimal estimation

Given a signal $\mathbf{x}$, defined as a stochastic process X with a probability density function $f_X(\mathbf{x})$, which is symmetric with respect to its mean value $\langle \mathbf{x} \rangle$, even and non decreasing for $\mathbf{x} \geq \langle \mathbf{x} \rangle$, the optimal estimation $\hat{\mathbf{x}}$ of $\mathbf{x}$ is the one capable of minimizing the expected value of a loss function $\mathcal{L}(\mathbf{x} - \hat{\mathbf{x}})$,

$$\langle \mathcal{L}(\mathbf{x} - \hat{\mathbf{x}}) \rangle = \int_{-\infty}^{\infty} \mathcal{L}(\mathbf{x}' - \hat{\mathbf{x}}) f_X(\mathbf{x}')\, d\mathbf{x}'. \tag{B-1}$$

By introducing an auxiliary variable $\mathbf{p} = \mathbf{x}' - \langle \mathbf{x} \rangle$, the expression above can be rewritten as

$$\langle \mathcal{L}(\mathbf{x} - \hat{\mathbf{x}}) \rangle = \int_{-\infty}^{\infty} \mathcal{L}(\mathbf{p} + \langle \mathbf{x} \rangle - \hat{\mathbf{x}}) f_X(\mathbf{p} + \langle \mathbf{x} \rangle)\, d\mathbf{p}. \tag{B-2}$$

Now, consider two integrable real positive-definite and even functions $g : \mathbb{R}^n \to \mathbb{R}$ and $h : \mathbb{R}^n \to \mathbb{R}$. It must be stated that $g(\mathbf{x})$ is non-decreasing and $h(\mathbf{x})$ non-increasing for $\mathbf{x} \geq \mathbf{0}$. Within this conditions it is known that

$$\int_{-\infty}^{\infty} g(\mathbf{x}' + \mathbf{a}) h(\mathbf{x}' + \mathbf{b})\, d\mathbf{x}' \geq \int_{-\infty}^{\infty} g(\mathbf{x}') h(\mathbf{x}' + \mathbf{b})\, d\mathbf{x}', \tag{B-3}$$

where $\mathbf{a}$ and $\mathbf{b}$ are arbitrary constants. Proof of this property can be found with the following steps. First by rewriting the expression above as

$$\int_{-\infty}^{\infty} [g(\mathbf{x}' + \mathbf{a})) - g(\mathbf{x}')] h(\mathbf{x}' + \mathbf{b})\, d\mathbf{x}' \geq 0, \tag{B-4}$$

and then, by rewriting the integration interval from $[-\infty, +\infty]$ to $[-\infty, -a/2] \cup [-\mathbf{a}/2, \infty]$ and applying in the resulting two integrals a pair of variable substitution ($\mathbf{x}' \to -\mathbf{x}'$ and $\mathbf{x}' \to \mathbf{x}' - \mathbf{a}$), Eq. (B-4) becomes

$$\int_{\mathbf{a}/2}^{\infty} [g(\mathbf{x}') - g(\mathbf{x}' - \mathbf{a})][h(\mathbf{x}' - \mathbf{a}) - h(\mathbf{x}')]\, d\mathbf{x}' \geq 0, \tag{B-5}$$

which is known to be true, given that g is non-decreasing and h non-increasing. Consequently, if $\mathcal{L}$ attends to the same conditions of g and f_X to the conditions of h, it leads to

$$\langle \mathcal{L}(\mathbf{x} - \hat{\mathbf{x}}) \rangle \geq \int_{-\infty}^{\infty} \mathcal{L}(\mathbf{p}) f_X(\mathbf{p} + \langle \mathbf{x} \rangle)\, d\mathbf{p}, \tag{B-6}$$

allowing the conclusion that

$$\langle \mathcal{L}(\mathbf{x} - \hat{\mathbf{x}}) \rangle \geq \langle \mathcal{L}(\mathbf{x} - \langle \mathbf{x} \rangle) \rangle. \tag{B-7}$$

In other words, the minimization of the expected value of $\mathcal{L}$ is achieved when $\hat{\mathbf{x}} = \langle \mathbf{x} \rangle$.

B.2 Propagating averages and covariances

Let's consider the following discrete-time stochastic dynamics defined by the state transition matrix $\mathbf{A}_d$ and input matrix $\mathbf{B}_d$,

$$\mathbf{x}_{n+1} = \mathbf{A}_d \mathbf{x}_n + \mathbf{B}_d \mathbf{u}_n + \mathbf{w}_{d,n}, \tag{B-8}$$

where $\mathbf{x}_n$ is the state vector, $\mathbf{u}_n$ is a known input, and $\mathbf{w}_{d,n}$ is a Gaussian zero-mean white noise with a covariance matrix $\mathbf{W}$. Due to the intrinsic stochastic behavior and the Gaussian nature of the probabilistic term, it is of great interest to possess the knowledge of how the first moment, $\langle \mathbf{x}_n \rangle$, and the covariance matrix, $\mathbf{P}_n$, propagate through time. To understand this, we start by taking the expected value of both sides of Eq. (B-8), which results in

$$\langle \mathbf{x}_{n+1} \rangle = \mathbf{A}_d \langle \mathbf{x}_n \rangle + \mathbf{B}_d \mathbf{u}_n. \tag{B-9}$$

The covariance matrix $\mathbf{P}_{n+1}$ can be obtained by using its definition,

$$\mathbf{P}_{n+1} = \langle (\mathbf{x}_{n+1} - \langle \mathbf{x}_{n+1} \rangle)(\mathbf{x}_{n+1} - \langle \mathbf{x}_{n+1} \rangle)^T \rangle, \tag{B-10}$$

then, after substituting $\mathbf{x}_{n+1}$ with Eq. (B-8) and $\langle \mathbf{x}_{n+1} \rangle$ with Eq. (B-9), we encounter

$$\begin{aligned} \mathbf{P}_{n+1} = \langle & \mathbf{A}_d (\mathbf{x}_n - \langle \mathbf{x}_n \rangle)(\mathbf{x}_n - \langle \mathbf{x}_n \rangle)^T \mathbf{A}_d \\ & + \mathbf{w}_{d,n} \mathbf{w}_{d,n}^T + \mathbf{A}_d (\mathbf{x}_n - \langle \mathbf{x}_n \rangle) \mathbf{w}_{d,n}^T \\ & + \mathbf{w}_{d,n} (\mathbf{x}_n - \langle \mathbf{x}_n \rangle)^T \mathbf{A}_d^T \rangle, \end{aligned} \tag{B-11}$$

since $\mathbf{w}_{d,n}$ has zero mean and is uncorrelated with the state vector $\mathbf{x}_n$, and since the control law is deterministic, we can rewrite $\mathbf{P}_{n+1}$ as

$$\mathbf{P}_{n+1} = \mathbf{A}_d \mathbf{P}_n \mathbf{A}_d^T + \mathbf{W}. \tag{B-12}$$

B.3 Recursive least-squares estimator

Linear recursive estimators are powerful tools for parameter estimation [61, 62, 75]. They are particularly advantageous for systems linear in their

parameters a_k, expressed as

$$\frac{d^n\mathbf{x}(t)}{dt^n} = \sum_{k=0}^{n-1} a_k \frac{d^k\mathbf{x}}{dt^k}, \tag{B-13}$$

where $m \in \mathbb{N}, 0 \leq m \leq n-1$. Consider the simplest scenario, the measurement equation applied to a constant vector $\mathbf{a}$ in the presence of white noise $\mathbf{m}_{d,n}$ with zero mean and covariance $\mathbf{M}$,

$$\mathbf{y}_n = \mathbf{C}_d\mathbf{a} + \mathbf{m}_{d,n}. \tag{B-14}$$

The linear recursive estimation $\hat{\mathbf{a}}_n$ of $\mathbf{a}$ is expressed as

$$\hat{\mathbf{a}}_n = \hat{\mathbf{a}}_{n-1} + \mathbf{K}_n(\mathbf{y}_n - \mathbf{C}_d\hat{\mathbf{a}}_{n-1}), \tag{B-15}$$

where $\mathbf{K}_n$ is the estimator gain matrix. The estimation error $\mathbf{e}_n$ and its mean $\langle\mathbf{e}_n\rangle$ are given by, respectively,

$$\begin{aligned} \mathbf{e}_n &= \mathbf{a} - \hat{\mathbf{a}}_n = \mathbf{a} - \hat{\mathbf{a}}_{n-1} - \mathbf{K}_n(\mathbf{y}_n - \mathbf{C}_d\hat{\mathbf{a}}_{n-1}) \\ &= (\mathbf{I} - \mathbf{K}_n\mathbf{C}_d)(\mathbf{a} - \hat{\mathbf{a}}_{n-1}) - \mathbf{K}_n\mathbf{m}_{d,n}, \end{aligned} \tag{B-16}$$

and

$$\begin{aligned} \langle\mathbf{e}_n\rangle &= (\mathbf{I} - \mathbf{K}_n\mathbf{C}_d)\langle\mathbf{a} - \hat{\mathbf{a}}_{n-1}\rangle - \mathbf{K}_n\langle\mathbf{m}_{d,n}\rangle \\ &= (\mathbf{I} - \mathbf{K}_n\mathbf{C}_d)\langle\mathbf{e}_{n-1}\rangle. \end{aligned} \tag{B-17}$$

From Eq. (B-17), it is noteworthy that once $\langle\mathbf{e}_m\rangle = \mathbf{0}$, $\langle\mathbf{e}_n\rangle = \mathbf{0}$ for all $n > m$, independently of $\mathbf{K}_n$. This results indicates that optimal estimation, once achieved, persists within a single time-step of the update in the prediction. However, to successfully produce these predictions, an explicit expression for $\mathbf{K}_n$ is necessary. To this end, we define the criteria to be optimized. The least-square method minimizes the quadratic cost-to-go criteria, the same presented in Section 3.1 for the LQR. The criteria for the step n, $\mathcal{L}(\mathbf{e}_n)$, can be written as

$$\begin{aligned} \mathcal{L}(\mathbf{e}_n) &= \langle(\mathbf{a} - \hat{\mathbf{a}}_n)^T(\mathbf{a} - \hat{\mathbf{a}}_n)\rangle \\ &= \langle\mathbf{e}_n^T\mathbf{e}_n\rangle \\ &= \langle\mathrm{Tr}\,(\mathbf{e}_n\mathbf{e}_n^T)\rangle \\ &= \mathrm{Tr}\,\mathbf{P}_n, \end{aligned} \tag{B-18}$$

where $\mathbf{P}_n$ is the estimation error covariance matrix. Its recursive formulation is given by

$$\mathbf{P}_n = (\mathbf{I} - \mathbf{K}_n\mathbf{C}_d)\mathbf{P}_{n-1}(\mathbf{I} - \mathbf{K}_n\mathbf{C}_d)^T + \mathbf{K}_n\mathbf{M}\mathbf{K}_n^T. \tag{B-19}$$

Now, it remains to encounter the adaptation of $\mathbf{K}_n$ to minimize $\mathcal{L}$. By

taking $\frac{\partial \mathcal{L}_n}{\partial \mathbf{K}_n}$ and applying the relation $\frac{\partial \mathrm{Tr}(\mathbf{ABA}^{\mathrm{T}})}{\partial \mathbf{A}} = 2\mathbf{AB}$, applicable when $\mathbf{B}$ is symmetric, a condition that holds true for $\mathbf{P}_n$, we find

$$\mathbf{K}_n = \mathbf{P}_{n-1}\mathbf{C}_d^T(\mathbf{C}_d\mathbf{P}_{n-1}\mathbf{C}_d^T + \mathbf{M})^{-1}, \tag{B-20}$$

concluding the formulation for the least squares estimator.

C
1550 nm setup characterizations

This appendix is dedicated to document characterizations and results which were left out of Chapter 5.

C.1
Noise characterization

Prior to conducting the all electrical cooling experiment, the high power laser source (RIO Orion + Keopsys CEFA-C-BO-HP-SM) was characterized in the absence of any nanoparticles. This characterization aimed to assess both the noise floor levels provided by the employed detectors (Newport 2117-FC) and the overall intensity noise of the laser light source. These results are summarized in Table C.1.

Configuration	$\bar{\zeta_x}^2(\mathrm{V}^2/\mathrm{Hz})$	$\bar{\zeta_y}^2(\mathrm{V}^2/\mathrm{Hz})$	$\bar{\zeta_z^2}(\mathrm{V}^2/\mathrm{Hz})$
Detection	1.52×10^{-10}	1.73×10^{-10}	4.96×10^{-11}
Detection +high power laser source	1.13×10^{-9}	1.57×10^{-9}	1.30×10^{-10}

Table C.1: Noise floor levels of detection and laser source. Results were obtained after capturing 10000 traces of 40 ms. These values represent the noise floor in a frequency bandwidth ranging from 20 kHz to 1 MHz. The optical source characterization was conducted with the amplifier operating at an output power of 2.82 W (34.5 dBm). The notation $\bar{\zeta_i}$ follows the same convention used in the supplementary material section of Chapter 5.

The employed detector is equipped with a builtin tunable bandpass filter and an adjustable amplifier, enabling the removal of harmonic components at frequencies below 100 Hz. The amplification gain was set to a factor of 100 for all three detectors. The amplification factor was chosen according to the optimization of the SNR.

C.2
Resonance frequencies vs optical input power

The Erbium-doped fiber amplifier (EDFA) used in the experiment from Chapter 5 offers the flexibility of tuning the output power within a range from 25 dBm ($\approx$ 315 mW) to 35 dBm ($\approx$ 3.15 W) while ensuring that its internal electric current remains within the operational range specified by the manufacturer. Through systematic adjustment of the amplifier's output power, and consequently, alteration of the optical power entering the vacuum chamber, its becomes experimentally possible to verify the theoretical expression which provides the correlation between optical power with the particle's resonance frequencies. First, it is necessary to map the relation between the amplifier's output and the optical power in the beginning of the all-electrical cooling setup. Prior to the free-space setup implemented, a series of fibered optical elements were integrated to facilitate parametric cooling within the existing experimental setup. These elements are shown in the diagram in Fig. C.1. It is pertinent to note that these fibered components introduce a power loss, which was characterized for the range spanning from 300 mW to 500 mW. This specific interval was defined by the minimal power output of the amplifier and maximum input power of the employed power meter (Thorlabs 132C).

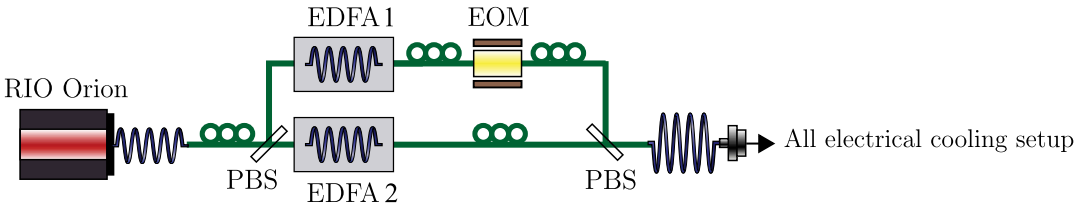

Figure C.1: Fibered experimental setup. A 1550 nm laser source (RIO Orion) outputs approximately 12 mW of optical power which is split into two paths (9 mW/3 mW). The first is designated for modulation purposes, initially amplified by EDFA 1 (Tuolima) up to $\approx$ 60 mW and then sent to an EOM (Covega Mach-10 063). The second path is sent to EDFA 2 (Keopsys), where it is amplified to 2.82 W, and subsequently combined with the modulated part via a PBS. Fibered polarization controllers are added to maintain the non-modulated and modulated portions with orthogonal polarisations.

Figure C.2a) illustrates that within the measured interval the optical power in free space is linearly related to the output power provided by the EDFA (Keopsys). This observation leads to the conclusion that variations in the EDFA's output power will have a linear effect on the optical power used for trapping. This linear relationship was extrapolated to encompass the high

power interval exploited during the experiment. In Fig. C.2b) the experimental relation between trapping power and resonance frequencies is depicted. The solid line represents the curve resulting from fitting the theoretical relation $\Omega_i \propto \sqrt{P}$.

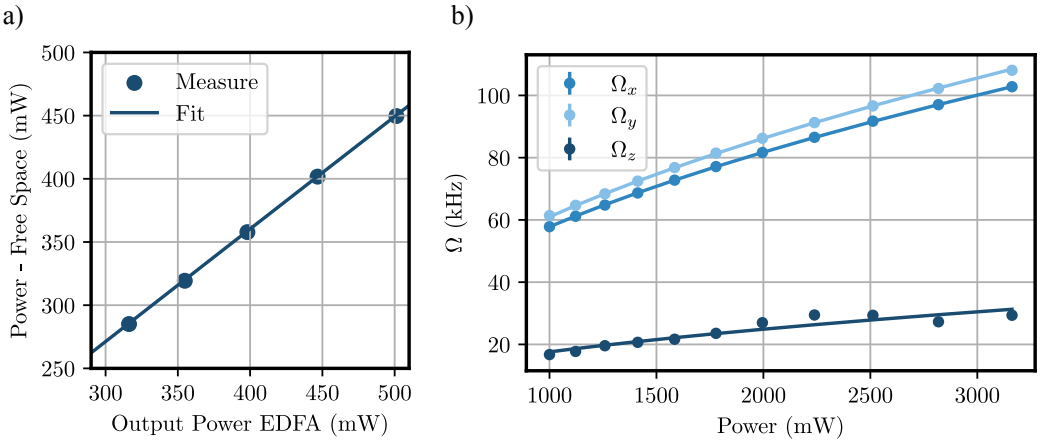

Figure C.2: Resonance frequency dependence with the optical power. a) Optical power used for trapping measured in free-space as a function of the output power supplied by the Keopsys amplifer. b) Dependence between Ω_i and P. Each data point was obtained by fitting a Lorenztian curve to the averaged PSD of 10000 traces of 40 ms. It is noteworthy that error bars are included with each point, although they are found to be negligible.

C.3 EOM and bias-tee for parametric cooling

To effectively implement parametric cooling, two points must be addressed to. First, for proper use of the EOM showed in Fig. C.1, the curve that relates its output power with its supply voltage must be examined. This examination allows us to identify a region where the relationship between these two variables is approximately linear. Second, upon identifying the linear operating region, an electronic circuit must be designed to add a bias voltage, V_{DC}, with an arbitrary radio-frequency signal, V_{RF}, providing a signal $V_{DC} + V_{RF}$ that will be fed to the EOM. The electronic circuit capable of adding bias to radio-frequency signals is known as *bias-tee*. Due to the low value of Ω_z measured in the experiment (which sets the lowest frequency component for modulation), we opted to implement our own homemade bias-tee, enabling for a flat-band response at frequencies as low as $2\Omega_z$.

The electronic diagram of the homemade bias-tee is presented in Fig. C.3a). It was designed and simulated for operation in a frequency range from 30 kHz to

20 MHz, although with the inclusion of appropriate high-frequency components, it could be extended for used up to 4 GHz. Figure C.3b) presents the frequency response by showing the magnitude ratio between output and input for the frequency interval of interest. By plugging the EOM to an adjustable DC power supply (Agilent E3645A) and measuring the optical power in the beginning of the setup from Chapter 5, we constructed the power *versus* voltage curve, presented in Fig. C.3. The vertical gray line, situated between 2 V and 4 V, represents the bias voltage which marks the center of the linear region, where a modulation ±6 mW is achievable.

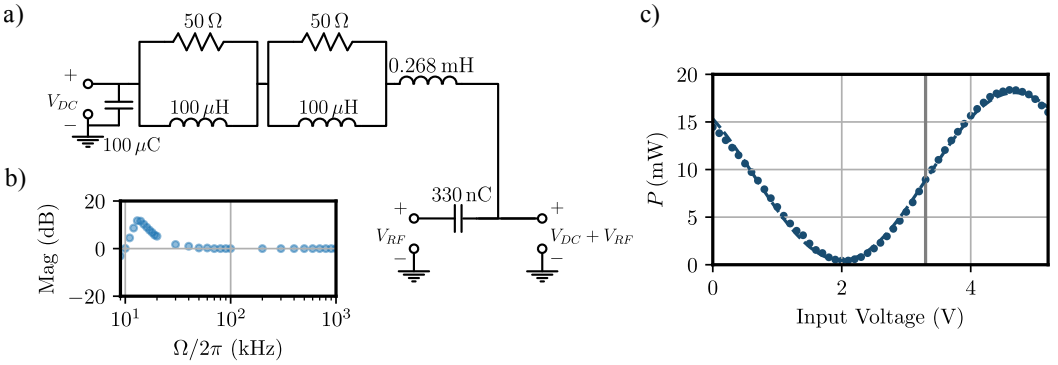

Figure C.3: EOM characterizations. a) Diagram of the bias-tee implemented for combining the V_{DC} provided by the DC power supply and radio-frequency signals. b) Magnitude of the response of the bias-tee, represented as V_{out}/V_{RF}, considering zero bias voltage. c) EOM characterization curve.

D
Code and data availability

The code used to generate the plots presented in this dissertation is available in the following repositories.

- https://github.com/oscarkremer/dissertation-codes (for Chapters 2, 3, 5 and 6);
- https://github.com/QuantumAdventures/non-linearity-experiment (for Chapter 4).

Each repository's main page contains detailed documentation regarding code structure. Additionally, the FPGA code were made available inside the same repos, providing files for sources, simulations and Vivado's project.